Studying Heterogeneity of Chemical Reactions via Single-Molecule Fluorescence

By
Katherine Lupo

A dissertation submitted in partial fulfillment of
the requirements for the degree of

Doctor of Philosophy
(Chemistry)

at the
UNIVERSITY OF WISCONSIN-MADISON
2018

Date of final oral examination: 6/15/2018
The dissertation is approved by the following members of the Final Oral Committee:
Randall Goldsmith, Assistant Professor, Chemistry
James Weisshaar, Professor, Chemistry
Timothy Bertram, Associate Professor, Chemistry
Silvia Cavagnero, Professor, Chemistry

Abstract

Single-molecule fluorescence microscopy (SMFM) is a well-used tool to study sub-ensemble, asynchronous behavior of chemical systems. Recently, SMFM has been extended towards revealing sub ensemble kinetics of inorganic reactions. However, extending SMFM to this realm leads to the necessity of innovation of new fluorophores that fluorescence well in organic solvents and surface immobilization techniques that are not susceptible to destruction under reaction conditions, among other concerns.

This thesis examines several potential solutions to the areas of need identified above. Several systems were investigated at the single-molecule level to vet their potential for use in single-molecule studies. In Chapter 2, the emission properties of dendrimeric catalytic fluorophore assemblies were studied to determine whether they would exhibit higher fluorescence than their monomeric counterpart. Contrary to expectations, higher emission was not observed due to Singlet-Triplet Annihilation, a phenomenon not visible at the bulk level. Different modes of surface immobilization were also investigated. In Chapter 3, the response of the commonly-used silyl ether-silica linkage mode of surface attachment under basic conditions was probed. Interestingly, it was found that the destruction of the linkage exhibited highly heterogeneous behavior only visible at the single-molecule level. Chapter 4 shows the progress that has been made toward the use of toluene-in-water droplets as a means of encapsulating and immobilizing single catalyst molecules to study single-molecule reaction kinetics.

Acknowledgements

My favorite part of every thesis defense I've attended is the part at the end, where the person defending talks about all of the people that have been instrumental in their success in grad school. I know I won't be able to do that part justice, as it would take way longer than the thirty minutes I get to talk to adequately thank all the people that I'd like to thank. So, I'll do that here, in a section that maybe three people will ever read. On the plus side, it will be recorded forever, unlike my presentation. So, I will begin.

Simply put, I would not have made it through grad school without the people I've listed below. I will try in most cases to put what I appreciate about each individual.

My advisor, Randy Goldsmith, has been a constant source of support. I thank him for taking me on as a student, for encouraging me, and for giving me new ideas when I thought nothing would ever work again. Randy, I've seen you grow as an advisor and I appreciate your willingness to adapt your mentorship style to each student. You once told me that I'm the most likely in my year to complain, but you said it as if you *appreciate* that quality, which has gone a long way towards making me feel like it is ok for me to be outspoken.

I thank my fellow students in the Goldsmith Group: undergrads, grad students, and post docs. I've had fruitful discussions about science with all of you that have helped me in many far reaching ways. You are all so much smarter than me and I'm grateful that I've been able to ride on all of you coattails for so long. I'm also grateful to call so many of you friends and I hope I can continue to call you friends once I leave. Our group has gotten too big for me to thank you all individually here, so if any of you are reading this and would like a confidence boost, send me a text or email and I'll tell you something great about you. I would, however, like to especially

mention the catalysis team- James, Daniel, Angela, Andrew, Veronica- for being great coworkers and collaborators on a day to day basis. I know Andrew and Veronica will do a great job of carrying on my and James' legacy. On the friendship side of things, I'm grateful to Daniel for all the food adventures and Kasie for introducing me to hot yoga. Morgan has been a constant source of positivity and coffee dates. I constantly miss Angela and how weird I could be around her. I thank Erik for playing "Guess the Nature Sound" with me and for letting me eat all of his snacks. James has been a great foil for the past 5 years and I'm glad we are friends. I'm sorry that our pizza preferences do not align. Andrew, I appreciate the thought you put into everything you say and do and thank you for all the pep talks you've given me over the past few months.

Ok, I'm getting dangerously close to mentioning everyone, which I said I wouldn't do. I'll end there. Group, on the off chance that you're reading this, send me a line and I'll tell you how much a miss you.

I thank my committee for their kindness and willingness to serve on my committee. Jim Weisshaar has an amazing bank of knowledge on all things single-molecule and I'm glad to have his perspective. Tim Bertram has been an encouraging presence on my committee for my RP and fourth year report. Silvia Cavagnero has kindly agreed to be my fourth committee member, and I'm grateful to have her.

I'm grateful for the various shops, offices, and resources in the chemistry department. They've helped me in many various ways. I'd like to especially shout-out Tracy Drier, who I've gone to with weird problems many times over the years. Thank you, Tracy, for offering solutions above and beyond what was asked of you, and for always being up for an interesting conversation.

I thank all my grad school friends. To my fellow p-chemists who started with me, thank you for being a supportive group. Especially in my first year, I'm glad that we cared about collaborative learning and not about proving ourselves at the expense of others. I thank them for all the weird outings that we did, in particular our yearly corn maze trip. I'm grateful to Britta for living with me, Mitchell for innumerable hang outs, and Tom for bein' Tom. I miss my Tuesday trivia friends: Wyatt, Danny, Brett, and Erin. I'm grateful to my movie night friends, especially Josh, for introducing me to Primer. I glad to have met so many more people that I will not name here who have made my grad school life so much more enjoyable.

I'm lucky to have many friends outside of graduate school. I miss all of my college friends and I'm grateful for their support. I'm particularly glad that Michelle (Mama K) Krankoski Wright could spend a summer here and remind me of the Good Things outside of work. Brooke has always been my go-to friend for discussing our existential angst. I know I could go to Alex and Amanda for anything. Thank you, Elmhurst friends, for being a group of people I know I can always come back to, even if I don't get to see you that often.

I'm lucky to have found a community outside of work that has embraced me. I'm hugely grateful for everything Madison Roller Derby has done for me. Thank you Wreckers for teaching me how to skate and thank you Vaudeville Vixens for letting me skate with you on a regular basis. It has truly been a dream come true to be a Vixen. I've learned so much from each of my teammates, who are too numerous to list here. I am a better person for knowing them. I am hugely grateful to my leaguemates Auntie and Dark Matter, who have very literally fed me, clothed me, and given me shelter. Most importantly, they've both made me cry-laugh more times than I can count and have made my life much richer.

Finally, I'd like to thank my family. Their support has been amazing and I would not have gotten through grad school without the knowledge that they will always support me, no matter what. I grateful for my mom for all the times she dropped everything and came to take care of me when I needed it. I'm also grateful for her sense of humor, her outspoken nature, and her ability to talk to strangers. I hope I inherited a little of each. I'm thankful to my dad for using the phrase "whatever you need, Katie" way more than I deserved which in turn has helped me to follow my dreams with the knowledge that if things don't work out, I will always have a place to go back to. I'm grateful for my brothers, Matt and Rich, for their constant support and faith in me. Every good grade I got was because I was trying to live up to their example. I'm glad to have two great sister-in-laws, Laura and Stephanie, who are fantastic people, and who both have advanced degrees. I'm glad that my niece Jessa will grow up with a mom and two aunts with very diverse interests who will show her that she can truly be whoever she wants to be and do whatever calls to her.

Table of Contents

List of Figures

List of Tables

List of Charts

1. Introduction

1.1 Single-Molecule Fluorescence Microscopy as a Means to Reveal Sub-Ensemble Behavior

Single-molecule fluorescence microscopy (SMFM) aims to reveal underlying physical phenomena that are otherwise obscured in standard bulk measurements. In standard bulk measurements, a given quantity is measured as an average- for example, quantum yield, reaction rate, and mechanisms are all *ensemble averaged* quantities. Ensemble averaged quantities fail to reveal any heterogeneity that may be present. For example, a cuvette filled with a fluorescent solution can be measured on a fluorimeter to have a certain fluorescent intensity. This measurement cannot distinguish between extremes- are all of the molecules emitting the same number of photons at any given time? Are half of the molecules not emitting at all and the other half are twice as bright as the bulk measurement would indicate? Does the distribution of behaviors change over time? Two related concepts that pertain to these questions are often discussed as being uniquely measurable through SMFM- *static* and *dynamic heterogeneity*. *Static heterogeneity* refers to the difference between individual molecules in a system. In the previous example, multiple molecules emitting different numbers of photons over time, ie having different fluorescent intensities, is an example of static heterogeneity. *Dynamic heterogeneity* refers to how the behaviors of single molecules change over time. Related to the previous example of fluorescence, a molecule going into a non-emissive state for a period of time is an example of dynamic heterogeneity. SMFM is uniquely suited to reveal both types of heterogeneity.

Additionally, SMFM allows for the observation of unsynchronized events. To measure many time-dependent quantities on large ensembles of molecules, the events must be synchronized. Thus, events that are not correlated are generally unmeasurable through ensemble methods. In the example of a bulk fluorescence measurement, the emission of a molecule is likely uncorrelated to the emission of other molecules in the system, particularly molecules that are spatially separated from it. Similarly, many time-dependent processes, such as those discussed below, are stochastic, making them difficult or impossible to synchronize. This leads to the impossibility of ensemble observations of these processes. SMFM provides a way to observe unsynchronized events. Because the behaviors of individual molecules are probed, it does not matter whether events are synchronized, thus allowing observation of unsynchronized behavior beyond the ensemble average.

1.2 Use of SMFM So Far

SMFM has long been used as a way to get past ensemble averages to observe heterogeneity. Examples of well-investigated phenomena explored with SMFM include protein folding dynamics, motor protein function, and enzyme dynamics. Forster Resonance Energy Transfer (FRET) has become an important tool for studies on single protein folding dynamics[1] and has been used to show transitions between folded and unfolded states.[2] FRET has also been used to determine transition path timescales, revealing that transition path timescales hardly vary compared to overall folding rates.[3] SMFM has been used to examine rates, step size, and pausing in motor proteins in the myosin and kinesin families.[4] In particular, SMFM has been used to show that kinesin moves over microtubules in a hand-over-hand mechanism as opposed to an inchworm mechanism.[5-6] Enzyme dynamics have also been examined through SMFM, revealing that fluctuations in protein conformations result in large fluctuations in turnover rates.[7] Non-exponential behavior of enzymes has also been shown and attributed to conformation dynamics in enzymes.[8]

While the examples given above constitute research done on biological systems, SMFM has been increasingly used in organic/inorganic systems. In particular, SMFM provides a way to examine energy transfer important to light harvesting applications. Energy transference in dendrimeric arrays[9-11] and semiconducting conjugated polymers[12-14] have both been studied through SMFM techniques to better understand their potential in light-harvesting applications. Additionally, SMFM provides a way to analyze surface dynamics, given the spatial and temporal resolution it provides. In particular, SMFM has been used to understand molecular diffusion in chromatographic systems[15-17] as well as diffusion at liquid-solid interfaces.[17-19]

Ultimately, the goal of research in the Goldsmith Group is to extend SMFM to observation of single turnover events from single inorganic catalyst molecules. Our work has led to novel information on the initiation dynamics of an organometallic catalyst[20] and further work, some of which is described herein, is working towards observation of individual C-C coupling events. Other groups have approached single heterogeneous catalyst studies using platinum,[21-22] palladium,[23] and ruthenium[24-25] catalysts. Much single-molecule work has centered on observations of catalysis on nanocrystals,[26] revealing variability of reactivity based on location on particles.[27] Further work has shown crystal face dependence on reactivity,[28-29] although other studies show that surface defects may have a more pronounced effect on reactivity.[30] Importantly, none of the catalysis research outlined above, from our group and others, feature observations of single catalysts achieving single turnover events. SMFM as applied to inorganic systems is a relatively young field, necessitating more work to enable these types of measurements. The goal of the research presented herein is to examine and perfect the parameters necessary to performing SMFM through single-molecule measurements. Intriguingly, by examining these parameters through SMFM, unusual behavior is often observed, ultimately revealing the power of SMFM.

1.3 Requirements of SMFM

At the core of single-molecule fluorescence microscopy, only a few things are needed. Essentially, all that is necessary is to have a change in fluorescence that indicates a chemical or physical change in the system being studied. However, there are many nuances that determine the efficacy of SMFM. Effective experimental design is essential for a successful experiment. In particular, fluorophore choice and surface immobilization play important roles in how achievable the desired results are. Such considerations will be examined in more detail in this work.

1.4 Fluorophore Choice

There are many considerations to balance when selecting a fluorophore for a SMFM experiment. For one, a change in fluorescence in response to a chemical or physical change in a system is necessary. However, there are many options for what this change can be that are dependent on the design of the experiment. An additional consideration, and one that will be explored in more detail in this work, are the photophysical properties of the fluorophore. Desirable photophysical properties include large absorption cross-sections and high quantum yields.[31] Absorption cross-section is the single-molecule analog to extinction coefficient and relates to the probability that a single molecule will absorb an incident photon. A high absorption cross-section leads to more photon absorption events, which in turn increases the occurrence of emissive events, all other parameters being equal. Quantum yield is a measure of the probability that an absorption event will lead to an emissive event. High quantum yields lead to high photon emission probability. Thus, it is desirable for a fluorophore to have a large absorption cross-section and high quantum yield to maximize the number of photons, and thus the visibility, of the fluorophore.

While these photophysical properties are somewhat tunable through fluorophore design, our group has explored other methods to increase signal-to-noise ratio. Our group has combined the use of synthetic design to tune properties with unconventional methods of increasing fluorophore brightness. In Chapter 1 of this thesis, dendrimeric arrangements of fluorophores are examined to determine their potential efficacy for single-molecule measurements. In this project, multiple fluorophores, up to 4 per molecule, are attached to a catalytic backbone. Thus, while the properties of the fluorophores are not intentionally being tuned through synthesis, the additive fluorescence of each fluorophore on a molecule should increase brightness. Despite these expectations, little difference is seen between molecules with different numbers of fluorophores, revealing unexpected photophysical properties visible only at the single-molecule level.

1.5 Surface Attachment

One important factor in experimental design is choice of fluorophore immobilization. If not immobilized, fluorophores may only exist in a field of view for fractions of a second, thus greatly decreasing the ability to take measurements. Thus, it is often beneficial to immobilize fluorophores in order to increase observation time. However, immobilization also constrains molecules, limiting their ability to move as they would in solution. It is of great importance to determine whether immobilization impacts a system's behavior and to design the system to avoid overly impacting normal function through immobilization. This work discusses multiple modes of immobilizing fluorophores, which will be discussed in depth in Chapters 3 and 4.

The primary mode of surface attachment used in Chapters 2 and 3 are silyl ether to silica linkages. In Chapter 3, the robustness of silyl ether-silica linkages are tested, in particular in relation to detachment caused by interaction with basic conditions. Intriguingly, non-exponential behavior is seen in the linkage failure, revealing the innate heterogeneity of the silica surface that would be obscured by ensemble measurements. In Chapter 4, a new mode of immobilization is presented. Instead of surface immobilization, microscale droplets are used to contain fluorophores. The benefit of droplet immobilization is that fluorophores are confined to a set area and thus cannot diffuse out of solution, but they are still able to freely diffuse within the droplet. However, size control and stability have proven troublesome. Chapter 4 discusses methods that we have employed to approach droplet fabrication, as well as future experiments which will employ droplet immobilization.

2. Fluorescent Dendrimeric Molecular Catalysts Demonstrate Unusual Scaling Behavior at the Single-Molecule Level

This chapter was first published as Upadhyay, S. P.*; Lupo, K. M.*; Marquard, A. N.; Ng, J. D.; Bates, D. M.; Goldsmith, R. H., Fluorescent Dendrimeric Molecular Catalysts Demonstrate Unusual Scaling Behavior at the Single-Molecule Level. *Journal of Phyical Chemistry C* **2015,** *119* (34), 19703-19714. *co-first authors

Katherine Lupo performed single-molecule experiments and did the analysis leading to the central conclusion of the article. Sunil Upadhyay synthesised and performed bulk spectroscopy on compounds **1-5**

2.1 Abstract

A series of surface-supported molecular palladium catalysts were synthesized using a dendrimeric attachment motif to incorporate multiple BODIPY fluorophores for single-molecule fluorescence microscopy. An unusual fluorescence intensity scaling law was observed, whereby the addition of multiple fluorophores did not result in a substantial increase in single-molecule brightness. Possible quenching mechanisms are discussed and simulations of photophysical population dynamics are used to identify singlet-triplet annihilation as the likely origin of the scaling law. This work is a conspicuous example of how the availability of different photophysical kinetic pathways can have substantial influence on molecular design rules, with implications for light-harvesting strategies.

2.2 Introduction

Single-molecule measurements are a potent means of revealing unsynchronized molecular behavior and heterogeneity. While many targets of single-molecule measurements have been biological in nature, single-molecule measurements have also revealed the intricacies of charge and energy transfer in supramolecular chromophore assemblies,[9-11, 32-34] semi-conducting polymers,[12-14, 35-38] and functionalized inorganic materials,[28, 39-41] and have been used to explore molecule-surface interactions.[42-44] More recently, single-molecule measurements have been applied to elucidate fundamental mechanistic questions in chemical reaction dynamics,[45-46] enabling investigation of both molecular[22, 47-49] and heterogeneous catalysts.[26, 29]

Continued exploration of non-biological targets in materials science and reaction chemistry at the single-molecule level will require use of fluorophores in non-aqueous environments. New or different fluorophores will likely be optimal, and development of new conjugation strategies for attachment to chemical targets of interest will be needed. Maintaining desirable signal-to-noise levels will require increasingly bright fluorophores because elevated background levels will result from the enhanced solubility of fluorescent impurities and higher Raman scattering cross-sections in less polar solvents. Identification of the ideal fluorophore for single-molecule experiments in non-aqueous systems is an important outstanding issue.

For studying molecular catalysts, Blum and co-workers have identified borondipyrromethene (BODIPY) dyes as good candidate fluorophores due to the absence of strongly coordinating heteroatoms capable of non-innocent interactions with the metal center of interest.[47] However, despite their high fluorescent quantum yields, solubility, and synthetic tailorability,[50-51] BODIPY dyes suffer from relatively low absorption cross-sections, requiring high pump power to maintain high signal photon streams, but leading to increased background levels. Polycyclic aromatic hydrocarbons would also possess only weak coordinating interactions with metal centers and have been used extensively for solid phase single-molecule spectroscopy experiments,[52-54] but suffer from low solubility and lack of good synthetic handles.

In an attempt to enhance the brightness of fluorescently labeled molecular catalysts for mechanistic investigations, we synthesized a family of dendrimerically labeled surface-supported palladium catalysts (see Chart 1). These catalysts possess multiple fluorescent BODIPY dyes per metal center. Use of multiple fluorophores to increase the brightness of a single target object was used in early attempts at single-molecule fluorescence microscopy,[55] and is a common strategy for *in vivo* tracking experiments where fusion proteins composed of multiple fluorescent proteins are employed to counteract high cellular autofluorescence.[56] However, new synthetic and photophysical strategies must be developed to multi-label small-molecule constructs and molecular catalysts in particular. Dendrimers have been used as a scaffold for holding multiple fluorophores in close proximity, and work by Hofkens, DeSchryver, Mullen, and co-workers has shown dendrimeric fluorophores to be a tremendously rich target for investigations of photophysical processes.[34, 57-60] In this article, we adopt a dendrimer scaffold as a structural element in a novel family of multi-fluorophore molecular catalysts. In the process, an unexpected fluorescence intensity scaling law was observed as an increasing number of fluorophores were added to each molecular system. Our results highlight important design rules that must be considered when developing multichromophoric systems.

More broadly, multichromophore arrays are extremely important systems in any type of natural[61-66] or synthetic[67-73] light-harvesting structure. A diverse array of photodynamic processes can be at play, exerting a significant degree of control over the exhibited absorption and emission properties. While single-molecule investigations of multichromophoric species are a powerful means of elucidating these photodynamics, such measurements are generally performed in air.[10, 33, 57-60] Solution-phase self-assembly of multichromophoric systems has become an increasingly useful approach for controlled exciton and charge flow in photovoltaic devices, but investigations at the single-molecule level have not been performed. Our dendrimerically labeled catalysts are an excellent platform for investigating multichromophoric interactions in non-aqueous media, and the resulting fluorescence intensity scaling laws are relevant for a broad array of energy harvesting motifs.

2.3 Synthesis of Dendrimeric Compounds

Full details of the synthesis and characterization of Compound **1-5** are reported in the published version of this chapter.

2.4 Bulk Spectroscopy

The following section "2.4 Bulk Spectroscopy" was performed by Dr. Sunil Upadhyay and is included to inform the further work.

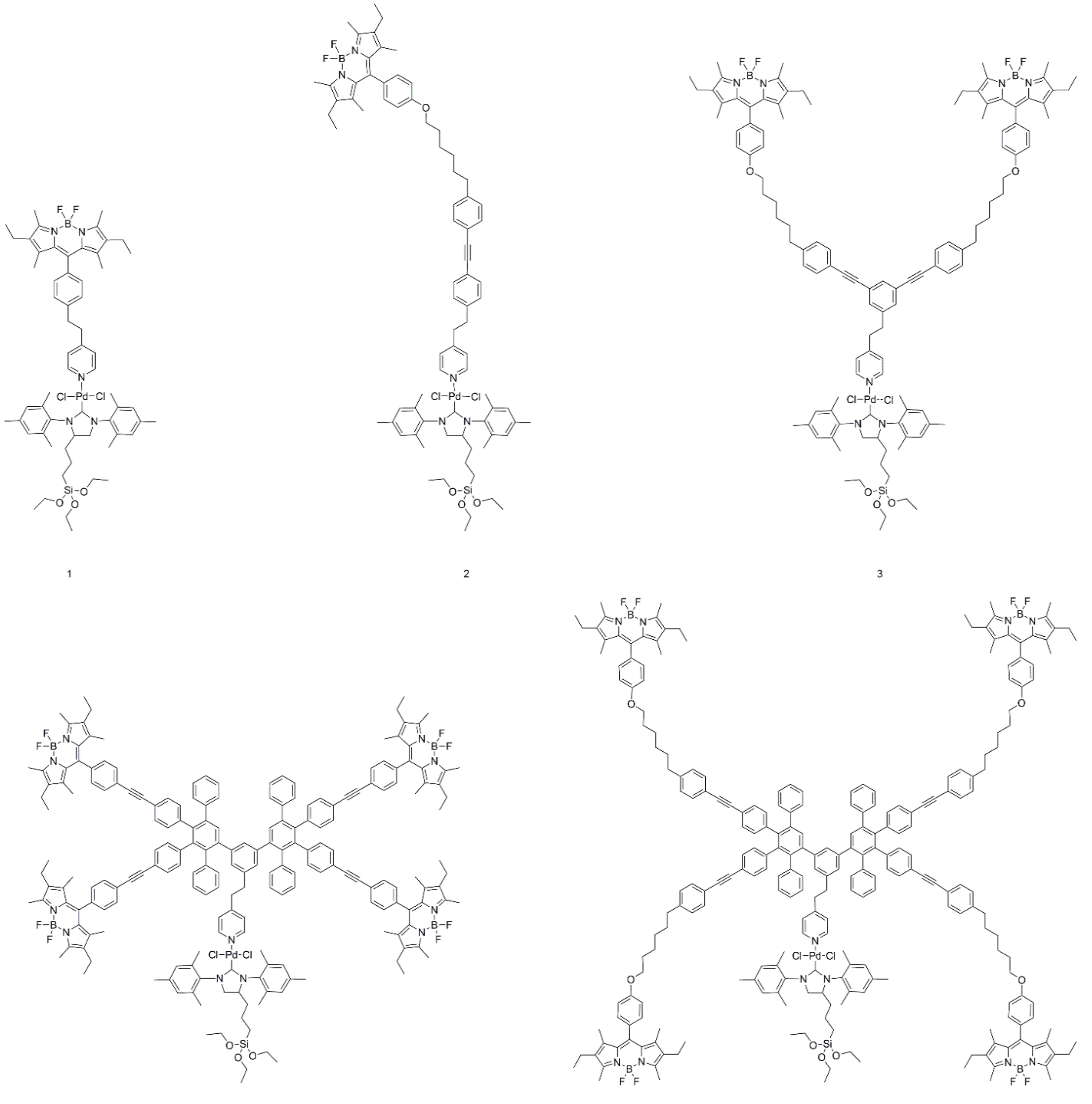

1 2 3 4 5

Chart 1: A Series of BODIPY Labeled Pd-NHC-PEPPSI Catalysts Synthesized with Varying Numbers of Fluorophores and Distances from the Central Pd Atom.

The ground-state electronic absorption and emission spectra of complexes **1-5** in iPrOH at 298 K are shown in Figure 1 and summarized in Table 1. All compounds exhibit absorption patterns that include high intensity intra-ligand S_0-S_1 (π-π^*) transitions typical for BODIPY fluorophores.[74] Compounds **1-3** all have features that overlap at 523 nm whereas compounds **4** and **5** are bathochromically shifted to 526 and 529 nm, respectively. While the minor bathochromic shift for **4** could be ascribed to the increase in conjugation length due to the presence of the ethynyl linkage, the increased width of this peak, as well as the larger shift and broadening for **5** suggest that multiple photophysical phenomena are playing roles.

The emission spectra of complexes **1-5** are shown in Figure 1b, and mirror the trends for the absorption spectra with **4** and **5** showing minor and major bathochromic shifts. The quantum yields (QY) of fluorescence for complexes **1-5** were measured in isopropyl alcohol using Rhodamine 6G as a standard.[75] While **1-3** show high QY values, as expected for BODIPY fluorophores, **4** and **5** are significantly quenched, and only began to achieve QY values comparable to **1-3** after excessive dilution (see Supporting Information).

catalyst	**λ_{max}/nm**	**λ_{em}/nm^a**	**Stokes shift/nm**	**QY^a**	**average maximum brightness/ photons·s^{-1}**	**average total photons detected**
1	523	535	12	0.79±0.006	8.61×10^3	4.28×10^4
2	523	535	12	0.93±0.013	9.61×10^3	2.89×10^4
3	523	535	12	0.87±0.010	8.96×10^3	1.57×10^4
4	526	538	12	0.45±0.007^b (0.38±0.004)	1.02×10^4	3.07×10^4
5	529	544	15	0.70±0.007^b (0.10±0.004)	9.58×10^4	1.45×10^4

Table 1: Fluorescence Data for Complexes **1-5** in iPrOH
[a]Excitation at 508 nm. [b]1% THF in iPrOH and at high catalyst dilution.

Data from steady-state spectroscopy and QY measurements suggest partially conflicting mechanisms. The redshift and broadening of the absorption spectra of 4-5 is a signature of J-

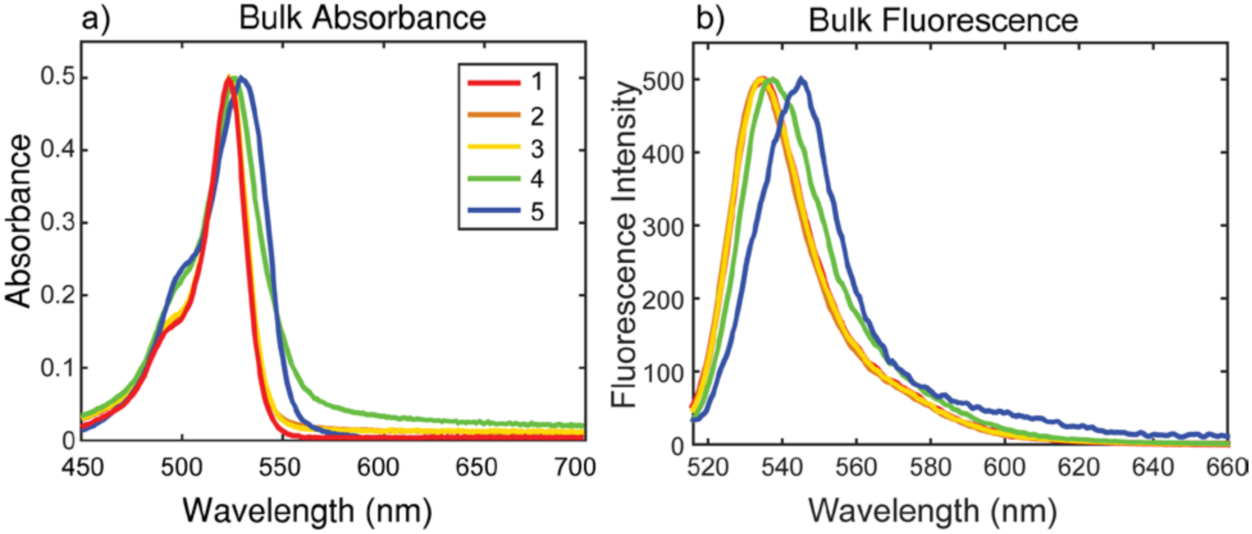

Figure 1: a) Bulk absorbance and b) bulk fluorescence emission spectra of compounds **1-5**. For fluorescence spectra, excitation is provided at 508 nm.

aggregation.[76] Aggregation is also strongly suggested by the concentration dependence of the QY measurements and multichromophoric pi-systems, including those with BODIPY components, are well- known to aggregate in solution.[77] The failure of the QY values of dendrimeric compounds 4 and 5 to rise to the values of 1-3 after dilution further suggests that some residual aggregation may still be occurring. However, unlike H-aggregation, which strongly quenches emission due to the lowest exciton-coupled excited state being symmetry forbidden from radiative return to the ground state, J-aggregation is not known to quench emission and has been observed to enhance emission in BODIPY compounds.[21, 75, 77-78] One possible origin is a mixture of impure H and J aggregation resulting in some quenching but with a net red shift. Quenching could also come from an interaction in the electronic excited state. One possible process is excimer formation, but this process would yield significantly red-shifted emission,[79] which is not observed. Other possible excited state interactions will be discussed below.

2.5 Single-Molecule Spectroscopy

2.5.1 Preparation of Reaction Chambers

Glass tubing (13 mm OD, 10 mm ID, borosilicate, 33 COE) was cut into roughly 4 cm lengths. Each cut side was polished using silicon carbide (Wale Apparatus, 600 grit) and rinsed with Millipore water, acetone, and methanol. Glass coverslips (Fisherfinest, 25x25x0.17 mm) were rinsed with methanol, acetone, and methanol again. After drying, the tubes and coverslips were O_2 plasma cleaned in 300 W plasma for 3 minutes.

The cleaned coverslips were arranged on a cold hotplate. The glass tubing was individually dipped into a 40% sodium silicate solution that was prepared by diluting 40° baumé sodium silicate (J.T. Baker) with Millipore water. Excess sodium silicate was removed by dabbing the dipped end of the tubing against aluminum foil. The dipped end was placed on a coverslip, weighted down with an appropriately sized ball bearing, and rotated about half a turn to ensure contact with the

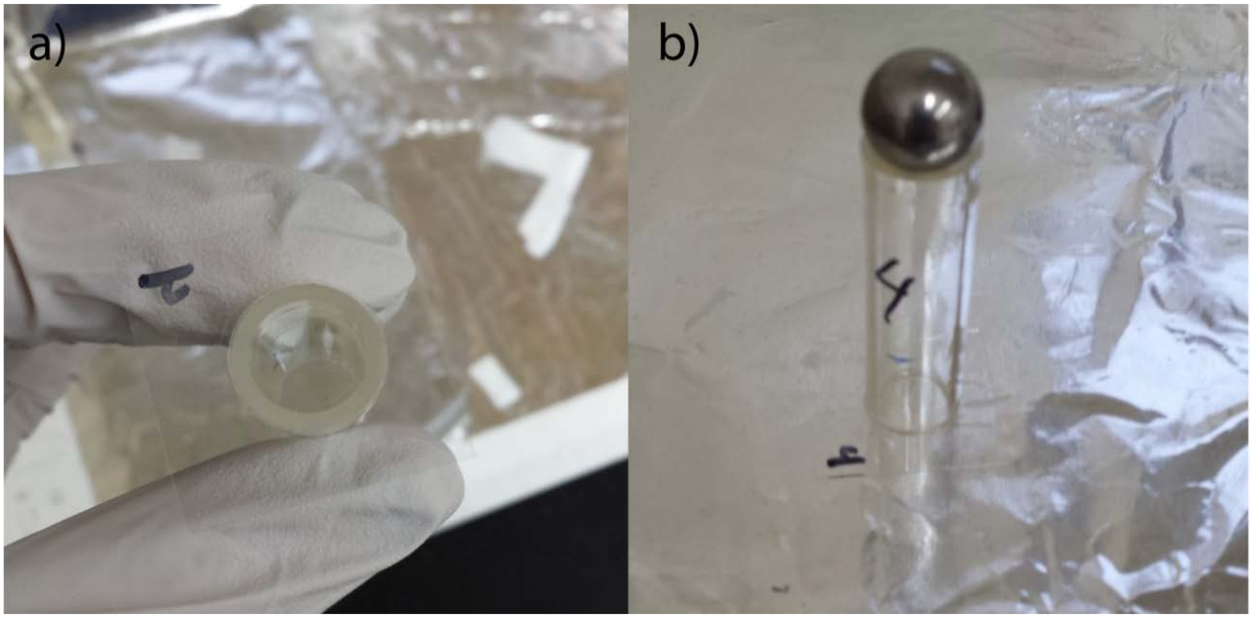

Figure 2: a) Bottom-up view of a completed chamber. The tube is attached to a coverslip. b) A chamber curing on a hotplate with a ball bearing to weigh it down.

surface. After all tubes were placed on coverslips, the chambers were heated to a final temperature of 135 °C, starting at 60 °C and increasing the temperature by 15 °C every 15 minutes. The chambers sat at 135 °C overnight and allowed to cool to room temperature before use.

2.5.2 Deposition of Dendrimeric PEPPSI Catalysts:

All glassware, including chambers, was rinsed with HPLC grade methanol, acetone, and methanol and allowed to dry before O_2 plasma cleaning at 300 W for 3 minutes. HPLC grade isopropanol was photobleached for 3 days in a home-built photobleaching apparatus.[80] Stock solutions of the catalysts were prepared by dissolving small amounts of catalyst in photobleached isopropanol. Due to the low solubility of the dendrimers, in some cases it was necessary to remove excess solid from the stock solution before further dilution and deposition. When not in use, the stock solutions were covered in aluminum foil and stored in a -20 °C freezer. Before use, the stock solutions were sonicated for about 15 minutes and returned to room temperature. Fresh dilutions of the catalysts were prepared before every deposition and were selected based on the resultant surface coverage produced in the chambers. Generally samples with roughly 100 molecules per field of view were used, corresponding to a surface coverage of about 1 molecule/20 μm^2.

To deposit catalyst into chambers, 500 μL of the diluted catalyst solution was placed in chambers, covered with coverslips, and left to react at the surface via the silyl ether surface anchor at room temperature in a dark environment for one hour.

At the end of the hour, the solutions were pipetted out of the chambers and rinsed with 500 μL of isopropanol, using a micropipette to mix the isopropanol in the chamber before pipetting it out. The chambers were dried in an oven at 110 °C for 8 minutes, left to cool, and rinsed with isopropanol as before. The chambers were then filled with 500 μL of clean isopropanol prior to imaging.

To ensure that fluorescent impurities were not an issue, control “blank” samples were prepared in the same manner as the catalyst samples, except that 500 μL of isopropanol was added to the chambers in place of the catalyst solutions. Blank samples were left to sit for one hour and rinsed in the same manner as the catalyst samples. An example of a widefield image of a blank sample and a sample with deposited catalyst solution is shown Figure 3.

2.5.3 Microscopy

A 532 nm Coherent Sapphire fiber-coupled diode laser with at 5.1 mW output power was expanded using a telescope and guided through a Nikon 60x Apo TIRF 1.49 NA oil-immersion objective fitted to a Nikon Eclipse Ti inverted microscope. At the sample, the beam was 2.12×10^{-5} cm^2 in area and had an intensity of 239 W/cm^2. The fluorescent signal was collected through the same objective, passing through a Semrock 532 nm RazorEdge Dichroic mirror and a Semrock EdgeBasic 532 nm longpass filter before being focused onto an Andor EMCCD iXon camera with a 512 x 512 pixel detector. Sample illumination was controlled using a Uniblitz shutter.

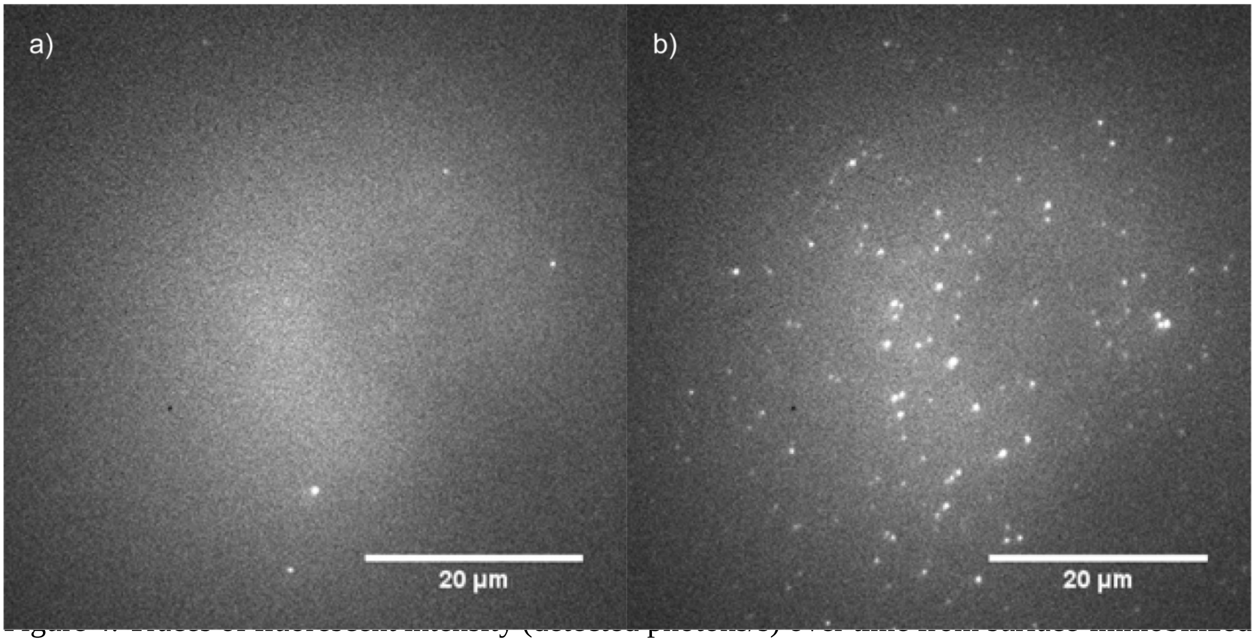

Figure 3: Comparison of a control sample and an actual sample. a) A typical widefield image of a blank sample. b) A typical widefield image of deposited catalyst (compound 4, conditions as described in text).

2.5.4 Imaging

Widefield images of PEPPSI catalysts were taken by starting a video acquisition before starting to illuminate the sample spot and then opening the shutter to prevent excess photobleaching in the sample prior to imaging. In general, only about 10 frames elapsed before the shutter could be opened. Images were recorded for 500 frames with 100 ms exposure times, resulting in roughly 50 seconds of video, during which time most of the fluorophores photobleached. Home-written Matlab programs were used to remove the dark initial frames, find individual molecules, track their intensity over time, and analyze the resultant traces.

For saturation studies, samples with higher surface concentrations were prepared. Individual frames at various laser powers were taken at the same location on a sample, starting at low powers and ramping up and down again to minimize photobleaching. To prevent excess photobleaching, each sample was only illuminated while the 100 ms frames were collected by synchronizing the camera shutter and an external shutter. After subtracting background, the mean intensity of each sample was plotted against the incident laser intensity.

2.5.5 Image Analysis

Home-written Matlab programs were used to analyze all data. After removing the dark frames that were recorded before opening the shutter, a spot finding program[81] was used to locate single molecules. The fluorescent intensities of the resultant spots were tracked over all frames, resulting in fluorescence intensity trajectories of individual molecules. To remove the effect of background fluorescence on the intensity traces, the fluorescence intensity of a 2 pixel wide perimeter around each fluorescent center was subtracted from the intensity of the central group of pixels at each frame. Traces that displayed analog intensity dynamics, poor background subtraction, or did not have any change over the entire trace were rejected for further analysis. A change point finding algorithm[82] was employed to determine the number of intensity levels above background. A histogram was created of the number of intensity levels for each molecule. The highest intensity level for each trace was recorded as the maximum intensity. Finally, the total number of photons emitted in each trace was quantified by integrating the trace and subtracting off the background level. Histograms of maximum emission intensity and number of photons emitted were prepared.

2.6 Results

Single-molecule fluorescence microscopy was used to explore the photophysical properties and dynamics of our labeled catalysts. Critically, because single-molecule measurements

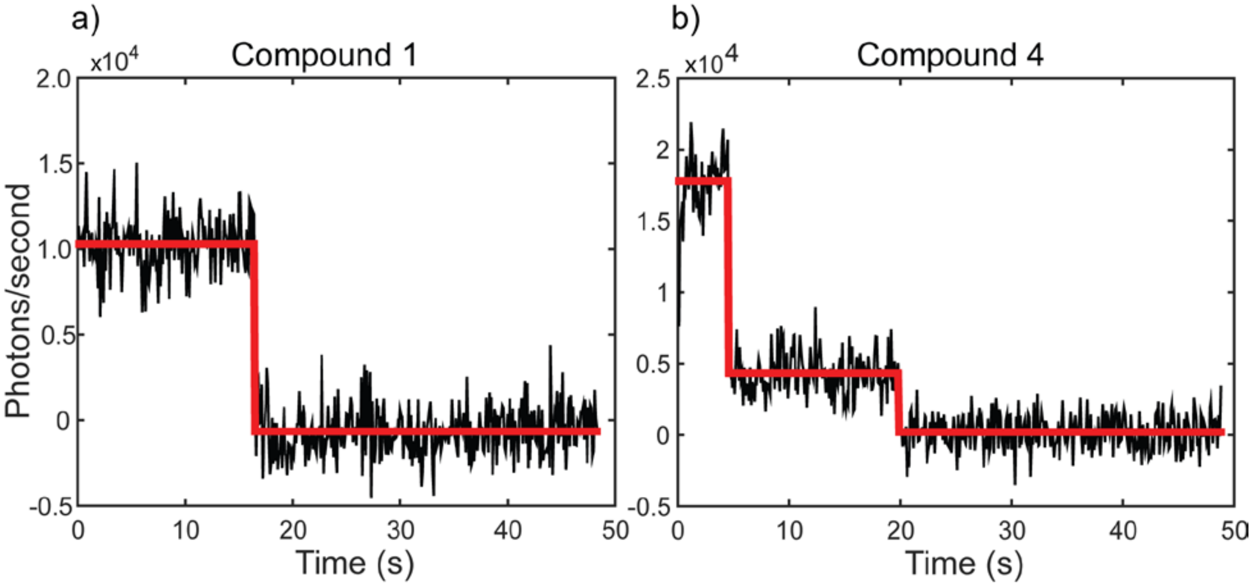

Figure 5: Traces of fluorescent intensity (detected photons/s) over time from surface-immobilized single molecules of a) compound **1** and b) compound **4** under isopropanol. Molecules were excited with 240 W/cm^2, 532 nm light. Emission was detected by an EMCCD camera operating at 100 ms per frame.

generally involve much higher excitation energies compared to bulk measurements, they probe molecules in a very different photochemical steady state, as will be described below. Compounds 1-5 were deposited onto glass coverslips at low surface coverages from highly diluted stock solutions where residual aggregation is likely eliminated and individual molecules are conspicuously observed. Samples were imaged under widefield illumination.[31] The time-varying fluorescence intensities of individual molecules were tracked over time to determine maximum brightness level, photobleaching dynamics, and photobleaching rate. Example time traces are shown in Figure 4. A change-point finding algorithm[82] was used to identify the accessed fluorescence intensity levels for each molecule. In Figure 5a, a histogram shows the distribution of the maximum brightness level (photons detected per unit time) exhibited for each individually probed molecule. For compounds **1-5**, most molecules show a maximum photon emission rate (averaged over the intensity plateau) near 3750 detected photons/second. Surprisingly, it appears that the additional fluorophores on compounds **3-5** do not make for more detected fluorescence intensity per molecule, a brighter emitter. The number of fluorescence intensity levels exhibited per molecule due to step-wise photobleaching was evaluated and is shown in Figure 5b.

Multiple resolvable brightness levels are seen even for the singly labeled complexes, and little difference in the number of brightness levels is seen between all five compounds. The total number of detected photons, an indicator of photostability,[83] was characterized for each complex, and displayed in Figure 5c. As expected, the curves demonstrate an exponential decay.[83] Little difference is seen between compounds **1-5**, indicating that linker length and number of fluorophores do not have a substantial influence on photostability.

2.7 Discussion

Compounds **1-5** were designed with the implicit assumption that more fluorophores per molecule would result in proportionally brighter (more photons detected per unit time) molecules upon photoexcitation. The validity of this assumption is based on the notion that the individual BODIPY fluorophores would exhibit weak intramolecular electronic interactions. In this limit, the multiple fluorophores on one molecule should each fluoresce at roughly the same rate, resulting in brighter molecules as discerned via single-molecule fluorescence microscopy. Additionally, we expected that individual molecules would display multiple brightness levels as the weakly coupled component fluorophores are independently trapped in dark states or photobleached, as have been observed in many multi-chromophore systems.[60, 84-85] These expectations were based on earlier uses of a similar dendrimer scaffold yielding weakly-coupled multichromophore photosystems.[60] Contrary to our expectations, the brightness of each of our multi-BODIPY functionalized PEPPSI compounds **1-5**, as demonstrated above, is largely the same. A common cause of decreasing fluorescence intensity in multi-fluorophore systems is self-quenching, usually originating in H-stacking of the component fluorophores. However, one diagnostic of H-stacking is a decreased fluorescence QY. Dendrimers **4** and **5** exhibit significant lowering of the QY at moderate or high concentrations, but at lower concentrations (and by extension, the extremely low concentrations of single-molecule experiments), compounds **1-5** demonstrate very similar QY values, indicating that H-stacking is not occurring. This conclusion is corroborated by the absence of blue shifting of absorption peaks relative to the non-exciton-coupled versions, which is also not observed. These observations, as well as the lack of a simple underlying mechanism, suggest the need to delve deeper into the photophysical properties of these compounds.

Multiple factors influence the apparent brightness of a fluorophore. With the benefit of a Jablonski diagram, Figure 6a, we can divide these factors into two classes, processes that principally affect the rate of reaching S_1, the first electronic excited state, and processes that principally affect the rate of S_1's decay, radiatively or non-radiatively. Both classes of processes can be influenced by intramolecular conformational changes and the interaction of molecules with

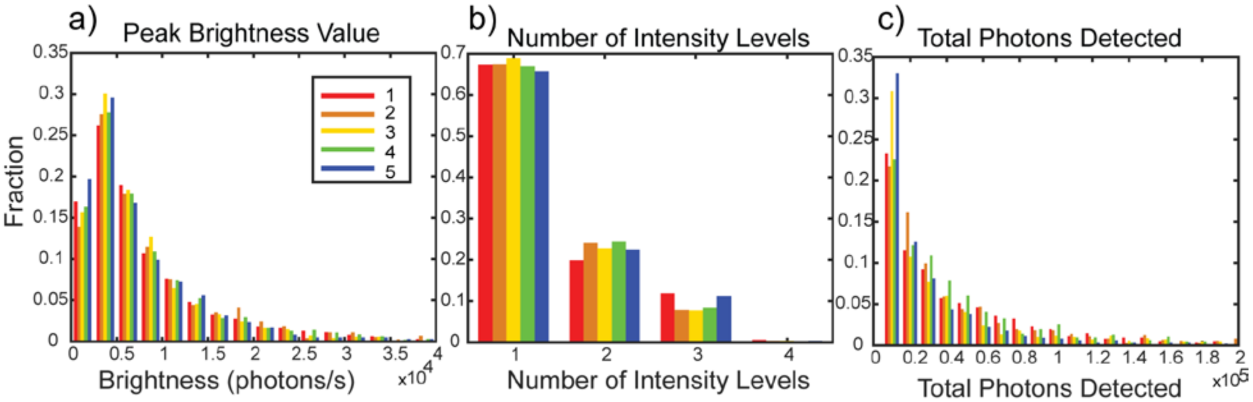

Figure 6: Histograms for compounds **1-5** for a) maximum fluorescence intensity values for individually probed molecules, b) number of intensity levels per molecule and c) total number of photons detected from each individual molecule. The following numbers of molecules were analyzed: **1**: 606, **2**: 704, **3**: 662, **4**: 904, **5**: 939.

their local microenvironment. Factors that affect the rate of formation of S_1 are dominated by interactions between the molecule and the excitation field. A higher absorption cross-section will increase the rate of photon absorption. Increasing the number of absorbing antenna chromophores will increase the effective absorption cross-section, though this effect will see diminishing returns at extremely high intensity fluxes, resulting in "exciton blockade" behavior.[57, 86] However, a simpler explanation is likely responsible for our observed broad distribution of peak brightness and intensity fluctuations. The orientation of chromophores relative to the linear polarization of the excitation field will strongly modulate absorption probabilities. Previous examinations of dendrimeric chromophores showed highly variable brightness values, offering examples of molecules with a larger number of antenna units demonstrating a smaller peak brightness value than molecules with smaller numbers of antenna.[57, 60]

These studies entailed immobilizing molecules in a transparent host polymer, essentially locking the molecules into a limited subset of conformations. In our studies, molecules are covalently attached to and immobilized at the surface, but are also exposed to solvent. Consequently, they will explore a substantially larger conformational space, with conformational fluctuations occurring on timescales slower than when the molecules are entirely in solution, but as seen in Figure 4, fast enough to be appreciated on our measurement timescale. The expected behavior then is for molecules to exhibit a range of brightness values, and that fluorescence intensities are expected to fluctuate as a function of time even before photobleaching is factored in, including monomeric materials like **1** and **2**, as observed.

While conformational fluctuations, including shifts of the orientation of the absorption transition dipole moment, can explain the presence of multiple intensity levels, as seen in Figure

4 and Figure 5b, they alone cannot explain the similar brightness levels across **1-5** shown in Figure 5a. Rates of excited state decay can exert tremendous influence on the brightness of fluorophores. In most bulk experiments, these decay rates can be succinctly related to the brightness via the QY,

$$\boldsymbol{QY = \frac{k_{rad}}{k_{rad}+k_{NR}} = \frac{k_{rad}}{k_{obs}}} \qquad \text{Equation 1}$$

where k_{rad} is the radiative rate of decay, k_{NR} is the rate of nonradiative decay processes to the ground state, and k_{obs} is the observed rate of excited state decay and is a sum of the rates of all radiative and non-radiative processes consuming the excited state. Large changes in the relative magnitudes of k_{rad} and k_{NR} can substantially affect the brightness, but will also result in changes to the QY, which are not observed in independent measurement, Table 1. By extension, if the QY's of 1-5 are comparable, as observed, 4 and 5 should be approximately four times as bright and 3 should be twice as bright as 1 and 2.

Bulk QY measurements are generally performed under low excitation fluence. On the other hand, single-molecule measurements are performed under conditions of high fluence, where

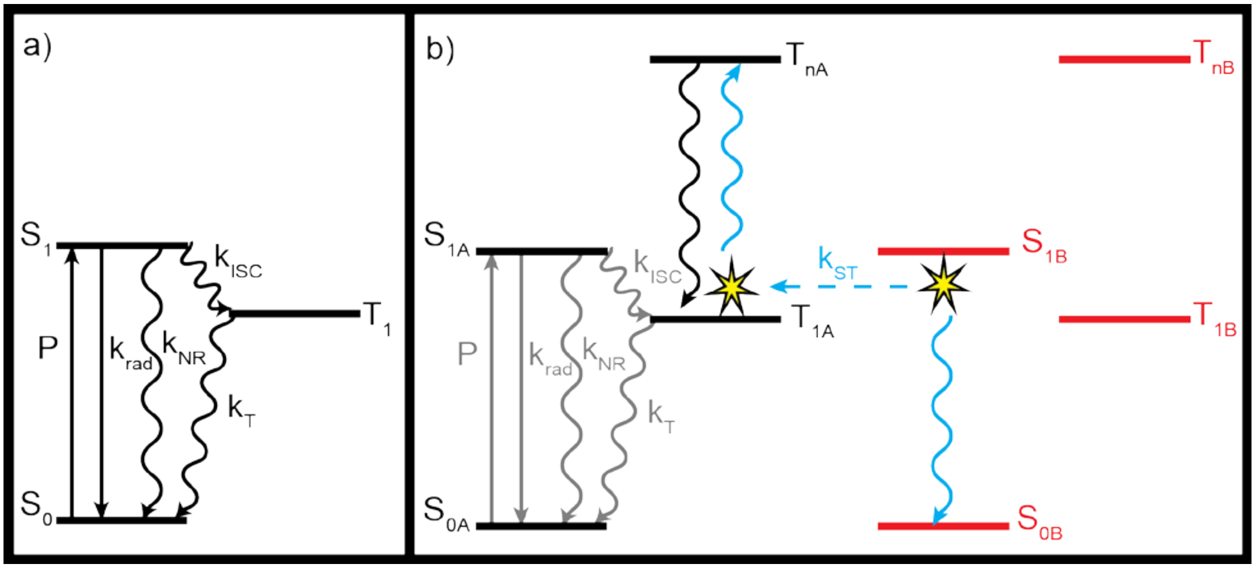

Figure 7: Jablonski diagrams for a) the one site system with three electronic levels and all relevant processes shown and b) a two site system, with each site having four electronic levels. The process of Singlet-Triplet annihilation is highlighted.

many repeated photocycles amplify the influence of rare events and slow photophysical processes. The oversized influence of slow processes is conspicuous in the calculation of saturation intensity, I_S, in a three-level system that includes a triplet state T_1 as compared to a two-level system. Increasing excitation intensity above I_S does not result in a linear increase in S_1 population or, ultimately, emission intensity, but asymptotically approaches a plateau with vanishing marginal increase in emission.

I_S is given by the following equations for the 2- and 3-level systems,[31] respectively:

$$I_S = {}^{h\nu}/_{(2\sigma\tau_{obs})} \qquad \text{Equation 2}$$

$$I_s = \frac{h\upsilon}{2\sigma\tau_{obs}}\left(\frac{1+\left({}^{k_{isc}}/_{k_{obs}}\right)}{1+\left({}^{k_{isc}}/_{2k_T}\right)}\right) \qquad \text{Equation 3}$$

where h is Planck's constant, ν is the frequency of the excitation light, σ is the absorption cross section of the molecule of interest, τ_{obs} is the inverse of k_{obs}, and k_T is the decay rate from T_1 to S_0. Fluorescence intensity and saturation intensity are related to power by the following:

$$I_{Fl} \propto R_\infty\left(\frac{{}^{I}/_{I_S}}{1+{}^{I}/_{I_S}}\right) \qquad \text{Equation 4}$$

The fluorescence intensity of compounds 1 and 4 as a function of excitation power, along with a fit to Equation 3, are shown in Figure 7. Both compounds exhibit saturation behavior slightly above the excitation intensity used in the single-molecule experiments.

The presence of a long-lived triplet state with modest quantum yield of intersystem crossing of just 2% is enough to cause the molecule's emission to saturate at an order of magnitude lower power than for a two-state system. Said another way, even if a transition is rare, once it occurs, the resulting state is long lived enough to have a tangible effect. The existence of such "triplet bottlenecks" are common in single-molecule fluorescence experiments, with various reagents shown to increase brightness by reducing the fraction of time and population spent in non-emissive triplet states.[87-90] However, reaching saturation behavior is not sufficient to eliminate the expected *additive* brightness of having multiple fluorophores, as was observed.

Though the presence of long-lived triplets can result in saturation behavior at lower intensities and lower brightness levels, they can also open additional photophysical quenching mechanisms. Singlet-triplet (S-T) annihilation,[58, 91] Figure 6b, is a spin-allowed process whereby energy transfer from an excited singlet donor (D) to a triplet acceptor (A) results in a ground state donor and an excited state triplet acceptor which quickly thermalizes to the lowest triplet level,

$D^*(S_1) + A^*(T_1) \rightarrow D(S_0) + A^*(T_n) \rightarrow D(S_0) + A^*(T_1)$

This process should not be confused with spin-forbidden singlet-triplet energy transfer where a singlet excited state decays to a singlet ground state while promoting another ground state into a triplet excited state, resulting in a change of overall spin multiplicity.[79] The requirements for S-T annihilation are co-existing populations of both initial excited states, spectral overlap between the emission of the donor S_1 and absorption of the acceptor T_1, and close proximity, with the latter two requirements comparable to those of more traditional singlet-singlet Förster energy transfer. S-T annihilation has been observed in the photosynthetic apparatus,[65, 92-95] conjugated polymers,[96-97] and in dye sensitized solar cells where it manifested as a wasteful process.[98] Critically, by being able to exert synthetic control over the number of fluorophores in our complex, unlike in natural systems, we are able to explicitly explore the effect of S-T annihilation on scaling laws in assembling multichromophoric arrays. Previous studies of dendrimeric fluorophores have implicated S-T annihilation in explaining collective blinking and increased off-times in dendrimeric systems.[99-101] but did not address the effect S-T annihilation has on scaling laws. In

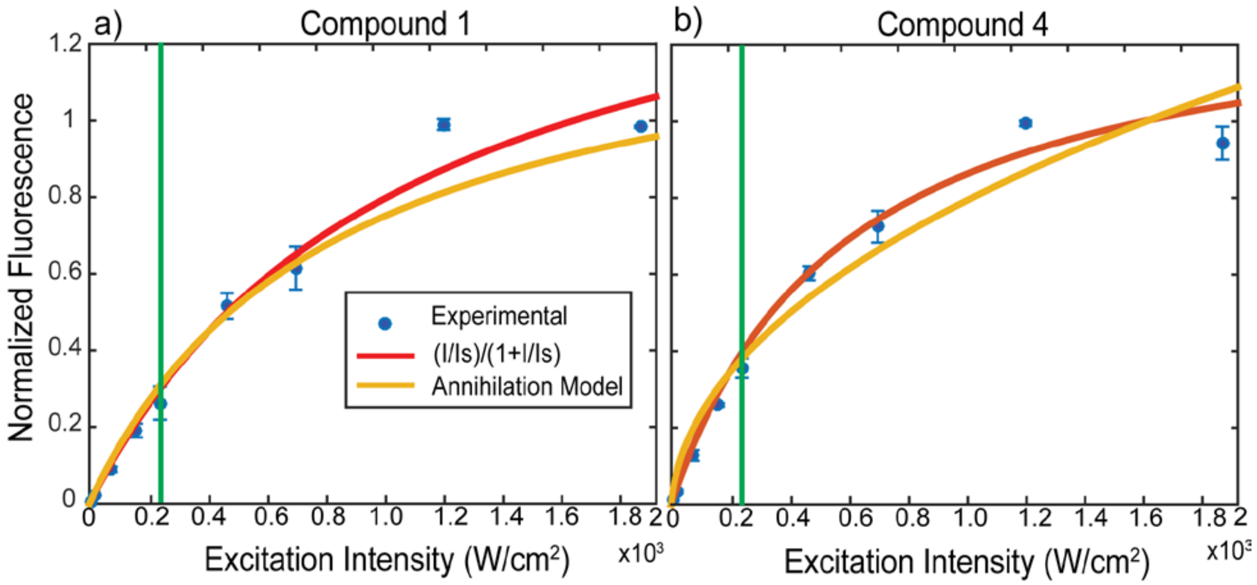

Figure 8: Saturation behavior exhibited by a) compound **1** and b) compound **4**. High surface coverage samples were illuminated with increasingly intense illumination and the average fluorescence intensity at each power was determined. Each point is an average from two samples. The red trace shows the fit to Equation 4 and the yellow trace models the saturation behavior expected from a model that includes singlet-triplet annihilation (see main text). The green vertical line indicates the intensity used for single-molecule experiments.

these previous studies, extremely slow relaxation from the lowest triplet state due to the absence of oxygen resulted in collective quenching of the entire array that was directly visible in fluorescence-time trajectories.[99-101]

For S-T annihilation to be considered a possible contributor it is necessary to determine if the S-T energy transfer rate is high enough to compete with fluorescence. A value for k_{ST} can be estimated using the theory of resonance energy transfer,[76] where the singlet excited state is the donor and the triplet excited state is the acceptor. For resonance energy transfer to occur, it is necessary to have overlap between the fluorescence of the donor and the absorbance of the acceptor. We have measured the bulk fluorescence emission spectra of **1-5** above, Figure 1. The acceptor absorption spectrum is the T_1-T_n absorption spectrum, which we modelled using a sum of Gaussians from the work of Montejano et al,[102] and has significant spectral overlap with the emission of **1-5.** The fluorescence emission from compound **1** was used because the bulk fluorescence of **4** shows signs of aggregation. At the single-molecule level, aggregation is not expected, thus the fluorescence emission of a single molecule is expected to resemble the bulk emission of **1** as opposed to **4**. The overlap is shown in Figure 8. The spectral overlap between the donor fluorescence and the acceptor absorbance is quantified by the overlap integral J(λ):

$$J(\lambda) = \int_{-\infty}^{\infty} F_D(\lambda)\varepsilon_A(\lambda)\lambda^4 d\lambda \qquad \text{Equation 5}$$

Where $F_D(\lambda)$ is the normalized donor emission spectra and $\varepsilon_A(\lambda)$ is the acceptor extinction coefficient. The overlap integral can then be used to calculate the Forster radius R_0, the distance between the donor and acceptor where half of the donor molecules decay through resonance energy transfer,[76]

$$R_0 = 0.211[\kappa^2 n^{-4} QYJ(\lambda)]^{1/6} \qquad \text{Equation 6}$$

where κ^2 accounts for the relative orientation of the donor and acceptor transition dipoles and is assumed to be 2/3, n is the refractive index of the medium, and QY is the quantum yield of the donor without the acceptor present. From R_0, the rate of energy transfer between the donor and acceptor, k_{ST} is calculated as a function of distance, r, between the donor and acceptor:

$$k_{ST}(r) = \frac{1}{\tau_D}\left(\frac{R_0}{r}\right)^6 \qquad \text{Equation 7}$$

where τ_D is the fluorescence lifetime.

The relationship between k_{ST} and interchromophoric distance is shown graphically in Figure 10. Because k_{ST} scales with $1/r^6$, k_{ST} decreases rapidly with increasing r value. Using computationally derived values for r, we can estimate the expected k_{ST} values for our system. Collaborator Desiree Bates performed computations to calculate r and details of the calculation are presented here. To find the interchromophoric distances in compound **4**, the structure was optimized with the semi-empirical PM6 method.[103] Gradients of the optimized structures reported here are less than $1\text{x}10^{-4} E_h$ bohr^{-1}. Harmonic vibrational frequencies were obtained for all

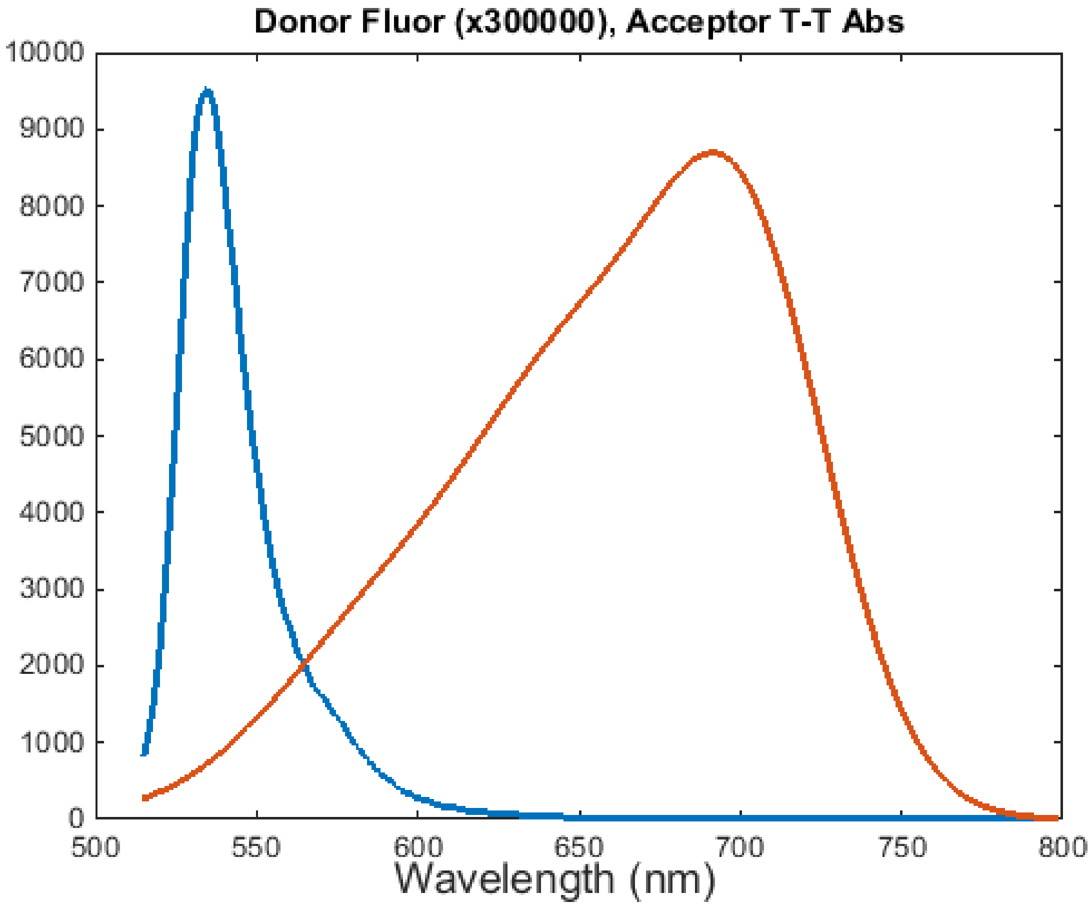

Figure 9: Experimentally determined fluorescence emission (blue) of compound **1** and T-T absorption (red) modelled off of the work of Montejano et al. Fluorescence emission is normalized to have unity integration. Here, the curve is multiplied by 300,000 so that it is on the same scale as T-T absorption. The T-T absorption is presented in terms of extinction coefficient, in units of $M^{-1}cm^{-1}$.

structures to determine the nature of the stationary point. Imaginary frequencies were found for both structures. However, all imaginary frequencies are less than 2 cm^{-1}. All calculations were performed with Gaussian 09 Software package. The computationally derived structure for **4** is shown in Figure 9. A wide range of interchromophoric distances is seen, ranging from 1.4 nm to up to 3.3 nm. The average distance from one chromophore to any other is approximately 2 nm. We use this average distance when determining the expected value for k_{ST} (see Figure 10). This corresponds to a k_{ST} value of approximately 5 ns^{-1}. However, it must be determined if a k_{ST} value of 5 ns^{-1} can reasonably explain the experimentally observed fluorescence intensity scaling law.

To determine the influence of single-triplet annihilation on the scaling laws of fluorescence emission as more fluorophore units are added, we can calculate the relative emission rates (I_{Fl}) of one-fluorophore (**1,2**) two-fluorophore (**3**) and four-fluorophore (**4,5**) complexes as a function of the microscopic kinetic parameters discussed above and summarized in Figure 6b. Steady state populations of each site, *i*, with a total of N sites are calculated as functions of k_{obs}, k_{isc}, k_{T}, k_{ST}, and excitation intensity, P_{ex}, for each state using the following differential rate law which was derived from the hybrid Jablonksi diagram, Figure 6b:

$$\frac{\partial S_{1,i}}{\partial t} = P_{ex}S_{0,i} - k_{obs}S_{1,i} - k_{isc}S_{1,i} - \sum_{j\neq i}^{N} k_{ST}S_{1,i}T_{1,j} \qquad \text{Equation 8}$$

$$\frac{\partial S_{0,i}}{\partial t} = k_{obs}S_{1,i} + k_{T}T_{1,i} - P_{ex}S_{0,i} + \sum_{j\neq i}^{N} k_{ST}S_{1,i}T_{1,j} \qquad \text{Equation 9}$$

$$\frac{\partial T_{1,i}}{\partial t} = k_{isc}S_{1,i} - k_{T}T_{1,i} \qquad \text{Equation 10}$$

$$I_{Fl} \propto \sum_{i}^{N} k_{obs}S_{1,i,SS} \qquad \text{Equation 11}$$

A single site system or a system with negligible single-triplet annihilation will have the summation terms vanish.

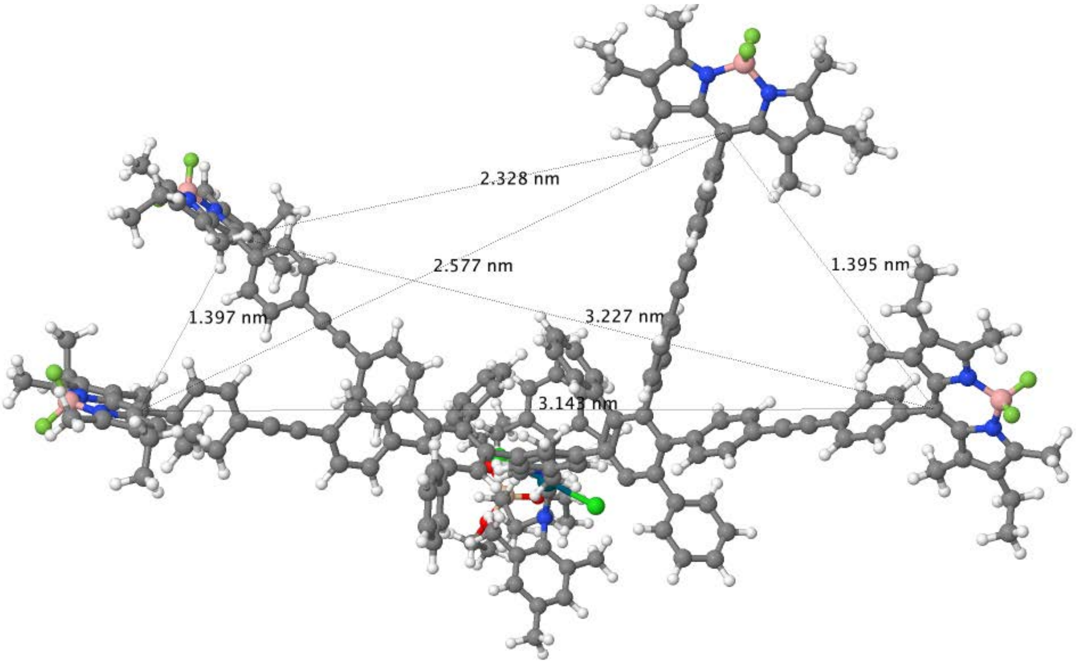

Figure 10: The optimized structure of **4**. Distances between chromophores are shown in the figure in nm.

Equation 8 to Equation 10 were solved to determine the steady state populations of S_0, S_1, and T_1 for each individual site with 1, 2 or 4 total fluorophore sites. Of particular interest is S_1, as it can be related to fluorescence intensity through Equation 11. The equation for the steady-state population of S_1 for each case is presented below:

$$S_1 = \frac{k_T P_{ex}}{k_{isc}k_T + k_{obs}k_T + k_{isc}P_{ex} + k_T P_{ex}} \qquad \text{Equation 12}$$

$$S_{1,2site} = -\frac{k_{isc}k_T + k_{obs}k_T + k_{isc}P_{ex} + k_T P_{ex} - \begin{bmatrix} k_{isc}^2 k_T^2 + 2k_{isc}^2 k_T P_{ex} + k_{isc}^2 P_{ex}^2 + 2k_{isc}k_{obs}k_T^2 + 2k_{isc}k_{obs}k_T P_{ex} + 2k_{isc}k_T^2 P_{ex} \\ +2k_{isc}k_T P_{ex}^2 + 4k_{ST}k_{isc}k_T P_{ex} + k_{obs}^2 k_T^2 + 2k_{obs}k_T^2 P_{ex} + k_T^2 P_{ex}^2 \end{bmatrix}^{1/2}}{2k_{isc}k_{ST}} \qquad \text{Equation 13}$$

$$S_{1,4site} = -\frac{k_{isc}k_T + k_{obs}k_T + k_{isc}P_{ex} + k_T P_{ex} - \begin{bmatrix} k_{isc}^2 k_T^2 + k_{isc}^2 k_T P_{ex} + k_{isc}^2 P_{ex}^2 + k_{isc}k_{obs}k_T^2 \\ +2k_{isc}k_{obs}k_T P_{ex} \\ +2k_{isc}k_T^2 P_{ex} + 2k_{isc}k_T P_{ex}^2 \\ +12k_{ST}k_{isc}k_T P_{ex} + k_{obs}^2 k_T^2 \\ +2k_{obs}k_T^2 P_{ex} + k_T^2 P_{ex}^2 \end{bmatrix}^{1/2}}{6k_{isc}k_{ST}} \qquad \text{Equation 14}$$

To determine the emission rate scaling laws, values for the microscopic kinetic factors must be found. A value for k_{obs} (τ_{obs}) has been determined to be 0.167 ns^{-1} (6 ns).[104-107] Montejano and coworkers have extensively characterized the triplet state of several similarly functionalized BODIPY chromophores and have experimentally determined k_T (τ_T) to be approximately 2.5 x 10^{-5} ns^{-1} (40 μs).[102] Values for k_{isc} (τ_{isc}) appear to vary significantly between very similar BODIPY chromophores, with time constants (τ_{ISC}) ranging from 650 to 3000 ns.[51, 108-109] However, the saturation curves shown in Figure 7 provide an additional constraint for parameter selection as well as conspicuous proof of the existence of a long-lived excited state. We explored small deviations from the literature values for k_T and k_{isc} to represent the saturation curves in Figure 7. The determined values are listed in the caption of Figure 11 and demonstrate only minor deviations from literature values.

The values for the rates of these kinetic processes form a basis for simulating the excited state populations and ultimately for understanding the observed scaling laws for our compounds. Specifically, we can determine the influence of S-T annihilation on the observed emission intensity ratio. We can also examine the sensitivity of the scaling law to small changes in the required input parameters. Because there are five input parameters, we can use a series of contour plots to describe the five dimensional parameter space and gain insight into the populations and dynamics, Figure 11. Figure 11a shows the expected ratio between the four site (**4, 5**) and one site (**1, 2**) emission intensities as a function of the parameters that most directly influence the single-triplet annihilation rate, the return rate (k_T) from the triplet state which determines the triplet lifetime and the bimolecular annihilation rate (k_{ST}), calculated above. Weak electronic interactions between sites (low k_{ST}) or extremely short-lived triplets (high k_T) result in the expected linear scaling laws and a ratio approaching four. In the opposite case, the existence of single-triplet annihilation manifests as a significant detriment to emission, with the addition of more fluorophores providing more conduits for quenching. Critically, in the middle of the plot (red circle) at the most likely experimental values, a wide range of values yield a ratio near unity. In this regime, the inclusion of more fluorophores results in minimal change to the observed emission intensity and single-molecule brightness, as observed. Similar contours are demonstrated for a two site to one site emission intensity ratio and show an expected intensity ratio just below unity, as shown in Figure 11d-f. The following discussion will focus on Figure 11a-c as the 4 site system is our main focus but the statements made are generalizable to the 2 site system.

Figure 11b shows the influence on the emission rate ratio of the processes depleting the singlet excited state, k_{ISC} and k_{obs}. As expected, a high k_{obs} will return the expected linear scaling as the entire triplet manifold is made less relevant. When k_{obs} is restricted to its previously determined value (at the center of the axis), increasing k_{ISC} at low values of k_{ISC} results in a sharp decrease of the emission ratio as this increase directly translates into a higher triplet population and thus a higher rate of S-T annihilation. At unphysically high values of k_{ISC} where the QY of triplet formation is comparable to the QY of decay to the ground state, the ratio begins to slowly increase again. In this regime, intersystem crossing gradually becomes the dominant pathway depleting the singlet excited state, slowly diluting the influence of annihilation, and asymptotically returning the linear rate ratio. Importantly, the rate of change (slope) of the intensity ratio with k_{ISC}, the most uncertain parameter in our analysis, is fairly low (flat) in the most relevant region of the parameter space, suggesting the observed unity rate ratio is relatively insensitive to this parameter.

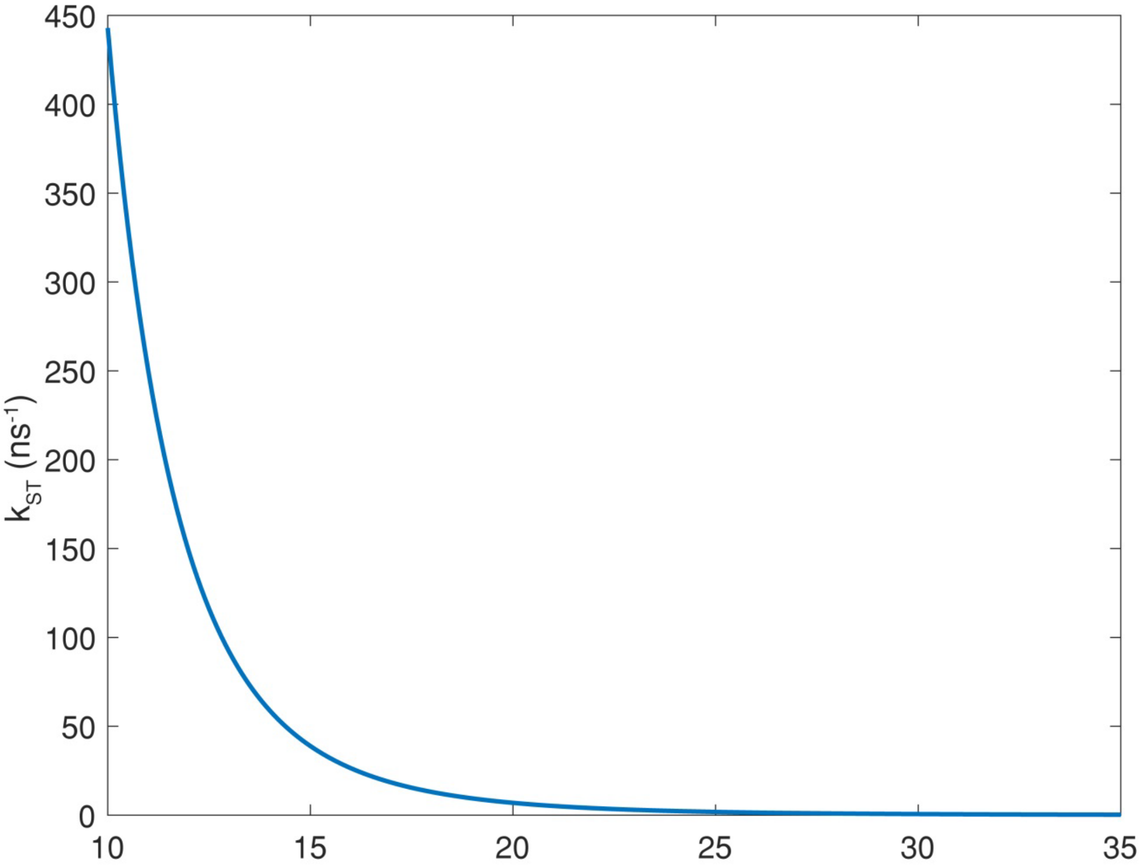

Figure 11: k_{ST} vs interchromophoric distance, determined using Equation 7.

Figure 11c shows the influence on the emission rate ratio of k_{ST} and excitation rate, P_{ex}. The role of k_{ST} has been described above. At extremely low excitation rates (excitation powers), the influence of S- T annihilation is minimal since the equilibrium population of triplet is low, leading to gradual recovery of the expected linear scaling law. At extremely high excitation rates, the linear scaling law is also gradually recovered as the transitions become saturated, with each saturated fluorophore unit essentially contributing independently. However, accessing the regimes where scaling deviates significantly from unity requires working at either inconveniently low excitation intensities where single-molecule detection is difficult, or very high intensities where photobleaching becomes a significant concern.

The center regions of Figure 11 correspond to the independently determined parameter values and to a parameter space region where increasing the number of fluorophore units has only a minor influence on the brightness of the individual molecules. The scatter in maximum brightness levels due to shifting conformations, Figure 5, prohibits resolving small brightness changes. Of the five input parameters, one is taken directly from literature values (k_{obs}), one is determined using literature spectra and computationally determined geometries (k_{ST}), one is

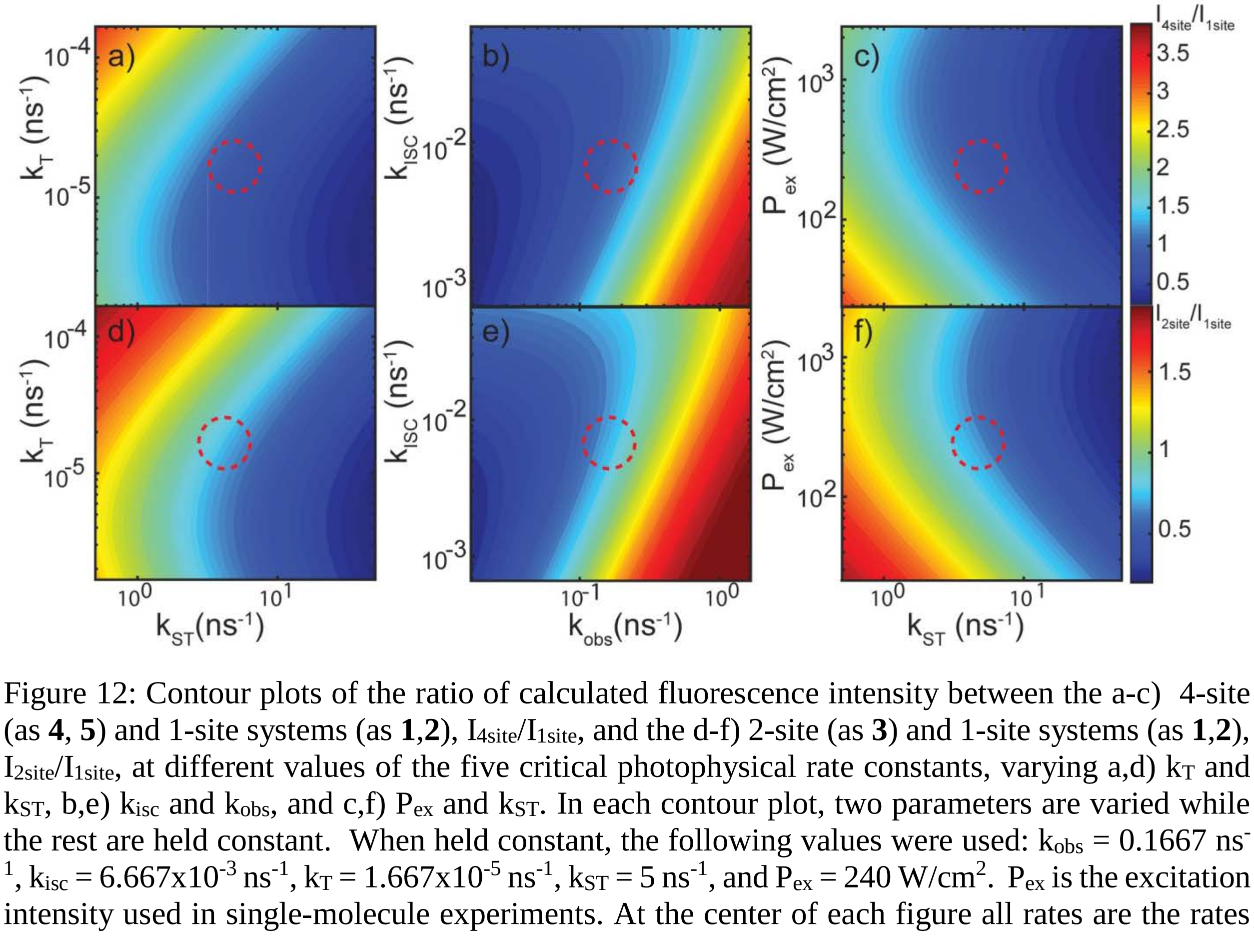

Figure 12: Contour plots of the ratio of calculated fluorescence intensity between the a-c) 4-site (as **4**, **5**) and 1-site systems (as **1**,**2**), I_{4site}/I_{1site}, and the d-f) 2-site (as **3**) and 1-site systems (as **1**,**2**), I_{2site}/I_{1site}, at different values of the five critical photophysical rate constants, varying a,d) k_T and k_{ST}, b,e) k_{isc} and k_{obs}, and c,f) P_{ex} and k_{ST}. In each contour plot, two parameters are varied while the rest are held constant. When held constant, the following values were used: $k_{obs} = 0.1667$ ns^{-1}, $k_{isc} = 6.667\text{x}10^{-3}$ ns^{-1}, $k_T = 1.667\text{x}10^{-5}$ ns^{-1}, $k_{ST} = 5$ ns^{-1}, and $P_{ex} = 240$ W/cm^2. P_{ex} is the excitation intensity used in single-molecule experiments. At the center of each figure all rates are the rates above. Note that the ratio in the neighborhood about this central value, as highlighted in the red dashed line, shows little variation.

experimentally controlled and easily determined (P_{ex}), and two ($k_{ISC,}$ k_T) are corroborated by saturation curves but are very close to literature values. The center regions of the contour plots in Figure 11 are sufficiently flat that small variations in these parameters between molecules due to minor electronic structure changes or differences in chain length (as in compound **3** and **5**) are not capable of pushing the system into a region where the ratio deviates substantially from one, suggesting this behavior is robust to shifts in parameter values. These simulations demonstrate that S-T annihilation is the likely origin for the unexpected scaling law.

S-T annihilation also provides a likely explanation for the quenching observed in **4** and **5** at high concentrations in solution, since J-aggregation cannot induce quenching and there is no evidence of H-aggregation. Excitons formed on an aggregate would be able to sample many more sites than in a monomer, giving them a higher probability of encountering a triplet and annihilating, even under those less intense excitation conditions.

Finally, though singlet-singlet annihilation can also influence fluorescence intensity and scaling laws,[58] it is not believed to be a significant contributor here due to the low excitation intensity. Indeed, when Equation 8 is solved at the steady state for the one site system, the equilibrium population in the S_1 state is less than 0.1%. Thus it is highly unlikely that two fluorophores in the same molecule will both be in the S_1 state at any given time, sharply reducing the impact of singlet-singlet annihilation. In contrast, it is the long lifetimes of the triplet state that make S-T annihilation so effective. At significantly higher excitation intensities, single-singlet annihilation has been shown to be an important contributor.[58]

2.8 Conclusions

We synthesized and characterized a new family of dendrimeric fluorescently-labeled surface-supported molecular catalysts. While our initial goal was to create brighter compounds for single-molecule mechanistic investigations of catalysis, we discovered an unusual scaling law where the attachment of individual fluorophores did not result in an increase in brightness at the single-molecule level. Through the use of simulations of photodynamics with independently determined input parameters, we showed that S-T annihilation was the likely origin of the observed scaling law.

To produce a system that *does* allow the addition of multiple fluorophores in a single molecular unit to yield brighter molecules for single-molecule investigations, the effect of S-T annihilation must be counter-acted. In general, achieving this result requires slowing the rate of S-T annihilation by reducing the rate constant k_{ST} or the triplet population in the bimolecular term in the rate laws in Equation 8 and Equation 9. k_{ST} can be reduced by using rigid, and longer linkers between fluorophores or choosing fluorophores with a lower overlap integral between the S_1 emission and T_1 absorption spectra. A lower value of k_{ST} directly translates into a more additive scaling law, Figure 11a. Alternatively, fluorophores with shorter S_1 or T_1 lifetimes, as well as slower internal conversion rates, would decrease the triplet population, the likelihood of S-T annihilation occurring, and thus recover the more additive scaling law, Figure 11a and b.

The photophysics of multichromophoric systems is highly dependent on the excitation conditions, with qualitatively different behaviors readily observed. Most steady-state photoemission techniques uniquely probe a low excitation population regime. Higher excitation population regimes can be probed at the ensemble level via ultrafast transient absorption techniques, where high peak powers can be used to populate chromophore assemblies with multiple excitons, leading to new quenching pathways, such as singlet-singlet annihilation. However, bulk spectroscopies that probe the high excitation population regime are typically transient techniques, and fail to probe the equilibrium state. Single-molecule measurements provide a convenient way of probing the equilibrium behavior in the multi-excitation regime. Under these conditions, rare processes, such as formation of triplet states when intersystem crossing is slow, acquire an amplified importance. In this regime these processes can profoundly influence the available photophysical pathways. Our work shows that these new pathways have important consequences for the scaling behavior of multichromophoric assemblies and therefore, is a highly relevant consideration in molecular design strategies for light harvesting materials.

2.9 Acknowledgements

This work was supported by the NSF via CHE-1254936 and through the University of Wisconsin Materials Research Science and Engineering Center (UW-MRSEC, DMR-1121288). Computational work was supported by NSF Grant CHE-0840494.

3. Probing Heterogeneity and Bonding at Silica Surfaces through Single-Molecule Investigation of Base-Mediated Linkage Failure

This chapter was first published as Lupo, K. M.; Hinton, D. A.; Ng, J. D.; Padilla, N. A.; Goldsmith, R. H., Probing Heterogeneity and Bonding at Silica Surfaces through Single-Molecule Investigation of Base-Mediated Linkage Failure. *Langmuir* **2016,** *32* (36), 9171-9179.

Katherine Lupo performed single-molecule studies and modelled saturation kinetics. Daniel Hinton synthesized compound **6**.

3.1 Abstract

The nature of silica surfaces is relevant to many chemical systems, including heterogeneous catalysis and chromatographies utilizing functionalized-silica stationary phases. Surface linkages must be robust to achieve wide and reliable applicability. However, silyl-ether silica support linkages are known to be susceptible to detachment when exposed to basic conditions. We use single-molecule spectroscopy to examine the rate of surface linkage failure upon exposure to base at a variety of deposition conditions. Kinetic analysis elucidates the role of thermal annealing and addition of blocking layers in increasing stability. Critically, it was found that successful surface modification strategies alter the rate at which base molecules approach the silica surface as opposed to reducing surface linkage reactivity. Our results also demonstrate that the innate structural diversity of the silica surface is likely the cause of observed heterogeneity in surface-linkage disruption kinetics.

3.2 Introduction

Attaching molecular catalysts to heterogeneous supports combines the efficacy and selectivity of homogeneous molecular catalysts with the reusability of heterogeneous catalysts.[110-111] Interactions between the surface and the supported molecular catalyst can add new functionality[111-112] and these supported molecular catalysts have become important tools in catalysis technology, particularly for in-flow reactors[113-114] and electrochemical transformations.[115-116] One critical figure of merit for a supported molecular catalyst is over how many cycles the catalyst can be used before its activity suffers. There are several factors that can contribute to loss of activity, with major origins including detachment of the molecular catalyst from the heterogeneous support[117] and the leaching of metal ions into the reaction mixture.[118]

A variety of methods exist to characterize the activity of molecular catalysts on surfaces. Recyclability studies can quantify changes in catalyst activity as a function of reaction cycle.[119-121] Of critical interest is whether the catalytic activity is due to the supported catalyst or whether a soluble species forms that is responsible for the catalytic activity.[122-124] However, while many studies assess the degree to which catalyst performance degrades, they may not provide insight into the nature of the degradation. Additionally, by necessity most studies are performed *after* the reaction occurs, thus eliminating the possibility of real-time monitoring of the state of the catalysts. While most investigation of deactivation of surface-supported catalysts has focused on leaching,[118, 125] an often overlooked issue is the malfunction of the surface anchor.[117] If the surface support is severed, the catalyst essentially becomes homogeneous, eliminating the benefits of having a supported catalyst.

More broadly, in addition to its use for catalysis, surface anchoring is an important tool in many applied chemical systems, particularly for chromatography. Silica stationary phases are modified in various ways to facilitate reverse-phase,[126] chiral,[127] and ion separation[128] chromatographies. Separations at high pH have become particularly important in separations critical for proteomics,[129] but basic mobile phases can degrade silica packing materials,[130-131] suggesting tremendous benefit to further understanding of the origins of chemical degradation at silica interfaces.

Given the importance of silica functionalization, it is critical to understand modes of surface-anchor failure. Thus, methods capable of interrogation of surface attachments are valuable tools, and include X-ray photoelectron spectroscopy (XPS) analysis, contact angle analysis, and IR spectroscopy. All three have been used to investigate silyl-ether surface linkages, including determination of chemical composition, thickness,[132] stability,[133] and wettability[134] of thin films. However, XPS must be performed under vacuum[132] and can be damaging to thin layers on substrates,[135] while contact angle analysis may vary based on measurement technique[136] and lacks chemical specificity. Importantly, these ensemble-averaged techniques lack the ability to discern unsynchronized surface chemical events. In this capacity, single-molecule microscopy provides an ideal way to characterize surfaces and has been directed toward understanding silica-molecule interactions[137] and model-systems for chromatography.[15-17, 42, 44] Spatial distributions,[42, 138] adsorption/desorption events,[16, 43, 139-140] and diffusion rates[16-17, 42, 141-142] in both silica particles and at silica surfaces have all been examined through single-molecule imaging. Single-molecule microscopy provides a means of examining surfaces in real time under relevant chemical conditions, recording individual molecular trajectories, and granting both temporal and spatial resolution. Dynamics of molecules at the surface can be assessed, providing a more complete view of the surface's properties.

Here, we examine a silyl ether-silica surface linkage that has been used for anchoring supported molecular catalysts[143-144] as well as for enabling surface functionalization for chromatography,[129] where the stability of the catalyst or stationary phase in an alkaline environment is a crucial issue. We employ single-molecule fluorescence imaging to allow characterization of unsynchronized chemical processes occurring at surfaces.[45, 145] In previous works, we have investigated the photophysical behavior of a fluorescently labeled molecular catalyst[146] and reported on catalyst initiation kinetics at the single-molecule level,[20] finding highly non-exponential kinetics indicative of chemical heterogeneity. Surprisingly, heterogeneity in the catalyst population appeared to change depending on added base concentration despite identical surface deposition conditions, and a model was proposed that demonstrated how a dynamic observed heterogeneity can derive from a static structural heterogeneity in a two-step mechanism.[20] However, it was also found that the silyl ether surface linkage is susceptible to being severed from the silica surface, as has been previously observed.[147] Here, we probe the mechanism of surface-support disruption at a silica surface by base using single-molecule microscopy.

The surface stability of a silyl ether-silica linkage in response to basic conditions was investigated using a surface-linked boron-dipyrromethane (BODIPY) molecule (compound **6**, see Figure 12c) as a probe, whose synthesis has been previously reported.[20] Widefield fluorescence microscopy in a pseudo- total internal reflectance (TIRF) mode was employed to report on dynamics of single molecules of **6** attached to a silica surface. At the surface, **6** will fluoresce, but molecules in the bulk solution, away from the surface, will not be excited. This dichotomy allows facile determination of events where molecules of **6** detach from the surface, thus allowing examination of the kinetics of the removal of **6** from the surface in response to increasingly basic conditions. We selected potassium tert-butoxide (KOtBu) as a target base because it is an effective base for Suzuki reactions in isopropanol[148] and is highly soluble in isopropanol, where isopropoxide is rapidly formed. Figure 12a shows an example of a widefield image of single molecules of **6.** The nature of the linkage between the molecular species and surface support is an important consideration when designing surface-supported catalysts. A variety of deposition conditions are employed in the literature for attaching silyl ether functionality to silica surfaces, differing significantly in time of reaction, temperature, and use of blocking layers.[149-152] To systematically investigate the influence of different conditions, three alkylsiloxane surface support

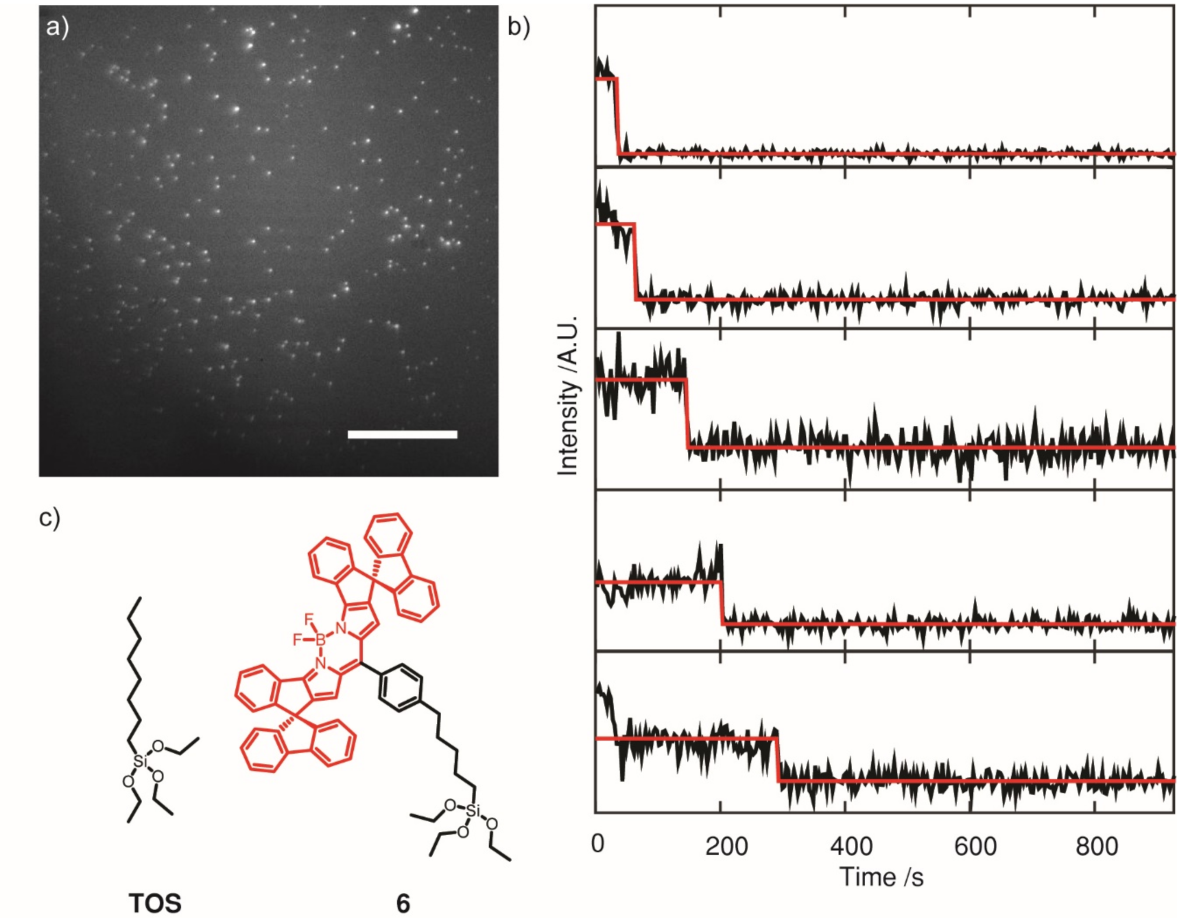

Figure 13: Examples of obtained data. a) One frame of a video of single-molecule dynamics. Scale bar is 20 µm. Multi-pixel regions of interest around each point capture the emission from a single probe molecule, with fluorescence intensity dynamics shown in traces, b). c) Structures of compound **6** and TOS before surface attachment.

deposition schemes were used, varying the use of thermal annealing and use of an alkylsiloxane blocking layer. In the first two procedures, only the alkylsiloxane-functionalized probe molecule, compound **6**, is deposited with no silane blocking layer, with one procedure undertaken solely at room temperature (no heat no silane, NHNS) and the other including a post-deposition heating step (heat, no silane, HNS). In the third deposition procedure, **6** is co-deposited with a high concentration of a commercially available alkylsiloxane, triethoxyl octyl silane (TOS, see Figure 12c), to create a nonpolar barrier which helps resist base attack.[153] These samples are termed HS (for their inclusion of the TOS blocking layer) and were thermally annealed like the HNS sample after the initial deposition. By investigating samples with and without a heating step, the effect of heating on the strength of the surface bond is investigated. It has been shown that hydrogen bonding may be a major mode of surface attachment in unheated films and that heat curing produces covalently bound siloxane.[154-155] Thus, surface attachment may be represented by the mechanism shown in Figure 13a and a thermal annealing step may be necessary to ensure a stable surface bond. Two places are left ambiguous in the mechanism: 1) the state of the silyl ether most strongly electrostatically interacting with the surface, which may or may not have been hydrolyzed by surface water,[154] and 2) the state of the remaining geminal silyl ether linkages after covalent attachment of one silyl ether to the surface, which also may or may not have been hydrolyzed, assuming another surface site is not available. Inclusion of the blocking layer also allows evaluation of the role of a steric obstacle in determining disruption kinetics. More broadly, investigating the surface stability of the alkylsiloxy linkage at three deposition conditions when exposed to base allows us to characterize the bonding landscape of the silica surface.

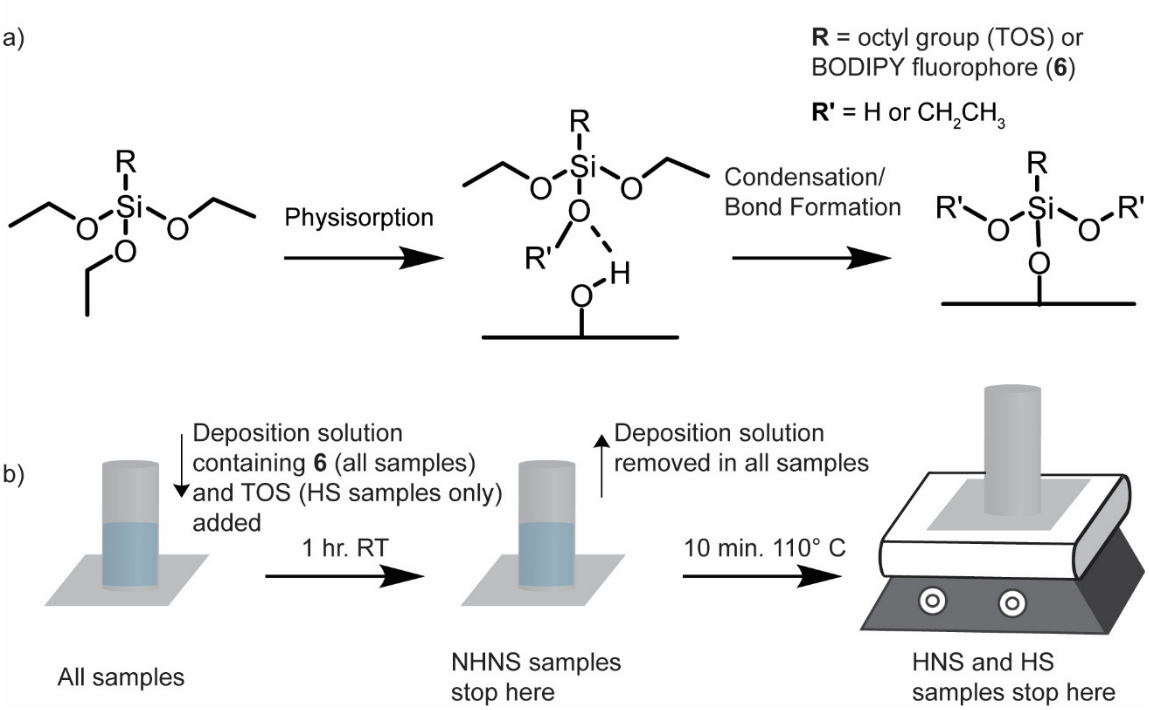

Figure 14: Mechanism of bond formation and sample fabrication. a) Suggested mechanism for bond formation between an alkylsiloxane and bare silica surface including physisorption step, where hydrogen bonding is the principle means of attaching the alkylsiloxane to the surface, and a thermal annealing step, where covalent bond formation occurs. b) shows a simplified procedure for depositing compound 6 at the silica surface. The grey cylinder represents an all-glass sample chamber composed of a glass cylinder bound to a glass coverslip. Full details of the fabrication of the sample chamber are presented in Ref. 44.

3.3 Experimental

3.3.1 Reagents and Cleaning Procedures

Compound **6** was synthesized as previously reported.[20] HPLC grade isopropanol was photobleached in a home-made photobleaching apparatus for 3 days before use[80, 146] and used for preparation of all solutions, including KOtBu (Sigma) stock solutions and deposition solutions. TOS was obtained from Sigma at 95% purity and used without further purification. Previously described all-glass sample chambers were used for single-molecule microscopy studies.[146] Prior to use, all glassware was cleaned by rinsing with HPLC methanol, acetone, and methanol followed by O_2 plasma cleaning for 3 minutes at 300 W.

3.3.2 Sample Deposition

A schematic of the sample deposition procedure is shown in Figure 13b. Samples were prepared under three conditions: no added blocking layer and no heating step (NHNS samples), no added blocking layer, but including a heating step (HNS samples) and including a blocking layer of TOS as well as a heating step (HS samples). All samples are prepared by first placing 500 mL of a deposition solution containing low concentrations of **6** into a sample chamber. Deposition solutions were prepared by taking small volumes of a stock solution, prepared by dissolving a small amount (sub-mg) of **6** in isopropanol, and dissolving them in isopropanol (for NHNS and HNS samples) or a 5% by volume solution of TOS in isopropanol (for HS) prepared by adding 50 μL of TOS per 950 μL of isopropanol. The volume of stock solution required to produce surface coverages comparable to that seen in Figure 14d varied, but ranged between 4 to 20 μL per mL of solution. All samples were then left at room temperature under an opaque box for an hour. Concurrently, blank samples of each deposition condition were prepared identically except without **6** in the deposition solution. After the hour long deposition step, the deposition solution was pipetted out of the HNS and HS samples and the samples were placed on their side in a 110 °C oven for 10 minutes. Drying the chambers on their side allows impurities in the solvent to condense onto the side of the chambers rather than the bottom, greatly improving sample purity (see blanks below). Concurrently, the deposition solution was pipetted out of the NHNS samples and the samples were rinsed with several 800 μL aliquots of isopropanol. After taking the HNS and HS samples out of the oven and cooling them for several minutes, they were rinsed in the same fashion. After rinsing, all samples had 100 μL of isopropanol added back in.

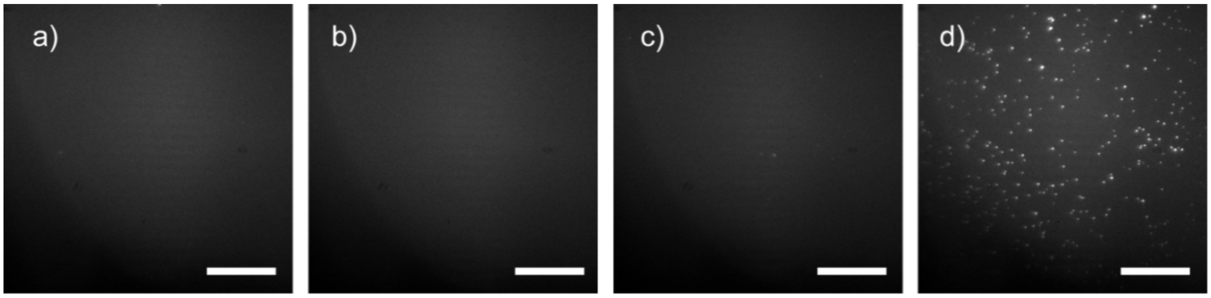

Figure 15: Comparison of control samples and an actual sample. a) NHNS blank, b) HNS blank, c) HS blank and d) NHNS sample containing **6**. All samples are at the same brightness and contrast levels. Scale bar is 20 μm.

A stock solution of 40 mM KOtBu in isopropanol was prepared. The same stock solution was used for all studies. Dilutions were prepared as needed directly before use. In between uses, the stock solution was kept in a -20 °C freezer.

3.3.3 Control Experiments

Single-molecule fluorescence measurements require systems with low levels of fluorescent impurities to ensure that only the analyte of interest is being studied. To this end, samples termed “blanks”, Figure 14, were prepared for every deposition condition by preparing samples without **6** that were otherwise treated identically to the samples with **6**. For NHNS samples, this meant using a deposition solution solely containing isopropanol. For HNS samples, again, the deposition solution was solely isopropanol, but the blank chamber was also heated to 110 °C, like HNS samples containing **6**. For HS samples, the deposition solution was a 5% solution of TOS in isopropanol and the samples were heated. TOS did not have to be purified to produce samples with low impurity levels.

To assess whether KOtBu had an effect on the quantum yield of **6** in isopropanol, bulk spectroscopic studies were performed on the non-surface functionalized version of **6**. As Figure 15 shows, fluorescence remains the same upon addition of concentrated KOtBu for a final concentration of 150 mM.

In Figure 2b of the main text, we show that there is uncertainty in the identity of the R’ groups. While we cannot easy directly determine the structure of the R’ groups at the surface, we can determine their identity in solution and use that as an indicator of the likely surface structure. Specifically, we used bulk NMR studies to assess whether the ethoxy groups hydrolyze in isopropanol to form hydroxyl groups, or if they stay intact in solution. A 5% by volume solution of TOS in deuterated isopropanol was spiked with water and left to sit in an NMR tube for an hour before an NMR spectrum (Figure 16) was taken to determine the degree of hydrolysis. The ratio between the methylene hydrogens alpha to the silicon (C) and the ethoxy hydrogens (A and B) is 2:6:9, indicating that three ethoxy groups exist on each molecule. Thus, any hydrolysis that occurs must happen at the surface, not in the bulk solution. Because any hydrolysis that occurs must involve strong interactions with the surface, the most likely form of the physisorbed species has at least two

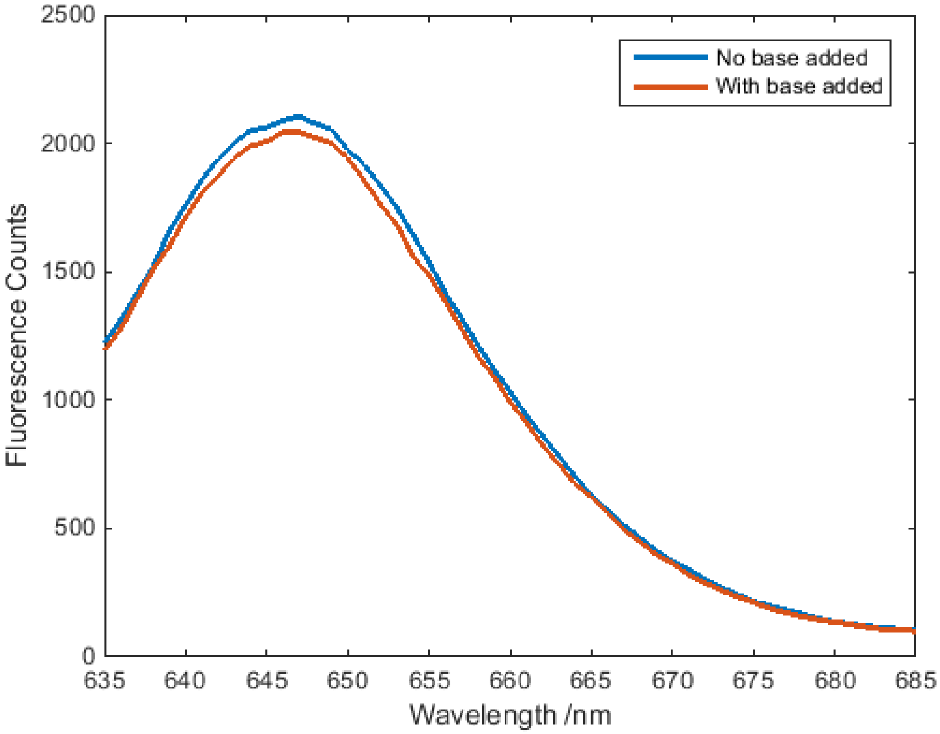

Figure 16: Bulk spectroscopic study showing that fluorescence of the BODIPY is not significantly affected by KOtBu.

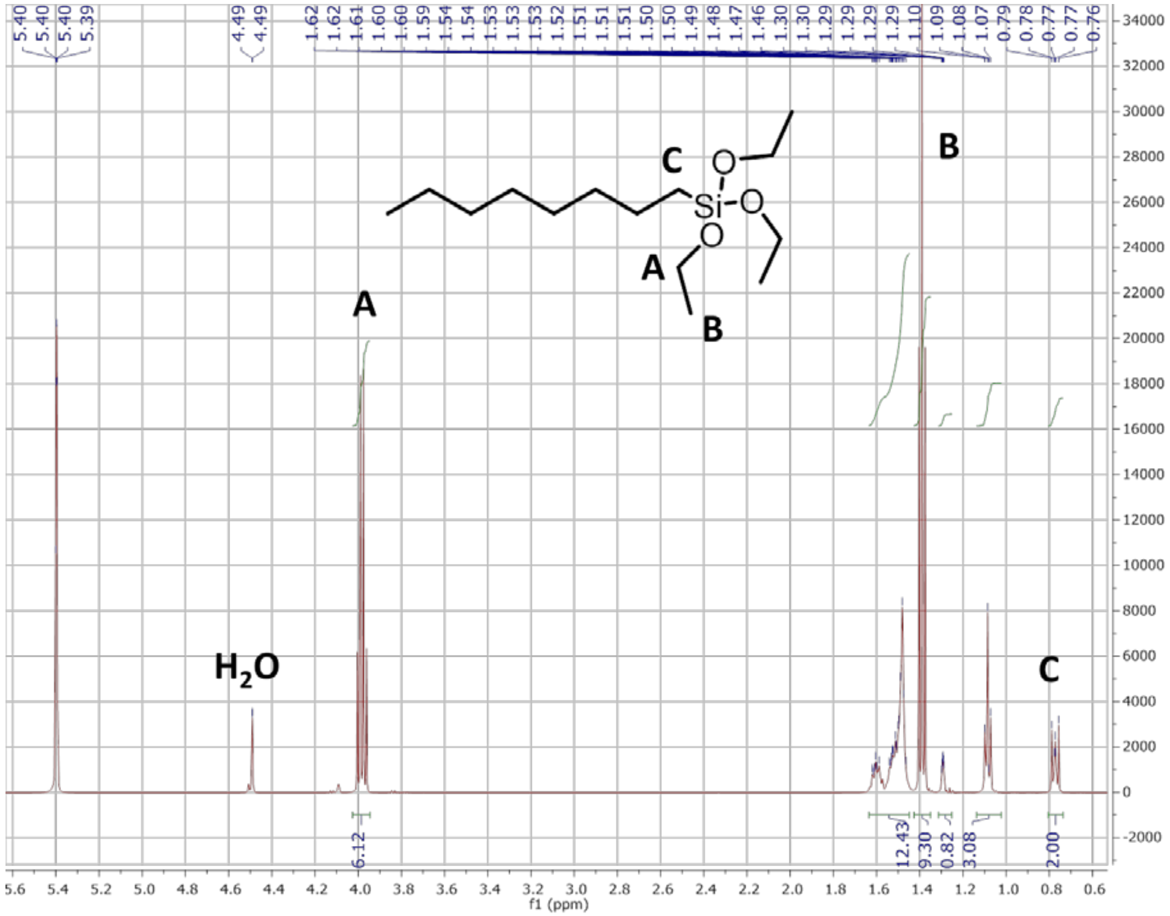

Figure 17: NMR spectrum of TOS in deuterated isopropanol, with a small amount of added water. Diagnostic peaks are labeled. The structure of TOS is overlayed.

ethoxy moieties, as indicated in Figure 2a, middle. While we think it is unlikely that hydrolysis changes the identity of R’ to hydroxyl groups when condensation occurs, it should be noted that the trend in k_1 (see section on Weibull Analysis, below) can still be rationalized with our model even if R’ is H. While hydrogen bonding would stabilize the base, the base would still be at a short distance from the surface as the hydrogen bond donor is at the alkylsiloxane group. In the physisorbed species, the hydrogen bonding would bring the base much closer to the surface as the hydrogen bond donor is at the surface silicon atom, facilitating the formation of the base-surface site species, suggesting that k_1 would still be faster in the NHNS samples than in the HNS samples.

3.3.4 Single-Molecule Microscopy

Single-molecule fluorescence microscopy was performed using pseudo-TIRF illumination on an inverted microscope as previously reported.[20] In brief, a 20 mW, 633 nm laser was used to excite an area of the sample plane of approximately 3000 μm^2. Fluorescent emission was passed through a 633 nm long pass filter before being focused onto an EM-CCD camera. Images with a 100 ms exposure time were captured every 3 seconds. Solutions of KOtBu (800 uL) were micropipeted into the chambers between the 10th and 11th frame. Because a relatively large volume of basic solution is added to a small volume of isopropanol already in each chamber, the solution in the chamber homogenizes within the three seconds between frames.[20] KOtBu solutions were prepared to achieve final concentrations of 40 μM, 400 μM, 4mM and 40 mM from a stock 40 mM KOtBu solution in isopropanol that was kept in a freezer between uses. All experiments were completed within a week of preparing the solution to prevent the KOtBu from degrading.

The addition of the base resulted in varying rates of surface anchor destruction. KOtBu deprotonates isopropanol to form a stoichiometric quantity of the active base, isopropoxide. To quantify the kinetics, first, the videos were analyzed to determine the location of single molecules (Figure 12a). The intensities over time of the found molecules were tracked, creating traces such as those shown in Figure 12b. Each trace was analyzed using a custom-written MatLab script to determine the frame of fluorescence loss for each molecule. For each video, the fraction of molecules fluorescing per frame was graphed, creating curves as shown in Figure 17a-e.

3.4 Data Analysis

Analysis of the time traces were performed using the same algorithm as is presented in Section 2.5.5, with minor modifications. For each fluorescent spot, 7x7 pixel regions of interest were analyzed. A 2 pixel border around each ROI was used as a local background. In some traces, such as the bottom trace in Figure 1b, there are additional minor intensity fluctuations that may originate from changes in the orientation of the molecule or changes in the molecule’s local environment, affecting its emission rate. Traces where the changes in intensity during emission are substantially larger than the change in intensity between the lowest level above background (bright) state and the background (loss of fluorescence) are assumed to come from multiple molecules and such traces are excluded from analysis. Blinking is treated in a similar fashion, where small, infrequent fluctuations to the background level are ignored but traces with frequent or long-lived blinking are rejected. In general, blinking will not affect the survival statistics because only the final irreversible “off” event is recorded. Because blinking is generally brief and uncommon using this dye, it is unlikely that a blinking event can be mistaken for a release event. Large intensity fluctuations are uncommon and the traces included in Figure 1b are representative of the data as a whole.

3.4.1 Number of Molecules Analyzed

Figure 3a-e in the main text shows normalized fractions of molecules, but each decay curve is built from hundreds of molecules. The number of molecules in each decay curve is shown below.

	No addition	40 μM	400 μM	4 mM	40 mM
NHNS	433	560	290	645	612
HNS	2215	566	606	515	753
HS	2031	662	711	565	827

Table 2: Number of Molecules per Decay Curve

3.5 Results and Discussion

As can be seen in Figure 17a-e, the addition of high concentrations of KOtBu results in a rapid loss of fluorescence, resulting from the removal of surface bound molecules from the surface into the bulk solution. As the concentration of KOtBu is decreased, the loss of fluorescence is more gradual indicating that molecules are being removed from the surface less rapidly. In the control experiment, where no base was added, there is still a gradual loss of fluorescence. This is likely caused by hydrolysis because water is not specifically excluded from the experimental setup.[133]

The effect of photobleaching is made minimal by imaging in a time-lapse manner with short illumination bursts separated by 3 second waiting periods while blocking the illumination between acquisitions. In total, each sample was illuminated for thirty seconds. In the samples where moderate or high concentrations of base are added, the contribution of photobleaching is negligible because of the fast base-induced dynamics, as seen in control experiments with the same dye where the kinetics were examined at different frame rates.[20] At the lower concentrations of added base (including the absence of base), photobleaching may exert a stronger influence. In the samples with no base added, hydrolysis and photobleaching are the only processes that cause a loss of fluorescence. If photobleaching were the dominant process, monoexponential decays would be expected (β =1, introduced below) since photobleaching is likely well represented by a one-step process without saturation kinetics. Non-monoexponential kinetics are seen, as discussed below, indicating that photobleaching is not a dominant process. However, though hydrolysis can be treated similarly to base-induced lysis by a two-step saturation mechanism, under these conditions the terms responsible for a $\beta < 1$ are not dominant, also suggesting a β close 1 will be present. However, deposition condition should not affect the rate of photobleaching, and so differences between the decay curves for different conditions observed in Figure 3) e,j suggest that hydrolysis is the dominant process occurring here. Thus, the β value produced in the Weibull fit of the no-base-added samples stem from a combination of a minor contribution of monoexponential photobleaching and a major contribution of nearly monoexponential hydrolysis. Under these conditions, photobleaching may play a minor role in artificially raising the observed β value extracted from Weibull fitting, resulting in slightly steeper curve in Figure 4a than would be produced if photobleaching were not present. However, the overall trend in β that is conspicuously observed at moderate and higher concentrations of base where photobleaching does not a play a role persists, suggesting that that photobleaching plays a mimimal role in our mechanistic analysis. Thus, the effects of photobleaching are deemed to have a minor role.

3.5.1 Weibull Analysis

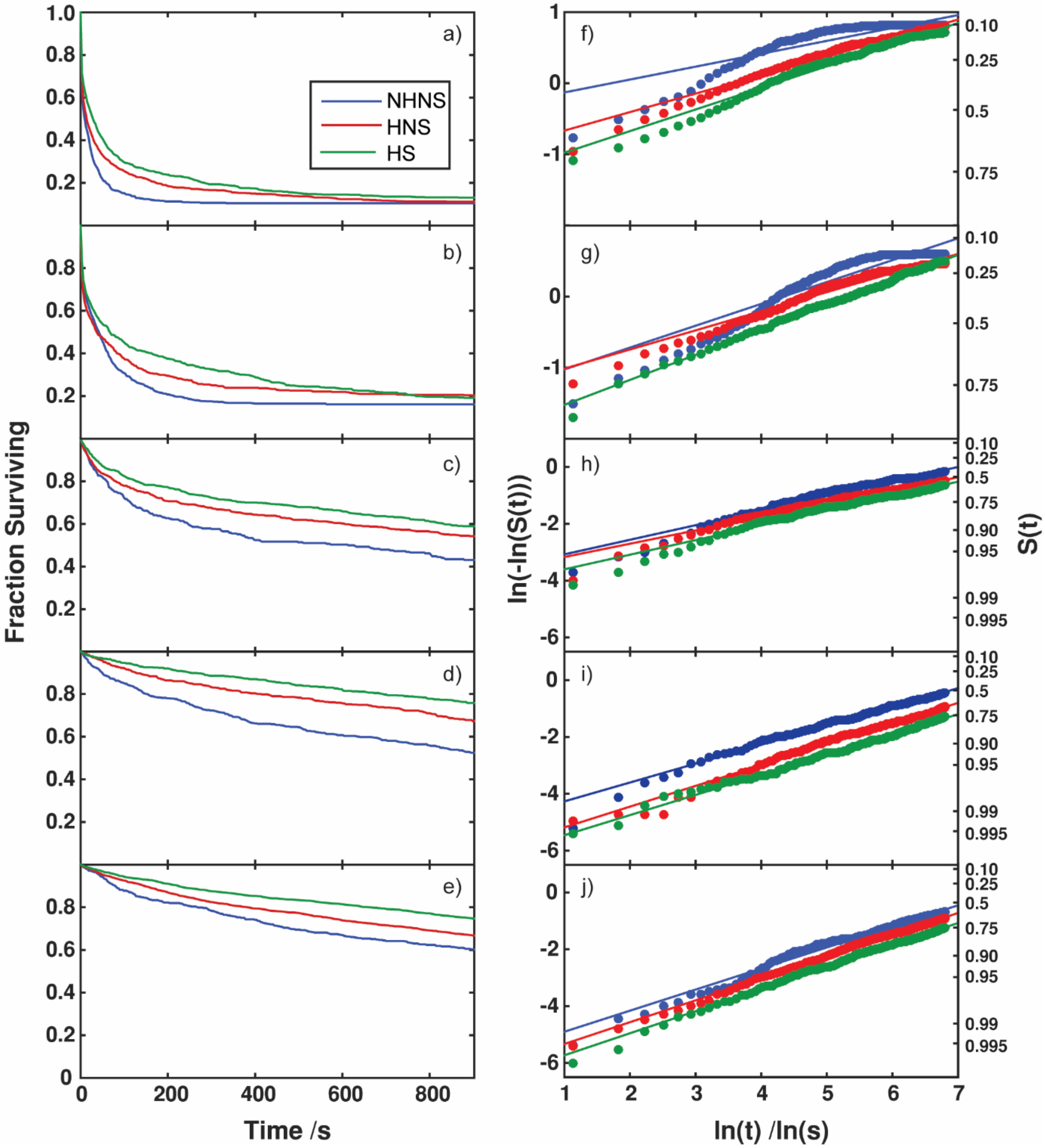

Figure 18: a-e) Survival fraction versus time. f-j) linearized Weibull plots of the corresponding decay curve with linear fits. Final concentrations of KOtBu are as follows: a, f) 40 mM, b, g) 4 mM, c,h) 400 µM , d,i) 40 µM, and e, j) none. In f-j), data is shown as closed circles and fits are shown as lines.

The declining fraction of surface-supported fluorescent molecules surviving as a function of time demonstrates conspicuously non-exponential kinetics. Stretched-exponential kinetics have been previously used to model the dynamics of molecules at surfaces and Weibull analysis is a convenient means of clearly displaying and quantifying stretched-exponential behavior.[8, 20] In Weibull analysis, the stretched exponential describing the decaying surviving fraction, S(t), in Equation 15 is linearized by taking a double natural logarithm, Equation 16,

$$S(t) = e^{-(k_{eff}t)^{\beta}} \qquad \text{Equation 15}$$

$$ln\big(-ln\big(S(t)\big)\big) = \beta lnt - \beta ln(\frac{1}{k_{eff}}) \qquad \text{Equation 16}$$

where β is a shape parameter and k_{eff} is a scale parameter.[156] More specifically, β indicates the degree to which a curve is non-monoexponential, with β equal to 1 indicative of monoexponential kinetics. The effective rate of loss of **6** from the surface is given by k_{eff}. The inverse of k_{eff}, τ_{eff}, indicates the effective lifetime of **6**. (The quantity τ_{eff} is distinct from the median lifetime, $\tau_{1/2}$, which is given by the equation

$$\tau_{1/2} = \frac{(ln2)^{1/\beta}}{k_{eff}} \qquad \text{Equation 17}$$

Whenever lifetime is mentioned, it is referring to the effective lifetime, τ_{eff}, and not the median lifetime, $\tau_{1/2}$.) Survival fractions after base addition were analyzed via Weibull analysis (Figure 17f-j). In most cases, the decays were well fit as lines, indicating that they demonstrate stretched exponential behavior. Minor deviations are sometimes observed at early times, but these data points account for only small fractions of the data set, as quantified on the right ordinate axis.

At the highest concentration of base added, the Weibull curves at all three deposition conditions deviate from linearity. Stretched exponential kinetics are observed when molecular contributors exhibit a distribution of rate constants formally described by a Weibull distribution.[157-158] Thus, stretched exponential kinetics with β <1 are indicative of heterogeneity in molecular behavior.[8, 20] However, non-linear behavior on a Weibull plot is likely still indicative of a distribution of molecular behaviors, but with a non-trivial population distribution shape deviating significantly from a Weibull distribution.

To quantify the difference in behavior between each sample, values for β and τ_{eff} were extracted from each linear fit. As Figure 18 shows, the general trend of decreasing β and logarithmically decreasing τ_{eff} with increasing base concentration holds for all deposition conditions. However, there are also trends apparent *between* each deposition condition. The HS samples consistently exhibited the highest τ_{eff} values for each base concentration added, followed by the HNS condition, with the NHNS samples degrading most rapidly, indicating that the TOS modified surfaces were the most resistant to base attack. The trend for β is less clear, with β values decreasing as base concentration is increased, but remaining tightly clustered between different deposition protocols.

3.5.2 Error Analysis for β and τ_{eff}

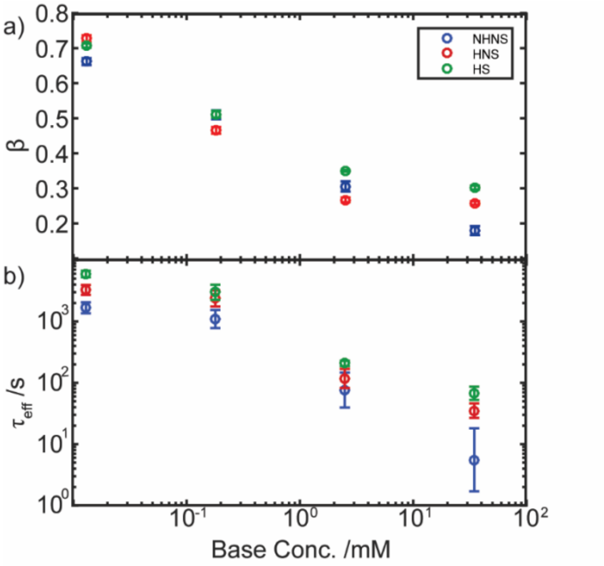

Figure 19: a) beta values and b) effective lifetimes of decay curves derived from the linearized Weibull fits shown in Figure 17. Error bars represent 95% confidence intervals.

β and τ_{eff} were found using MatLab's Curve Fitting toolbox by fitting the equation $y=mx+b$ to the linearized data, where $m=\beta$ and $b=-\beta\ln(\tau_{eff})$. The MatLab Curve Fitting toolbox calculates 95% confidence intervals for m and b. Because $m=\beta$, the 95% confidence intervals for β are the same as those for m. Because τ_{eff} is a function of both m and b, contributions in error from both m and b must be included in the 95% confidence interval for τ_{eff}. Generally,

$$\sigma^2_{F(x,y)} = (\frac{\delta F}{\delta x})^2\sigma^2_x + (\frac{\delta F}{\delta y})^2\sigma^2_x + 2(\frac{\delta F}{\delta x})(\frac{\delta F}{\delta y})\sigma_{xy} \qquad \text{Equation 18}$$

τ_{eff}= $e^{-b/m}$, so Equation 18 becomes:

$$\sigma^2_{\tau_{eff}} = \left(\tau_{eff}\right)^2\frac{b^2}{m^4}\sigma^2_m + \left(\tau_{eff}\right)^2\frac{1}{m^2}\sigma^2_b - 2\left(\tau_{eff}\right)^2\frac{b}{m^3}\sigma_m\sigma_b \qquad \text{Equation 19}$$

Because Matlab provides 95% confidence intervals and not variances, the variances of m and b must first be found before $\sigma^2_{\tau_{eff}}$ can be found. To find the variance, $^{\sigma 2}$, for m and b, the Equation 20 and Equation 21were solved for σ_q. Both equations yield the same value for the variance.

$$lb = q * e^{-norminv(0.05)*\sigma_q/q} \qquad \text{Equation 20}$$

$$ub = q * e^{norminv(0.05)*\sigma_q/q} \qquad \text{Equation 21}$$

Where lb and ub are the 95% confidence intervals, q is either m or b, and norminv(0.05) is the cutoff value for a two-tailed inverse normal Gaussian distribution and is equal to 1.96. Once $\sigma_{\tau_{eff}}$was found, it was used to calculate the 95% confidence intervals for τ_{eff} through substitution into Equation 20 and Equation 21.

3.5.3 Saturation Kinetics

The trends in Figure 18 allow us to investigate the molecular mechanism of surface linkage failure and how different deposition conditions can influence this process. The most unintuitive feature of the kinetics of the process is that as base concentration increases, the surface-supported population within a single deposition condition class *appears* to exhibit increasing molecular heterogeneity, despite identical deposition procedure, as indicated by a decreasing β value with increasing base concentration (Figure 18a). We have previously shown how a single static underlying distribution of molecular properties can exhibit different apparent distributions of shifting breadth under different experimental conditions by invoking a two-step mechanism.[20] Here, we consider a two-step process whereby base (B) reversibly diffuses from the bulk to a surface site (A) followed by irreversible cleavage of the surface linkage to reform an empty surface site (A’) and a free fluorophore (C), Equation 22. Further, we restrict the number of available surface sites to a maximum value, $[A]_T$, resulting in saturation kinetics,[159-160] Equation 23.

$$A+B \underset{k_{-1}}{\overset{k_1}{\rightleftharpoons}} AB \xrightarrow{k_2} A'+C$$

Equation 22

$$R_{obs} = \frac{k_2[A]_T[B]}{\frac{k_{-1}+k_2}{k_1}+[B]}$$

Equation 23

Replacement of singular values for any of the inputs in Equation 23 with distributions of values results in non-monoexponential behavior with β values shifting as base concentration changes, indicative of changing observed heterogeneity of rates, even far from saturation.[20] At low base concentrations and slow k_{-1}, the system approaches the low concentration limit:

$$R_{obs} = k_1[A]_T[B]$$

Equation 24

However, while the saturation model explains the trend of decreasing β with increasing base concentration, it fails to account for the differences observed *between* deposition conditions. To explain these differences, we sought to understand what interactions govern the behavior of **6** under base attack and how these interactions are affected by the different deposition protocols. To do so, simulations of the experimental Weibull distributions for each preparation procedure were performed on the basis of Equation 22, allowing us to derive estimates for the kinetic parameters in Equation 22. This process was accomplished by simulating a Weibull distribution of τ_{eff} values using Equation 23. We found it was necessary to create distributions of either k_1 or $[A]_T$ to qualitatively reproduce the observed trends. It was not necessary to create distributions in both parameters simultaneously, nor were distributions in other parameters necessary. It was found that the values of the parameters k_{-1} and k_2 did not have to be changed between deposition conditions to fit the experimental data, indicating that these parameters either have little effect on the kinetics of surface removal, or that they are the same between samples. To further examine their influence, each was changed by orders of magnitude while all other parameters remained the same to determine their individual effects. Example fits are shown for HS samples in Figure 19. Even when k_{-1} is changed by several orders of magnitude, little difference is seen between the simulated curves. This insensitivity indicates that k_{-1} has little to no influence on the kinetics of surface cleavage, consistent with the system operating in the regime of Equation 24, and that quantitative determination of k_{-1} is impossible from this data. Shifting k_2 by orders of magnitude causes a weak effect on the resultant fits. While little is changed in the low concentration fits (where Equation 24 will be a particularly good approximation), lowering k_2 has a significant impact on the high concentration simulated curves when it is changed by orders of magnitude. Consequently, while k_{-1} cannot be estimated from the data, an order of magnitude estimate of k_2 can be extracted. While it is possible that k_2 is changing for different deposition conditions, we are not able to resolve those changes and thus the observed diversity is believed to evolve from k_1 and $[A]_T$.

Simulations with distributions in $[A]_T$ are shown in Figure 22a-c. It was found that, regardless of which variable had the distribution, changing k_1 and $[A]_T$ had the greatest effect on the simulations. Multiple sets of non-unique simulation parameters resulted in qualitatively similar fits. However, the product $\langle k_1[A]_T \rangle$ (where the brackets denotes an average over the parameter distribution) is conserved across fits and decreases going from NHNS to HNS to HS. The dominant contribution of $k_1[A]_T$ and the lack of significant dependence on k_2 indicates that the system exists primarily in the low concentration limit, Equation 24.

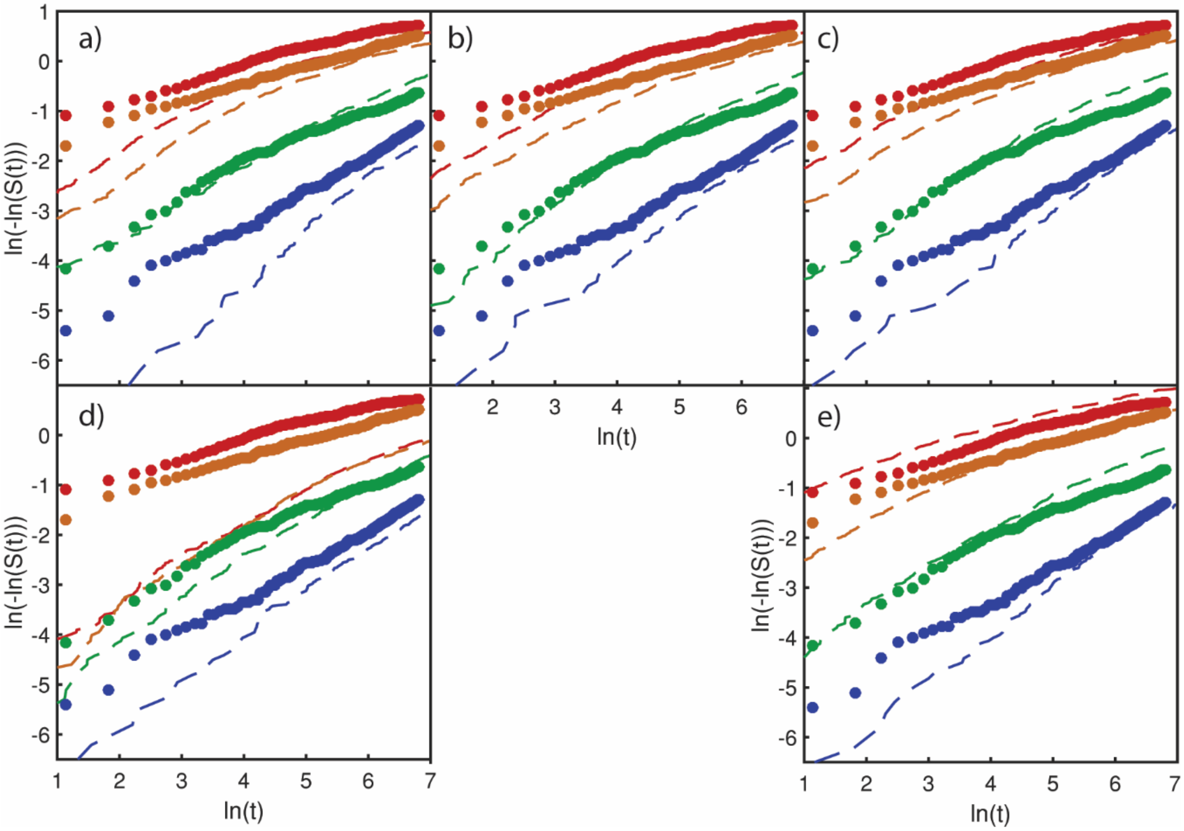

Figure 20: Simulations of HS data with k_{-1} and k_2 varied. For all, $[A]_T=3$, $k_1=1.5$ and $\beta=0.5$. For a-c) $k_2 = 0.008$. For d) and e) $k_{-1}=1x10^{-9}$. For a) $k_{-1}=1x10^{-15}$, b) $k_{-1}=1x10^{-9}$, and c) $k_{-1}=1x10^{-5}$. For d) $k_2=0.0008$ and for e) $k_2=0.08$. Note that b) utilizes the k_{-1} and k_2 values used in all simulations presented in the main discussion.

	$[A]_T$	k_1	k_1*[A]
NHNS	3	12	36
HNS	1.5	6	9
HS	1.5	3	4.5

Table 3: Best Simulation Parameters for Weibull Plots

For all, $[A]_T$ is a distribution with $\beta=0.5$, $k_2=0.008$, and k_{-1}=1E-9. Because the system largely operates in the regime describe by Equation 23, values determined for k_{-1} and k_2 have substantial uncertainty as discussed in the Supporting Information and are not used for mechanistic analysis.

3.5.4 Numerical Weibull Fitting

To more clearly show how the kinetic parameters control the behavior of **6**, the results of the simulations were used as the basis to numerically fit the Weibull curves. Global numerical fittings using a home-written MatLab fitting code were also performed on the data. Fits were performed under several initial conditions to determine whether the initial estimates had an effect on the fitting. It was found that the initial fitting parameters had a large effect on the resultant fits, indicating that the system is underdetermined. The values for β, k_2, and k_{-1} did not significantly vary from the starting conditions. While the individual values for k_1 and $[A]_T$ were quite variable, the product $k_1[A]_T$ is consistent for each deposition condition. Figure 20: Simulations with different k_1 and $[A]_T$ values. In Condition 1, k_1=3, $[A]_T$=3, and $k_1[A]_T$=9. In Condition 2, k_1=1, $[A]_T$=9, and $k_1[A]_T$=9. Data is from HNS samples. In both, k_2 = 0.008, k_{-1} = 1x10^{-9}, and β = 0.5 for the distribution of sites. Figure 20 shows simulations with different values for k_1 and $[A]_T$ but the same value for $k_1[A]_T$. Figure 22 shows the simulations that best reproduced the data, with parameters for the fits shown in Table 4. It was found that the fits

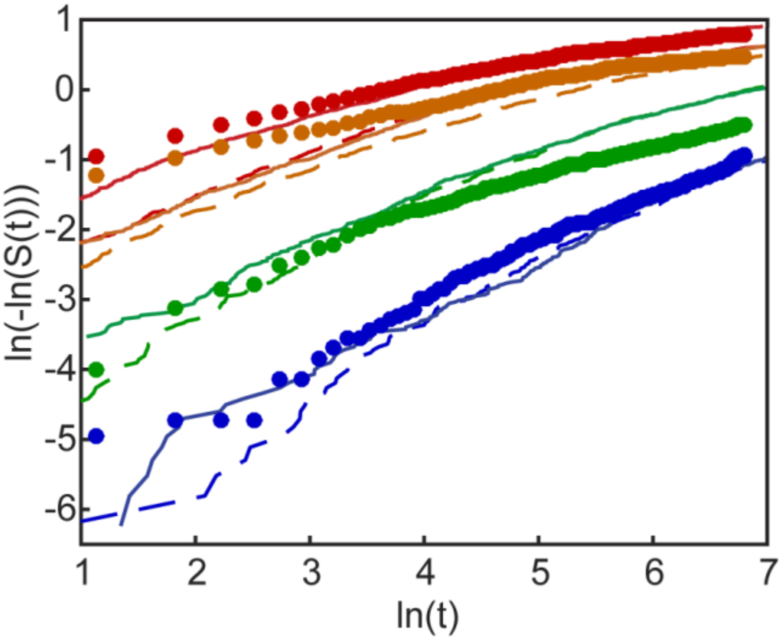

Figure 21: Simulations with different k_1 and $[A]_T$ values. In Condition 1, k_1=3, $[A]_T$=3, and $k_1[A]_T$=9. In Condition 2, k_1=1, $[A]_T$=9, and $k_1[A]_T$=9. Data is from HNS samples. In both, k_2 = 0.008, k_{-1} = 1x10^{-9}, and β = 0.5 for the distribution of sites.

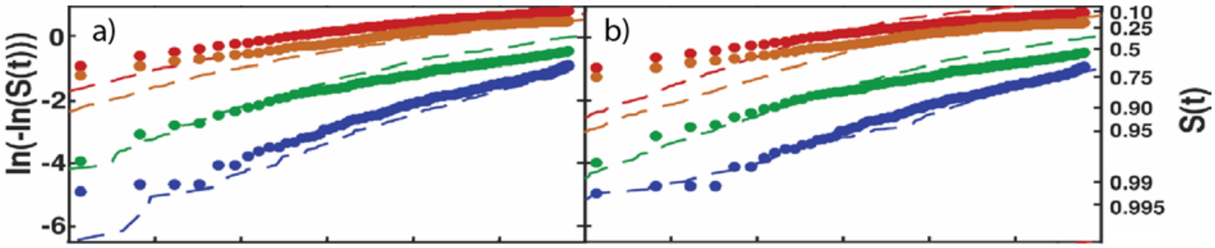

Figure 22: Simulations and fitting show similar results. a) Simulation with the following parameters: $k_1 = 6$, $[A]_T = 1.5$, $\beta = 0.5$, $k_2 = 0.008$ and $k_{-1} = 1\text{x}10^{-9}$. b) Fitting with the following parameters: $k_1 = 1.49$, $[A]_T = 6.06$, $\beta = 0.50$, $k_2 = 0.0082$ and $k_{-1} = 1.01\text{x}10^{-9}$. Neither fit is appreciably better than the other.

were not significantly better than the simulations by hand. Figure 21 shows an example of simulations giving very similar results.

3.6 Role of Deposition Conditions and Target of Base Attack

The results of the above simulations help to paint a molecular picture of the interaction of the base with the surface linkage and the silica surface. In summary, while heating and blocking layers increase the stability of the surface linkage (as reflected in rising values of τ_{eff}), they have little effect on the apparent diversity of rate constants (as reflected in the similar values of β between sample deposition conditions) which appears to increase as a function of base concentration (as reflected in decreasing β value with base concentration). The relative independence of β on deposition conditions is particularly surprising, suggesting that while the blocking layer may contribute to the apparent diversity in catalyst initiation rates, it does not contribute to the diversity for destruction of the surface linkage.[20]

We initially expected that the largest influence of the different deposition conditions would be observed in the value of k_2, the rate of irreversible reaction at the surface. However, the insensitivity of the simulation to k_2 suggests the system is effectively in the low concentration (diffusion-limited) regime where k_2 makes little contribution. In this limit the role of the different deposition conditions is suggested to exist elsewhere, either in k_1 or $[A]_T$, parameters that also control the β value. However, additional constraints can be added when considering a molecular mechanism. In particular, the insensitivity of β to deposition conditions suggests a splitting of the roles of the two parameters, with one parameter containing the critical distribution needed to observe a β value less than one independent of deposition conditions, with the other parameter containing a value dependent on deposition conditions that governs τ_{eff}. These constraints will help identify a plausible molecular mechanism of surface linkage disruption.

	[A]	k_1	β	k_2	k_{-1}	k_1*[A]
NHNS	18.27	0.80	0.40	0.0171	1.19E-9	14.6
HNS	1.5	6	0.5	0.008	1E-9	9
HS	1.5	3	0.5	0.008	1E-9	4.5

Table 4: Fitting Parameters in Figure 22

The addition of the TOS layer on the surface protects the surface linkage of **6** by creating a physical barrier between the base and the glass surface, thus making it more difficult for the base to reach the silyl linkage.[153] When TOS is deposited in samples at a high concentration, the network that is created provides a steric barrier to attack by the bulky isopropoxide species as well as an electrostatic barrier, as the highly polar anion cannot easily penetrate the non-polar aliphatic layer. Thus, the addition of TOS provides multiple barriers against base reaching the silyl linker, resulting in a low value of k_1. Because the blocking layer can be expected to significantly affect mass transport between the bulk solution and the surface, we will focus on k_1 as the dominant term capturing the role of the different deposition protocols.

The inclusion of a heating step in the HNS procedure is also expected to influence the value of k_1 but in a more subtle manner. By heating the HNS samples, a covalent bond is formed between the silica surface and **6**, whereas in the unheated NHNS samples, the physisorbed **6** is likely held at the surface by hydrogen bonding interactions, Figure 13a middle. When an isopropoxide molecule, a hydrogen bond acceptor, approaches the surface proximal to post-heated covalently bound **6**, no hydrogen bond donors exist at the surface near bound **6**, except in the rare instance of **6** being attached to a geminal silanol.[161] However, physisorbed **6**, which has yet to condense and eliminate H_2O, contains at least one hydrogen bond donor directly proximal to the surface linkage. These donors are able to interact favorably with the isopropoxide, improving the probability of successful surface encounters, thus increasing k_1 in NHNS samples as compared to HNS samples. The fact that no detectable hydrolysis occurs in solution (see Supporting Information) suggests that the silyl ether linkages remain intact if they are not forming strong interactions with the surface, a precursor interaction to covalent bond formation. The chemically distinct surface linkages in the HNS and NHNS samples are further indicated by differences in the required surface deposition procedure. Specifically, to prepare HNS and NHNS samples with roughly the same fluorophore surface coverage, the deposition solution for the NHNS samples must be five times more concentrated than the HNS samples, otherwise, washing steps remove the majority of the physisorbed molecules.[154] Consequently, trends in k_1 are well connected to differences in microenvironment stemming from the deposition conditions.

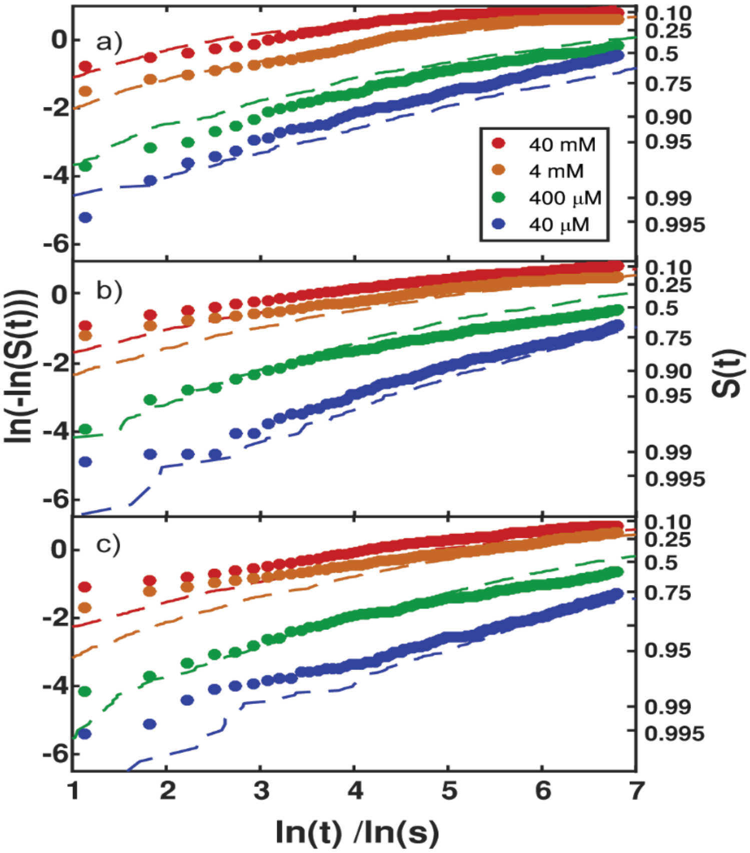

Figure 23: Numerical fits (dashed lines) of experimental data (closed circles) for Weibull fits using Equation 23 for a) NHNS, b) HNS, c) HS samples.

The model must also capture diversity in values for $[A]_T$, the maximum “local concentration” of base molecules attached to the surface capable of reacting with and irreversibly cleaving the surface support. Critically, the model requires decoupling this value from the surface treatment. While comparable values of $[A]_T$ are expected for the NHNS and HNS treatments, it was expected that the density of the blocking layer would also influence $[A]_T$, particularly since $[A]_T$ dominated the distribution in our previous work on catalyst initiation at surfaces.[20] However, the chemical environment *within* the aliphatic blocking layer (near the catalyst) may be quite different from the environment at the surface. The number of hydroxyl groups on a silica surface varies depending on preparation conditions, but on average, there are 4-5 hydroxyl functionalized groups per nm^2 on a silica surface.[162-163] This density implies that the distance between bound molecules at the surface is large compared to the size of the base anion. While the TOS layer makes it more difficult for the base to get to the surface (affecting k_1), once at the surface, the microenvironment of the surface of the HS samples may not appear to be greatly different from the HNS and NHNS samples. Thus the apparent chemical heterogeneity would be only weakly dependent on surface treatment, as observed. The dominant source of chemical heterogeneity is then the natural diversity of surface sites on silica,[164-166] with different topography and chemical functionality in the neighborhood of each surface linkage determining the maximum local concentration, $[A]_T$.

In lieu of the model proposed here, we might consider models wherein $[A]_T$ changes and k_1 stays the same, or where both $[A]_T$ and k_1 are changing. If k_1 remained constant, this would imply that the surface was equally accessible by base in every deposition condition and that the change in kinetics between deposition conditions is solely caused by changes in $[A]_T$. To invoke this model, one would have to suggest that the barrier created by addition of TOS has no effect on the approach of the base and we reject this proposal as unphysical because the TOS creates both a steric and electrostatic barrier between the substrate and bulk solution. On the other hand, varying $[A]_T$ is not supported by the simulations. For all deposition conditions, a distribution of $[A]_T$ was necessary to fit the data. In every case, a very similar width of the distribution was needed, reflected by the β value of the distributions. If $[A]_T$ were changing, it is likely that the width of the distributions of $[A]_T$ would also change. Because this is not seen, we believe that the proposed mechanism, wherein k_1 changes with deposition condition but $[A]_T$ stays the same, is the most plausible model to describe the observed phenomena. While we cannot discount the possibility that more complex mechanisms are operational here, our proposed two step model is the simplest model that captures the observed behavior, and is thus preferred in the absence of additional experimental evidence.

In summary, the molecular picture described above provides a qualitative means of understanding the behavior in Figure 18. In our model, the differences in τ_{eff} between deposition conditions is caused not by different rates of irreversible chemical reaction, k_2, but by the decreasing value of the product $k_1[A]_T$ from NHNS to HNS to HS samples, as suggested by fits to Figure 22. Further analysis suggests k_1 varies significantly between deposition methods. The deposition methods also do not affect the immediate chemical microenvironment of the surface linkage that controls $[A]_T$, leading to diversity originating with natural surface heterogeneity of silica.

3.7 Conclusions

During our single-molecule investigation of surface-support degradation at silica surfaces, we found that a kinetic model captures the observed trends where the benefit of thermal annealing and blocking layers derives not from an increase in the stability of the surface linkage, but from a decrease in rate at which base molecules approach the surface before irreversible attack at the silyl ether linkage. We also showed that the observed heterogeneity in kinetics is likely caused by the innate structural diversity of the silica surface. These results suggest that efforts to make silyl-ether constructs at silica interfaces more stable in basic environments should focus on further reducing mass transport of bases through the functional layer to the silica surface, an important recommendation for in-flow reactors with surface-supported molecular catalysts. Further, efforts to reduce the chemical diversity of interacting sites at the silica surface, in chromatographic separations for example, will be limited by silica surface site polydispersity unless the dominant interaction between the mobile and stationary phase occurs at the interface between the functional layer and the mobile phase, effectively insulating the silica surface from interaction with the mobile phase. Finally, these results show another example of how single-molecule techniques can be a powerful tool to investigate chemical dynamics at surfaces.

3.8 Acknowledgments

This work was supported by the National Science Foundation under Grant No. (CHE-1254936). We would like to thank Michael Vermeuel for assistance with data acquisition, Sunil Upadhyay for assistance with synthesis and Angela Marquard for helpful conversation

4. Production of Toluene-in-Water Droplets to Probe Single-Molecule Catalyst Kinetics.

This chapter is unpublished.

Katherine Lupo investigated droplet formation in vortexed emulsions, PDMS microfluidics, and glass microfluidics and performed DCDHF reaction optimization in collaboration with Andrew Cavell. PDMS microfluidic work was done in collaboration with Dr. Job Grant. Andrew Cavell and Veronica Krasecki did additional work with the glass microfluidic.

4.1 Abstract

The Suzuki-Miyaura coupling reaction is a well-studied C-C coupling reaction, making it a good candidate for single-molecule studies. To immobilize single molecules of a Pd catalyst without the need for covalent attachment, toluene-in-water droplets were generated. Microscale droplets have been used for single-molecule reactions, but generally water-in-oil droplets have been used. The generation of toluene-in-oil droplets was studied, revealing the difficulty of finding surfactant and generation conditions to produce small and stable droplets. Concurrently, the conditions of a C-C coupling reaction were modified to make the reaction feasible on the single-molecule level. Work continues towards reaching single-catalyst encapsulation in nanoscale toluene droplets.

4.2 Introduction

Low-volume droplets formed in microfluidic devices have increasingly become useful tools for vetting reactions quickly. Droplets offer several advantages: they act as “microreactors”[167-168] with low volumes that allow for selective mixing[169-170] and high-throughput screening,[171] particularly in single cell analysis.[172] Droplets are also useful tools in single-molecule detection. Applications include single-molecule PCR[173-174] and investigation of enzyme kinetics.[175-176] In fact, an early example of single-molecule measurements was on the enzyme β-D-galactosidase, where single enzyme molecules in water droplets performed a fluorogenic reaction.[175] A distribution of reaction rates from single molecules of β-D-galactosidase was found, proving that heterogeneity existed in the system. These results provided a precedence for future work on single-molecule catalyst kinetics, including the present work.

Here, we describe a way to use droplets to immobilize non-biological molecular catalysts for single-molecule study. In previous studies, we have immobilized fluorescent probes to glass surfaces to allow for imaging at a longer time scale than permitted by diffusion.[20, 177-178]

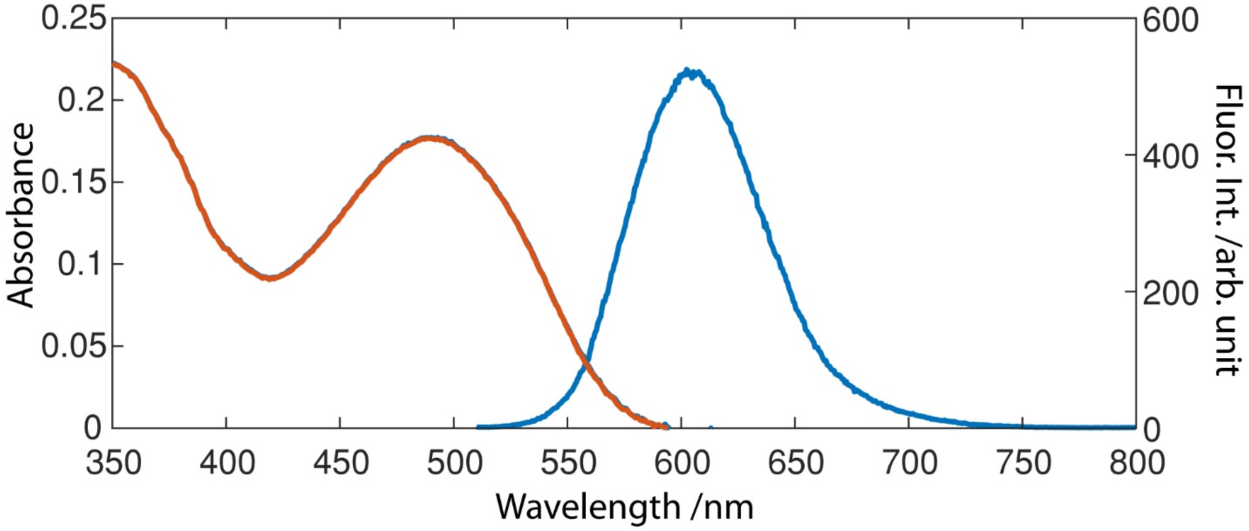

Figure 24: Bulk absorbance (red line) and fluorescence (blue line) of DCDHF in toluene. The fluorescence was excited at 500 nm.

Confinement in droplets provides the advantage of surface immobilization, i.e. the ability to image for long time scales, with the advantage of free diffusion, i.e. that movement and function are not constrained. Using droplets to confine catalysts instead of surface immobilization is also advantageous in that the structure of the catalyst does not have to be altered to have a surface support, which introduces synthetic challenges and could possibly alter the function of the catalyst. In this experiment, the goal is to have droplets with one or fewer catalyst molecules in droplets, with synthetically relevant reactant concentrations. The catalyst and reactants are nonfluorescent, but upon coupling, the product becomes fluorescent, ie, a fluorogenic reaction. Because only one catalyst would exist per droplet, the generation of fluorescence is directly caused by a single catalyst. Thus, kinetic information for the direct action of single catalysts could be derived.

The Suzuki-Miyaura Reaction is a C-C coupling reaction used to couple aryl boronic acids and aryl halides into biaryl compounds.[179] Here, a fluorogenic reaction (Figure 24) is used to investigate the activity of single catalyst molecules of palladium tetrakis(triphenylphosphine) ($Pd(PPh_3)_4$). Mechanistic studies of $Pd(PPh_3)_4$ as a catalyst for Suzuki-Miyaura couplings exist, providing a good basis for single-molecule studies.[180] Information on the kinetics of single catalyst molecules provides information lost in bulk reactions. Ultimately, understanding the heterogeneity of the system will act as a complement to bulk studies, potentially elucidating why some catalyst systems perform better than others.

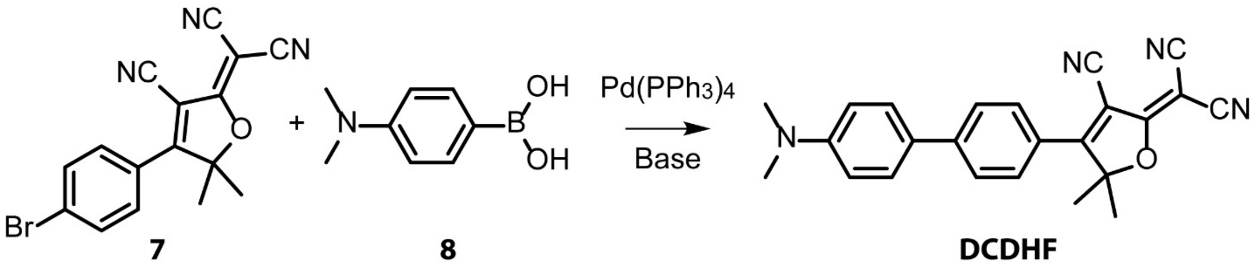

Figure 25: The DCDHF Reaction.

The reaction in Figure 24, herein called the DCDHF reaction, involves the coupling of 2-dicyanomethylen-3-cyano-5,5-dimethyl-4-(4-bromophenyl)-2,5-dihydrofuran, **7**, and 4-(dimethylamino)phenylboronic, **8**, to form coupled DCDHF, where DCDHF is short for 2-dicyanomethylene-3-cyano-2,5-dihydrofuran. We will use the term “DCDHF” to refer to the coupled DCDHF fluorophore unless otherwise noted. DCDHF fluorophores are a class of push-pull fluorophores composed of a donor amine group and an acceptor DCDHF group. The donor and acceptor groups are separated by a pi-conjugated core.[181] Many fluorophores in the DCDHF family have been synthesized, but the one used in this study features a biaryl core which results in absorption and emission properties that are well suited for our system. Bulk absorption and emission curves are shown in Figure 23. At the wavelength of maximum absorption, the molar absorptivity of DCDHF is 31,000 $M^{-1}cm^{-1}$ and the quantum yield is 0.82 in toluene.[181] Notably, there is significant absorption at 532 nm, the wavelength used for microscopy in this study. The use of DCDHF, however, constrains which solvents can be used. A non-radiative pathway through a twisted intramolecular charge-transfer (TICT) state has been implicated as a source of fluorescence quenching and polar solvents stabilize the TICT state well. It has been shown for some DCDHF fluorophores that the use of the nonpolar solvent toluene results in an order of magnitude higher quantum yield compared to the quantum yields in polar solvents such as acetone or ethanol.[83] Thus, toluene was selected as the solvent in this study.

4.2.1 Challenges and Opportunities

Much work has been done in producing water droplets suspended in oil carrier phases. Robust surfactant-oil-water systems have been developed to produce small and stable droplets.[182] However, oil-in-water droplets are less well studied and examples of oil-in-water droplets generally employ high viscosity oils.[183-185] Because the target reaction is carried out in toluene, it is necessary to make toluene-in-oil droplets. Examples of toluene-in-water droplets exist, but are usually in the size range of tens to hundreds of micrometers.[186, 187] As discussed below, nanoscale, not microscale, droplets are ideal for this study. Thus, the challenge of developing a method for producing small, uniform, and stable toluene-in-water droplets arises. By modifying surfactants and formation modes, we have begun to approach the parameters necessary for single-molecule studies.

Another consideration is the desire to run reactions at the single-catalyst level. Lower catalyst concentrations may decrease the overall yield of product, so conditions must be found that balance the speed of the reaction and the concentration of catalyst. The catalyst concentration and droplet size must be balanced such that the local concentration of catalyst and reactant in each droplet is high enough that the reaction proceeds at a reasonable time scale, on the order of hours, while still having single catalyst molecules in droplets. At various droplet sizes, assuming spherical droplets, the necessary concentration of catalyst needed to have roughly one catalyst per droplet can be calculated. Various droplet sizes and the corresponding catalyst concentrations are presented below in Table 5. Clearly, smaller droplets allow for higher catalyst concentrations, which are beneficial in terms of reaction speed. Additionally, approaching higher catalyst concentrations leads to more synthetically relevant reaction conditions. If a typical coupling reaction uses 10% catalyst, to reach synthetically relevant conditions, the catalyst concentration would have to be on the order of hundreds of micromolar. Smaller droplets are also advantageous for microscopy in that it should increase the signal to noise ratio of the fluorescence signal by decreasing background fluorescence.

Diameter (μm)	20	10	1	0.5	0.1
Volume (μm^3)	4200	520	0.52	0.063	$5.2x10^{-4}$
[$Pd(PPh_3)_4$]	396 fM	3.2 pM	3.2 nM	25.5 nM	3.2 μM

Table 5: Various sizes of droplets and the corresponding concentrations of catalyst that would be necessary to average one catalyst molecule per droplet, assuming spherical droplets. Every decrease in diameter by an order of magnitude corresponds to a 10^3 increase in catalyst concentration.

The work presented herein shows attempts at balancing both challenges- producing small, uniform, and stable toluene-in-water droplets and controlling the rate of reaction of the DCDHF reaction. Droplets were produced using different production methods and various surfactants. While ideal conditions have not been reached, improvements have been made. Similarly, development for the DCDHF reaction has occurred, but ideal conditions have not been reached. Despite the unfinished nature of this project, potential exists for the continuation of this study.

4.3 Experimental

4.3.1 DCDHF Reaction

The DCDHF reaction scheme is shown in Figure 24. In short, **7** and **8** couple to form the DCDHF fluorophore. Compound **7** was synthesized by graduate student Daniel Hinton and former post-doctoral researcher Sunil Upadhyay. Compound **8** was received from Sigma Aldrich and purified as discussed below. Palladium tetrakis(triphenylphosphine) ($Pd(PPh_3)_4$) was used as catalyst. In a typical experiment for setting up emulsions, 4 mM each of **7**and **8** were used and the $Pd(PPh_3)_4$

was varied, with toluene as the solvent. Generally, an additional base was not used, as discussed below. Reactions were generally performed at room temperature.

To makes compounds **7** and **8** suitable for single-molecule studies, ie remove fluorescent impurities, additional purification steps were taken. To purify **7**, it was recrystallized twice in 30% methanol in dichloromethane, then washed with pentane three times, decanting off the pentane between rinses. To purify **8**, it was washed with pentane 5 times.

4.3.2 Droplet Formation

Many different modes of droplet generation were attempted. Because of the difficulty associated with making toluene-in-water droplets, no one mode of droplet formation has proven to be ideal, thus far. The various methods for preparing droplets are discussed below.

4.3.2.1 Vortexed Emulsions

Perhaps the simplest mode of droplet formation is through vortexed emulsions. In a typical experiment, 150 μL of the disperse phase, generally a toluene solution, was added to 750 μL of an aqueous phase in a microcentrifuge tube. The mixture was then vortexed (Scientific Industries Vortex Genie 2) at the highest speed for roughly a minute. The resultant emulsion (Figure 25a) was left to settle for a few minutes before use and imaging. Generally, droplets formed through vortexing were sized in the 10’s of micrometers and showed high variability in their size.

4.3.2.2 PDMS and Glass Microfluidic Devices

In collaboration with the Romero group, PDMS microfluidic devices were used to produce droplets. The pattern of the microfluidic device is seen in Figure 25b. The continuous phase, generally an aqueous surfactant solution, and the disperse phase, generally toluene, were pumped through the device using two New Era Model 501 Syringe Pumps. The syringe pumps were controlled with a custom written Python code (Romero, Philip. Syringe-pump-controller. GitHub Repository. https://github.com/RomeroLab/syringe-pump-controller). To prevent degradation of plastic syringes from toluene, gastight glass syringes (Hamilton Syringes) were used. Droplets were formed in a jetting regime, discussed below. Droplets are shown in Figure 27and generally had a size of about 20 micrometers in diameter.

PDMS swells in toluene,[188] causing toluene to stick to the device's sidewalls. To attempt to combat the sticking, polyionic polymer layers were deposited in the microfluidic device.[189] To do this, solutions of poly(allylamine hydrochloride) (PAH, MW=50,000, Sigma Aldrich) and poly(sodium 4-styrenesulfonate) (PSS, MW=70,000, Sigma Aldrich) were prepared. Individual devices were coated with layers of 0.1% w/v PAH and PAA in 0.3 M NaCl. Between each polyelectrolyte, 0.3 M NaCl was put through the device. A gentle vacuum was attached to all ports of an individual device except for one. Small amounts of each solution, about 5 μL aliquots, were pipetted into the port not attached to the vacuum. Between each aliquot, the solution was allowed to fully drain out of the device. For each device, 8 layers total were deposited.

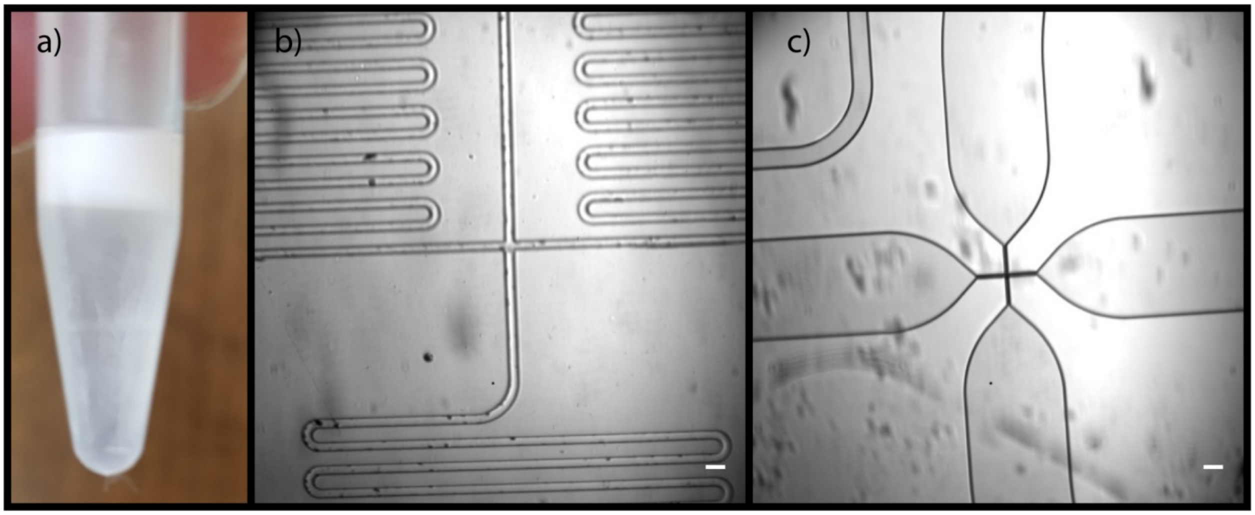

Figure 26: Various tools for droplet formation. a) A vortexed emulsion. b) The PDMS microfluidic device and c) the glass microfluidic device. Scale bars are 100 μm.

To circumvent the issues of sticking in PDMS microfluidic devices, a 14 μm Small Droplet Chip glass microfluidic device was obtained from Dolomite Microfluidics. A picture of the device is shown in Figure 25c. The glass microfluidic has a naturally hydrophilic surface, which prevents interactions between the device's walls and toluene. As before, the aqueous phase and the disperse oil phase were pumped through the device using syringe pumps and glass airtight syringes. The program SyringePumpProV1 (SyringePumpPro, Gawler, South Australia, Version 1.6.4.7) was used to control the syringe pumps. Flows were adjusted as necessary to reach regimes where droplets formed; flows of roughly 100 μL/min were used for the continuous aqueous phase and flows of about 10-20 μL/min were used for the disperse toluene phase.

Alternatively, the glass microfluidic device was used in a shearing mode.[190] Instead of having two streams of continuous phase coming in from the side ports to pinch off the single toluene stream coming up the center, the opposite configuration was used. Toluene was pumped through the two side ports while the aqueous phase was pumped through the central channel. This configuration is closer in functionality to a T-junction.

4.3.3 Droplet Immobilization in Gel

Poloxamers have become a useful tool for droplet immobilization. Poloxamers are a type of polymer which are liquid at cold temperatures and become gel-like at elevated temperatures.[191] A poloxamer known by the trade name Pluronic F-127 (Sigma Aldrich) was used. A roughly 30% solution of Pluronic F-127 in water is liquid-like when refrigerated and becomes gel-like at room temperature.[191-192] To use the polymer for sample immobilization, about 100 μL of 30% Pluronic F-127 is pipetted onto a coverslip while still cold. The coverslip and the vial of Pluronic F-127 were placed on a cold aluminum block. Then, while the Pluronic F-127 was still liquid, a small amount of an emulsion, roughly 5 μL, was pipetted into the Pluronic F-127. Then, a coverslip was placed on top of the sample.

4.3.4 Microscopy

4.3.4.1 Brightfield Microscopy

Brightfield microscopy was used to observe droplet generation in the glass microfluidic device. Overhead illumination on a Nikon Eclipse Ti inverted microscope was collected through a 10x air objective and focused on an Andor EMCCD iXon camera with a 512 x 512 pixel detector.

4.3.4.2 Fluorescence Microscopy

Samples were imaged on a Nikon Eclipse Ti inverted microscope using a 532 nm Coherent Sapphire fiber-coupled diode laser. The excitation laser was guided through a Nikon Plan Fluor 40x air objective. The fluorescent signal was collected through the same objective and passed through a Semrock 532 nm RazorEdge Dichroic mirror and a Semrock EdgeBasic 532 nm longpass filter. The fluorescent signal was then focused onto an Andor EMCCD iXon camera with a 512 x 512 pixel detector. The resultant illuminated area was about 100 cm^2 and the laser intensity used varied depending on the experiment, but ranged from 10-100 W/cm^2.

4.3.4.3 Typical Fluorescence Experiment

The overall goal, as stated before, is to observe the generation of DCDHF by single catalyst molecules encapsulated in single droplets. To approach this limit, we initially started with higher catalyst concentrations and stepped down the catalyst concentration gradually. In a typical experiment, an emulsion was made through vortexing a DCDHF reaction mixture containing **7**, **8**, and $Pd(PPh_3)_4$ in toluene as the disperse phase and an aqueous surfactant solution, generally CA-720, as the continuous phase. The emulsion, after settling for a few minutes, was immobilized in the Pluronic F-127 as described above. Droplets were then imaged over several hours, with images of the same droplets taken every 15-30 minutes. Image analysis was then done on the droplets to see whether fluorescence, from the formation of DCDHF, increased over time.

4.4 Results

4.4.1 Droplet Formation

The success of droplet formation was quite variable depending on conditions. In the course of preparing droplets, we have found that the number of parameters that can be varied leads to difficulty in optimizing conditions. The results from the various modes of droplet generation are discussed below.

4.4.1.1 Role of Surfactant

Several surfactant types were used to form droplets. Surfactants were dissolved in the aqueous phase. Surfactant choice is important because factors such as droplet size and stability can depend on the surfactant. Importantly, the surfactant must not interfere with the desired chemistry. To determine the suitability of various surfactants, several emulsions with various surfactants were prepared, and the emulsions were monitored for stability over the course of several days. A comparison of the emulsions prepared with various surfactant solutions and a DCDHF reaction mixture as the disperse phase are shown in Figure 26. Interestingly, all surfactants used led to stable emulsions over the course of several days. However, several surfactants showed incompatibility with the DCDHF reaction conditions. As is visible in Figure 26, the emulsion prepared with sodium dodecyl sulfate appeared purple. While we did not investigate what caused

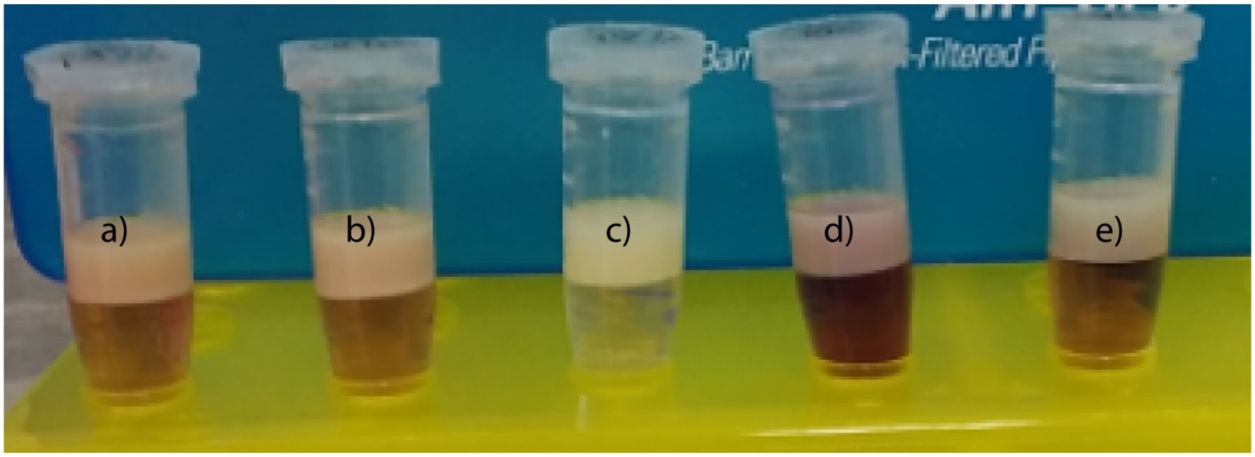

Figure 27: Vortexed emulsions with 4 mM **7** and **8,** 1 µM Pd(PPh_3)$_4$ and a) 1% v/v CA-720, b) 1% v/v CO-720, c) 1% v/v Tween 20, d) 4% w/w SDS, and e) 0.1% w/w MTAB.

this color change, it is clear that SDS should not be used for further studies. Instead, we identified CA-720, CO-720, and Tween 20 as the most promising surfactants for further study.

While not much difference was seen in emulsions stability, surfactants may play a bigger role as droplet size is reduced. Structurally, we predict that CA-720, CO-720, and Tween 20 will be the most stabilizing surfactants. In a toluene-in-water droplet, the nonpolar tail of the surfactant will lie within the toluene sphere, whereas the hydrophilic head group will lie outside of the toluene droplet, in the aqueous phase. Sterically, it is likely advantageous to have bulky polar head groups compared to the nonpolar tails. It has been shown that in water-in-oil droplets, where the nonpolar tail is on the outside of the droplet, having smaller alkyl chain lengths increases the radius of the droplet.[193] It likely follows that in the opposite configuration, with the polar head groups facing out, their size will affect the curvature of the droplet. When packed together, surfactants with bulkier polar groups may be more susceptible to curving, making it easier to form spherical droplets. It has been shown that the size of spherical micelles depends on the length and volume of the surfactant tail as well as the surface area of the molecule.[194] With tail sizes being roughly equal, the size then becomes dependent on the head group of the surfactant. However, the area of the head group is based on energetic considerations, not simply on geometric considerations.[195]

Thus, it is not easy to determine if the predicted effect of head group size will actually translate to a change in droplet sizing. Further studies are needed to systematically determine which surfactant produces the most stable and small droplets.

4.4.1.2 Droplets Formed Through Vortexing

Forming emulsions through vortexing was the main method of droplet formation used. The vortexing method has several desirable properties. Vortexed emulsions are quick and easy to produce, taking just minutes to set up and produce. Thus, vortexed emulsions are an ideal solution for producing droplets for time sensitive tests and for running initial experiments quickly. However, vortexed droplets have multiple disadvantages. For one, there is little control over the size of the droplets produced through vortexing. Although we have not studied these affects systematically, vortexing speed and time affect the sizes of droplets produced, making reproducibility difficult. Similarly, vortexing produces droplets in a wide distribution of sizes, with the median sizes tending to still be too large for the single-molecule studies planned. For the single-molecule studies, it is ideal to have droplets that are small and as close to monodisperse as possible, as discussed above. However, much of our initial data is from vortexed emulsions because of their ease of use. While they cannot be used for single-molecule studies, they have been an important tool as we go ever closer towards single-molecule studies.

4.4.1.3 Droplets Formed In PDMS Devices

Droplets that were formed in PDMS devices tended to be more monodisperse than droplets formed through emulsions. However, forming droplets in PDMS devices has several disadvantages. PDMS swells in toluene,[188] leading to toluene sticking to the sidewall of the device. The sticking, in turn, leads to difficulty in reaching a pinching regime in the microfluidic. Indeed, the only way we were able to produce droplets was in a jetting regime, where high pumping pressures led to a long stream of toluene going past the junction point with droplets coming off the end of the solvent jet. Droplets are shown in Figure 27 and generally had a size of about 20 micrometers in diameter. While the diameter of these droplets begins to approach the sizes needed for our single-molecule studies, production of the droplets takes a long time and lacks reproducibility. Getting to a jetting regime is a long process, as simply returning to previously successful settings generally does not result in droplet formation. Instead, it is necessary to gradually ramp up the pumping pressure to return to a regime where droplets are formed. Thus, it can take on the order of hours to begin producing droplets, which is the same timescale that the reaction would take place on. Ideally, to maximize the amount of data procurable, droplets would need to be produced in minutes, not hours.

To combat the problems caused by toluene sticking to the PDMS sidewalls, we attempted to put down a hydrophilic blocking layer onto the PDMS devices. Although the layer deposition was attempted several times, problems with deposition were persistent. When the vacuum on the device was not sufficient it would take several minutes to draw even small amounts of the solutions through. Increasing the vacuum through the device resulted in the inner walls collapsing, again

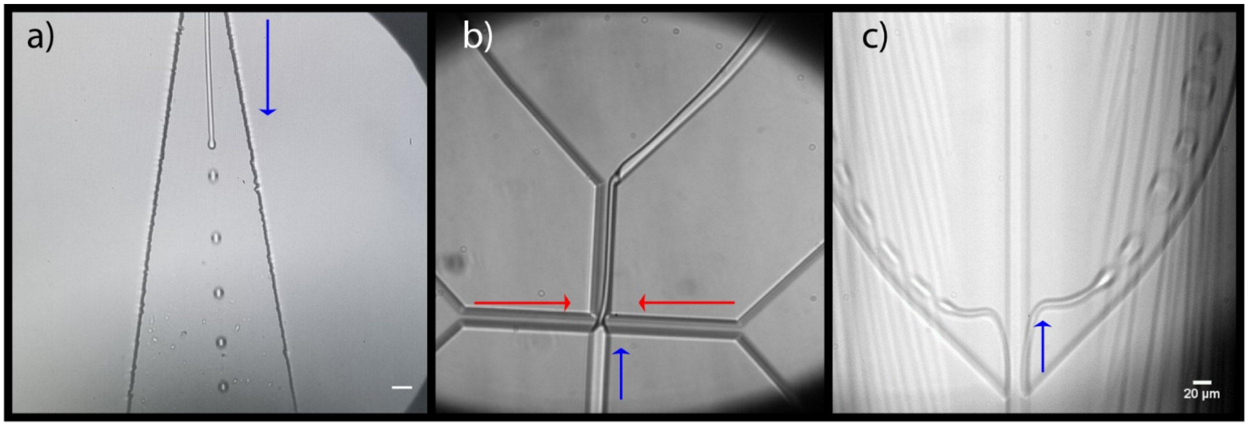

Figure 28: Toluene streams in microfluidics. a) Droplets streaming out of a PDMS device. Scale bar is 100 µm and is approximate. b) Toluene streaming out of the glass microfluidic in the cross-junction mode and c) droplets being formed from the T-junction mode. Scale bar for c) is 20 µm and is for both b) and c). Red arrows show the flow of water and blue arrows show the flow of toluene.

leading to difficulty in drawing solutions through them. When layers were successfully deposited, the devices would often have foreign matter in them from the solutions which would clog the devices. Furthermore, the deposited layers did not appear to have a beneficial effect on toluene sticking to the PDMS walls. Thus, the layer deposition was not used for further studies.

4.4.1.4 Droplets Formed in the Glass Microfluidic Device

So far, the glass microfluidic device has proven to be a promising method for producing droplets. The glass microfluidic has a naturally hydrophilic surface, which prevents interactions between the device’s walls and toluene. As such, we were hopeful that toluene would more easily form droplets in the device. Attempts were made to reach the pinching regime. At best, thin streams of the toluene phase were reached, but they never collapsed into droplets, as seen in Figure 27b. To try to reach a regime where droplets were produced, flows of around 100 μL/min were set as the initial rates for each phase. Once the flow reached a steady state, the rate for the toluene phase was decreased incrementally, leading to reductions in the thickness of the toluene stream. However, once a rate in the tens of microliters per minute was reached for the toluene, going below a certain rate caused the aqueous phase to overpower the toluene phase, causing the toluene to travel backwards in its channel. Whenever this happened, toluene would have to be flowed through the device at a high rate again; the toluene pressure could not simply be increased to the last acceptable rate to return to a regime where toluene was moving forward in its channel. Reaching an intermediate between the regime where the toluene was streaming but not breaking into droplets and regime where toluene was flowing backwards was difficult and we have only managed to reach a regime with droplets forming a few times and not for very long. The alternate mode of droplet formation in the glass microfluidic device wherein the ports used for continuous and disperse phases are switched has proven more successful. An example of droplets being formed in this mode is shown in Figure 27c.

Many have investigated the mechanism for droplet breakup in both cross-junction[196-198] and T-junction[199-201] devices. However, our mode of droplet formation has been markedly different from those presented in the literature. In the literature, much of what is described are mechanisms wherein droplets are forming at the junction between the continuous and disperse phases. We have not observed this mode of droplet formation. On the contrary, in both the cross- and T-junction configurations, the toluene stream extends past the junction point and droplets are formed from the end of the stream. This mechanism for breakup is referred to as the jetting regime. In contrast to other regimes, the jetting regime does not depend on the pressure at the junction,[202] instead depending on shearing forces caused by differences in the flow rate of each phase.[190] Because droplets are formed after the junction in the jetting regime, there is no difference in the mechanism of droplets formed in the T-junction or the cross-junction configuration. Thus, the relative ease of using the device in the T-junction configuration must be caused by ease of forming a jet. In the cross-junction, the continuous aqueous phase is coming in from two ports which, in a dripping regime, would cause toluene to pinch off into droplets. However, in the jetting regime, the dual aqueous streams simply make it difficult to produce a jet of toluene. When the toluene flow is set too low or the water flow too high, the pressure of the dual water ports overwhelms the toluene pressure, making it flow backwards. Conversely, in the T-junction configuration, with only one water port and two toluene ports, the toluene flow can be set lower without causing backflow, ultimately allowing for the creation of a thinner stream that can break up into droplets.

4.4.2 Droplet Immobilization

A benefit of the Pluronic F-127 is that the thickness of the sample is somewhat tuneable. To make the sample very thin, the top coverslip can be placed on the sample while it is still on the cold aluminum block. To make a thicker sample, the top coverslip can be placed after the sample is taken off the cold aluminum block, allowing the Pluronic F-127 to gel slightly before the coverslip is put on. Because the emulsion floats in the Pluronic F-127, after the sample has gelled, the sample can be inverted and imaged from the top coverslip. This results in the droplets being near to the bottom of the coverslip surface with no chance of them floating to the top, due to the gel polymer. Conveniently, putting the emulsion in the Pluronic F-127 helps to disperse the droplets, so while there are often still out of focus droplets in the polymer, it is easier to find regions with fewer out of focus droplets. Additionally, when the droplets are in the gelled Pluronic F-127, it is very rare for them to move. As a result, it is possible to observe the same droplets over a long period of time, up to a day (Figure 30c and d shows a droplet over 1 hour with no deformation). This is useful for spectroscopic studies where it is necessary to view the same droplets over the course of several hours.

4.4.3 DCDHF Reaction

Before investigations of the DCDHF reaction in droplets could be attempted, the reaction had to be characterized at the bulk level. The reaction must be first be optimized at the bulk level. To that end, several parameters were investigated in the bulk, as described below.

4.4.3.1 Role of Base

Suzuki couplings require a base to increase the rate of the transmetallation step in the catalytic cycle. It has been proposed that the base interacts with the boronate species to form a more reactive species that can react with the Pd center.[203] At the bulk level, initial studies by Sunil Upadhyay showed that potassium fluoride (KF) and 18-C-6 worked well as the base in toluene, with the 18-C-6 helping to solubilize the otherwise insoluble KF. Further investigations were performed in collaboration with graduate student Andrew Cavell. After many attempts to recreate this result, it was found that KF actually appeared to decrease the rate and overall yield of reaction. When the base was omitted, the reaction proceeded better than with any base, as can be seen in Figure 28. In Figure 28, an orange color indicates formation of DCDHF. Further experiments suggest that 18-C-6 appeared to be decreasing the yield of the reaction, Figure 28g-h. However, because the reaction proceeds without an added base, further investigations were eschewed in favor of working with the reaction without an additional base.

4.4.3.2 Role of Concentration of Reactants

Because decreasing catalyst concentration decreases the rate of the reaction, the highest possible reactant concentrations were used. It has been determined that the saturation concentration of **7** is about 4 mM, so 4 mM each of **7** and **8** were generally used in all reactions.

4.4.3.3 Lowering Catalyst Concentration

To move towards the single-molecule studies, the concentration of $Pd(PPh_3)_4$ was systematically lowered in bulk reactions. At 100 μM of $Pd(PPh_3)_4$ and 4 mM of each reactant, the

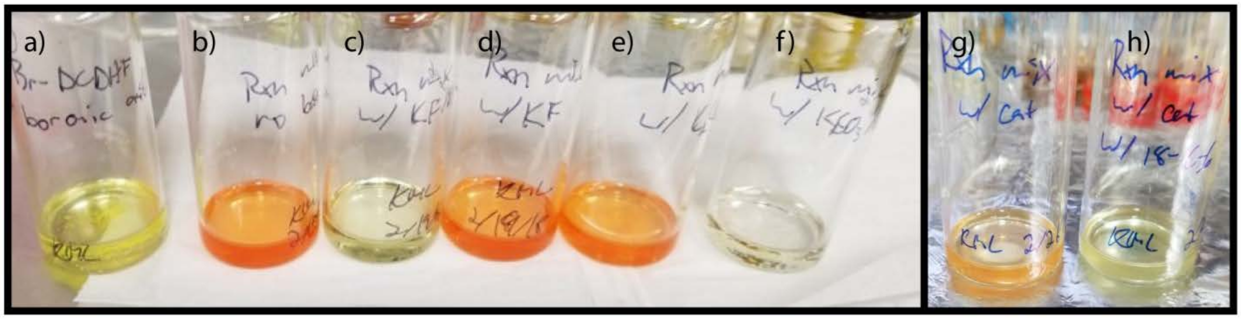

Figure 29: Reaction mixtures with various types of bases. All contain 4 mM each of **7** and **8** b)-h) contain 100 μM catalyst, a) no catalyst, no base b) no base c) KF, 18-C-6, d) KF, no 18-C-6, e) K_2CO_3, no 18-C-6, f) K_2CO_3, 18-C-6. g) no KF and no 18-C-6, h) no KF and with 18-C-6.

reaction proceeds quickly, with a visible color change within an hour. As the concentration of $Pd(PPh_3)_4$ is lowered, the reaction rate decreases, as expected. However, it has been determined that the concentration of $Pd(PPh_3)_4$ used affects the overall yield of the reaction. After sitting overnight, reaction mixtures with 10 μM $Pd(PPh_3)_4$ never reach the same yield as reaction mixtures with 100 μM, as can be seen in Figure 29. Thus, it is likely that the catalyst is deactivating before full conversion can happen. This is supported by the physical appearance of the catalyst solution. Upon first dissolution of $Pd(PPh_3)_4$ in toluene, the catalyst solution is a clear and pale yellow. After about an hour, the solution turns a murky brown. While we have not specifically analyzed the solution, the brown is likely from palladium black formation or aggregation, a common degradation product of Pd catalysts.[204]

To prevent $Pd(PPh_3)_4$ degradation, we added triphenylphosphine (PPh_3) as a stabilizer in the ratio of two parts PPh_3 to one part $Pd(PPh_3)_4$. However, PPh_3 did not appear to affect the stability of the catalyst, Figure 29.

4.4.4 Observation of DCDHF Formation in Droplets

Increase in fluorescence from reactions in single droplets was observed using vortexed emulsions and the poloxamer immobilization technique. At a catalyst concentration of 100 μM, fluorescence is very apparent, although at times little increase is seen over time because the reaction proceeds too fast. In Figure 30, examples from trajectories with 100 μM and 10 μM catalyst are shown. As the catalyst concentration is decreased, an increase in fluorescence is still visible down to 10 μM. Below this concentration, no increase in fluorescence is seen and in fact, fluorescence trajectories decrease. The decrease in fluorescence is likely caused by photobleaching, which cannot be outcompeted by fluorophore generation in the low-catalyst limit.

4.5 Conclusions and Future Directions

Droplet generation remains an area for improvement. Droplet sizes have been decreased to about 10 μm in size but further decreasing their size would be beneficial for achieving single-molecule droplet studies. To reach smaller droplets, work will have to be done in two areas. One, finding the ideal surfactant will make it easier to achieve both smaller and more stable droplets. However, identifying the ideal surfactant will be difficult because it depends on structure, concentration, and droplet producing conditions. The droplet generation conditions also have to be modified and better understood. As of now, little control of droplet generation is possible, and the mechanism of droplet generation needs to be better understood for better size control.

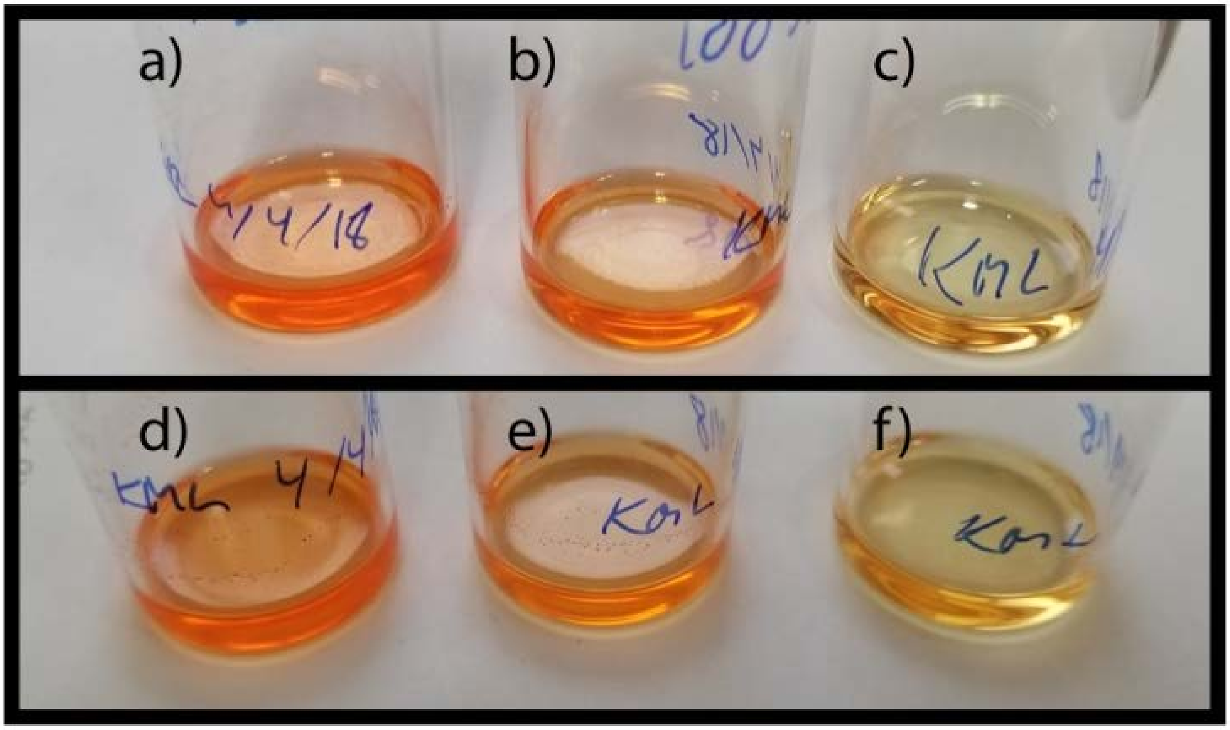

Figure 30: Reaction mixtures with various amounts of catalyst. All contain 4 mM each of **7** and **8.** a)-c) contain triphenyl phosphine at double concentration of catalyst and d)-f) contain only catalyst. a) and d) 100 μM $Pd(PPh_3)_4$, b) and e) 50 μM $Pd(PPh_3)_4$, c) and f) 10 μM $Pd(PPh_3)_4$. All reactions were left overnight at room temperature to react.

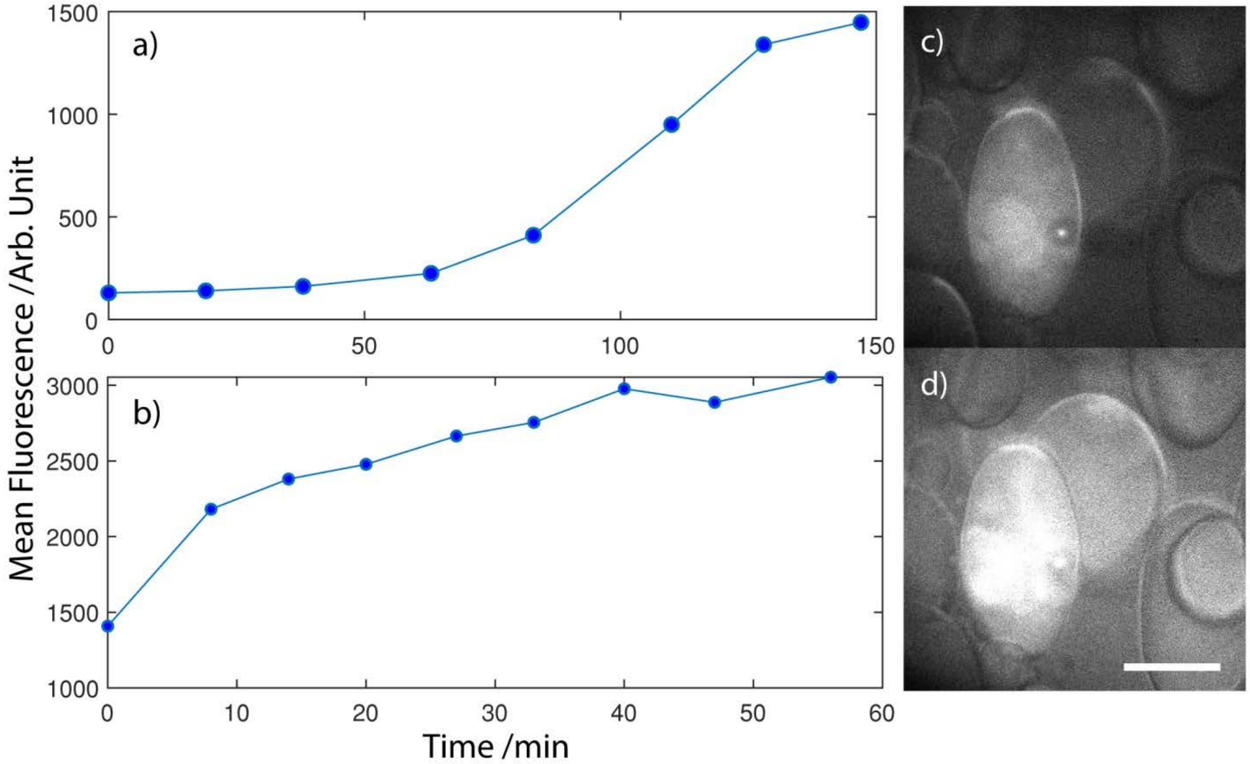

Figure 31: Example data. a) and b) Mean fluorescence intensity trajectories over time in individual droplets containing 4 mM each of **7** and **8** with a) 10 μM and b) 100 μM $Pd(PPh_3)_4$. Droplets from c) time 0 and d) time 9 (about an hour) from the 100 μM c $Pd(PPh_3)_4$ sample, trace b).

Progress has been made towards the observation of single turnover events in droplets of toluene. We have reached concentrations of 10 μM of catalyst in droplets, which corresponds to roughly $2.5x10^7$ catalyst molecules per 20 μm toluene droplet. This is still orders of magnitude higher than what is necessary for single-molecule studies. While decreasing the size of the droplets will raise the concentration of catalyst that can be used, the diameter of the droplets would have to be on the order of single nanometers to be able to maintain the $Pd(PPh_3)_4$ concentration currently being used. As we reach towards the limits of droplet size, we also strive to tune the reaction rate. As catalyst concentration is decreased, the rate and yield of the reaction decreases. Several methods could be tried to increase the rate and yield of the reaction. For one, to increase the rate of reaction, the reaction could be heated. As of yet, all experiments have been performed at room temperature but at the bulk level we have seen that heat will increase the reaction rate. To increase the yield of the reaction, degradation of the $Pd(PPh_3)_4$ will have to be prevented. Further studies with increased PPh_3 could be performed, although initial test reactions with additional PPh_3 failed. Other palladium catalysts could be used, such as $Pd(OAc)_2$ and derivatives[205-206] or PEPPSI.[148, 207]

Beyond the scope of this project, droplets have potential to be used for other single-molecule measurements. In particular, other work in our group is being done towards using droplets as minireactors for polymerization reactions wherein fluorescence anisotropy is used as a reporter for polymerization. Additionally, the development of small toluene-in-water droplets opens up the possibility of studying many other reactions which require organic solvents.

4.6 Acknowledgements

We would like to thank Andrew Cavell, James Ng, Veronica Krasecki, and Augie Witkowski for assistance with data acquisition, Sunil Upadhyay and Daniel Hinton for assistance with synthesis, and Angela Marquard for helpful conversations.

References

1. Schuler, B. Single Molecule Fret of Protein Folding Dynamics. *FASEB J.* **2009,** *23*.
2. Schuler, B.; Eaton, W. A. Protein Folding Studied by Single-Molecule Fret. *Curr Opin Struct Biol* **2008,** *18*, 16-26.
3. Chung, H. S.; McHale, K.; Louis, J. M.; Eaton, W. A. Single-Molecule Fluorescence Experiments Determine Protein Folding Transition Path Times. *Science* **2012,** *335*, 981-984.
4. Peterman, E. J. G.; Sosa, H.; Moerner, W. E. Single-Molecule Fluorescence Spectroscopy and Microscopy of Biomolecular Motors. *Annu Rev Phys Chem* **2004,** *55*, 79-96.
5. Vale, R. D.; Funatsu, T.; Pierce, D. W.; Romberg, L.; Harada, Y.; Yanagida, T. Direct Observation of Single Kinesin Molecules Moving Along Microtubules. *Nature* **1996,** *380*, 451-453.
6. Yildiz, A.; Tomishige, M.; Vale, R. D.; Selvin, P. R. Kinesin Walks Hand-over-Hand. *Science* **2004,** *303*, 676-678.
7. Min, W.; English, B. P.; Luo, G. B.; Cherayil, B. J.; Kou, S. C.; Xie, X. S. Fluctuating Enzymes: Lessons from Single-Molecule Studies. *Acc Chem Res* **2005,** *38*, 923-931.
8. Flomenbom, O.; Velonia, K.; Loos, D.; Masuo, S.; Cotlet, M.; Engelborghs, Y.; Hofkens, J.; Rowan, A. E.; Nolte, R. J. M.; Van der Auweraer, M.; de Schryver, F. C.; Klafter, J. Stretched Exponential Decay and Correlations in the Catalytic Activity of Fluctuating Single Lipase Molecules. *Proc Natl Acad Sci U S A* **2005,** *102*, 2368-2372.
9. Aratani, N.; Kim, D.; Osuka, A. Discrete Cyclic Porphyrin Arrays as Artificial Light-Harvesting Antenna. *Acc Chem Res* **2009,** *42*, 1922-1934.
10. Cotlet, M.; Vosch, T.; Habuchi, S.; Weil, T.; Mullen, K.; Hofkens, J.; De Schryver, F. Probing Intramolecular Forster Resonance Energy Transfer in a Naphthaleneimide-Peryleneimide-Terrylenediimide-Based Dendrimer by Ensemble and Single-Molecule Fluorescence Spectroscopy. *J Am Chem Soc* **2005,** *127*, 9760-9768.
11. Maus, M.; Mitra, S.; Lor, M.; Hofkens, J.; Weil, T.; Herrmann, A.; Mullen, K.; De Schryver, F. C. Intramolecular Energy Hopping in Polyphenylene Dendrimers with an Increasing Number of Peryleneimide Chromophores. *J Phys Chem A* **2001,** *105*, 3961-3966.
12. Bout, D. A. V.; Wai-Tak, Y.; Dehong, H.; Dian-Kui, F.; Swager, T. M.; Barbara, P. F. Discrete Intensity Jumps and Intramolecular Electronic Energy Transfer in the Spectroscopy of Single Conjugated Polymer Molecules. *Science* **1997,** *277*, 1074-1077.
13. Habuchi, S.; Onda, S.; Vacha, M. Molecular Weight Dependence of Emission Intensity and Emitting Sites Distribution within Single Conjugated Polymer Molecules. *Phys Chem Chem Phys* **2011,** *13*, 1743-1753.
14. Schindler, F.; Lupton, J. M.; Muller, J.; Feldmann, J.; Scherf, U. How Single Conjugated Polymer Molecules Respond to Electric Fields. *Nature Mat* **2006,** *5*, 141-146.
15. Kisley, L.; Landes, C. F. Molecular Approaches to Chromatography Using Single Molecule Spectroscopy. *Anal Chem* **2015,** *87*, 83-98.
16. Cooper, J. T.; Harris, J. M. Imaging Fluorescence-Correlation Spectroscopy for Measuring Fast Surface Diffusion at Liquid/Solid Interfaces. *Anal Chem* **2014,** *86*, 7618-7626.
17. Cooper, J.; Harris, J. M. Fluorescence-Correlation Spectroscopy Study of Molecular Transport within Reversed-Phase Chromatographic Particles Compared to Planar Model Surfaces. *Anal Chem* **2014,** *86*, 11766-11772.

18. Walder, R.; Nelson, N.; Schwartz, D. K. Single Molecule Observations of Desorption-Mediated Diffusion at the Solid-Liquid Interface. *Phys Rev Lett* **2011,** *107*.

19. Honciuc, A.; Harant, A. W.; Schwartz, D. K. Single-Molecule Observations of Surfactant Diffusion at the Solution-Solid Interface. *Langmuir* **2008,** *24*, 6562-6566.

20. Ng, J. D.; Upadhyay, S. P.; Marquard, A. N.; Lupo, K. M.; Hinton, D. A.; Padilla, N. A.; Bates, D. M.; Goldsmith, R. H. Single-Molecule Investigation of Initiation Dynamics of an Organometallic Catalyst. *J Am Chem Soc* **2016,** *138*, 3876-3883.

21. Esfandiari, N. M.; Wang, Y.; Bass, J. Y.; Cornell, T. P.; Otte, D. A. L.; Cheng, M. H.; Hemminger, J. C.; McIntire, T. M.; Mandelshtam, V. A.; Blum, S. A. Single-Molecule Imaging of Platinum Ligand Exchange Reaction Reveals Reactivity Distribution. *J Am Chem Soc* **2010,** *132*, 15167-15169.

22. Esfandiari, N.; Wang, Y.; McIntire, T.; Blum, S. Real-Time Imaging of Platinum-Sulfur Ligand Exchange Reactions at the Single-Molecule Level Via a General Chemical Technique. *Organometallics* **2011,** *30*, 2901-2907.

23. Canham, S.; Bass, J.; Navarro, O.; Lim, S.; Das, N.; Blum, S. Toward the Single-Molecule Investigation of Organometallic Reaction Mechanisms: Single-Molecule Imaging of Fluorophore-Tagged Palladium(Ii) Complexes. *Organometallics* **2008,** *27*, 2172-2175.

24. Easter, Q. T.; Blum, S. A. Evidence for Dynamic Chemical Kinetics at Individual Molecular Ruthenium Catalysts. *Angew Chem Int Ed* **2018,** *57*, 1572-1575.

25. Easter, Q. T.; Blum, S. A. Single Turnover at Molecular Polymerization Catalysts Reveals Spatiotemporally Resolved Reactions. *Angew Chem Int Ed* **2017,** *56*, 13772-13775.

26. Xu, W.; Kong, J.; Yeh, Y.; Chen, P. Single-Molecule Nanocatalysis Reveals Heterogeneous Reaction Pathways and Catalytic Dynamics. *Nat Mater* **2008,** *7*, 992-996.

27. Andoy, N. M.; Zhou, X. C.; Choudhary, E.; Shen, H.; Liu, G. K.; Chen, P. Single-Molecule Catalysis Mapping Quantifies Site-Specific Activity and Uncovers Radial Activity Gradient on Single 2d Nanocrystals. *J Am Chem Soc* **2013,** *135*, 1845-1852.

28. Tachikawa, T.; Yamashita, S.; Majima, T. Evidence for Crystal-Face-Dependent Tio2 Photocatalysis from Single-Molecule Imaging and Kinetic Analysis. *J Am Chem Soc* **2011,** *133*, 7197-7204.

29. Roeffaers, M. B. J.; Sels, B. F.; Uji-i, H.; De Schryver, F. C.; Jacobs, P. A.; De Vos, D. E.; Hofkens, J. Spatially Resolved Observation of Crystal-Face-Dependent Catalysis by Single Turnover Counting. *Nature* **2006,** *439*, 572-575.

30. Zhou, X. C.; Andoy, N. M.; Liu, G. K.; Choudhary, E.; Han, K. S.; Shen, H.; Chen, P. Quantitative Super-Resolution Imaging Uncovers Reactivity Patterns on Single Nanocatalysts. *Nat Nanotech* **2012,** *7*, 237-241.

31. Moerner, W. E.; Fromm, D. P. Methods of Single-Molecule Fluorescence Spectroscopy and Microscopy. *Rev Sci Instrum* **2003,** *74*, 3597-3619.

32. Maus, M.; De, R.; Lor, M.; Weil, T.; Mitra, S.; Wiesler, U. M.; Herrmann, A.; Hofkens, J.; Vosch, T.; Mullen, K.; De Schryver, F. C. Intramolecular Energy Hopping and Energy Trapping in Polyphenylene Dendrimers with Multiple Peryleneimide Donor Chromophores and a Terryleneimide Acceptor Trap Chromophore. *J Am Chem Soc* **2001,** *123*, 7668-7676.

33. Park, M.; Yoon, M.-C.; Yoon, Z. S.; Hori, T.; Peng, X.; Aratani, N.; Hotta, J.-i.; Uji-i, H.; Sliwa, M.; Hofkens, J.; Osuka, A.; Kim, D. Single-Molecule Spectroscopic Investigation of Energy Migration Processes in Cyclic Porphyrin Arrays. *J Am Chem Soc* **2007,** *129*, 3539-3544.

34. Weil, T.; Wiesler, U. M.; Herrmann, A.; Bauer, R.; Hofkens, J.; De Schryver, F. C.; Mullen, K. Polyphenylene Dendrimers with Different Fluorescent Chromophores Asymmetrically Distributed at the Periphery. *J Am Chem Soc* **2001,** *123*, 8101-8108.
35. Habuchi, S.; Onda, S.; Vacha, M. Mapping the Emitting Sites within a Single Conjugated Polymer Molecule. *Chem Comm* **2009**, 4868-4870.
36. Muller, J. G.; Lemmer, U.; Raschke, G.; Anni, M.; Scherf, U.; Lupton, J. M.; Feldmann, J. Linewidth-Limited Energy Transfer in Single Conjugated Polymer Molecules. *Phys Rev Lett* **2003,** *91*.
37. Thiessen, A.; Vogelsang, J.; Adachi, T.; Steiner, F.; Vanden Bout, D.; Lupton, J. M. Unraveling the Chromophoric Disorder of Poly(3-Hexylthiophene). *Proc Natl Acad Sci U S A* **2013,** *110*, E3550-E3556.
38. Vacha, M.; Habuchi, S. Conformation and Physics of Polymer Chains: A Single-Molecule Perspective. *Npg Asia Mater* **2010,** *2*, 134-142.
39. Rao, V. G.; Dhital, B.; He, Y.; Lu, H. P. Single-Molecule Interfacial Electron Transfer Dynamics of Porphyrin on TiO_2 Nanoparticles: Dissecting the Complex Electronic Coupling Dependent Dynamics. *J Phys Chem C* **2014,** *118*, 20209-20221.
40. Jin, S.; Lian, T. Electron Transfer Dynamics from Single CdSe/ZnS Quantum Dots to TiO_2 Nanoparticles. *Nano Lett* **2009,** *9*, 2448-2454.
41. Tachikawa, T.; Majima, T. Single-Molecule, Single-Particle Fluorescence Imaging of TiO_2-Based Photocatalytic Reactions. *Chem Soc Rev* **2010,** *39*, 4802-4819.
42. Cooper, J. T.; Peterson, E. M.; Harris, J. M. Fluorescence Imaging of Single-Molecule Retention Trajectories in Reversed-Phase Chromatographic Particles. *Anal Chem* **2013,** *85*, 9363-9370.
43. Kastantin, M.; Walder, R.; Schwartz, D. K. Identifying Mechanisms of Interfacial Dynamics Using Single-Molecule Tracking. *Langmuir* **2012,** *28*, 12443-12456.
44. Kisley, L.; Chen, J.; Mansur, A. P.; Shuang, B.; Kourentzi, K.; Poongavanam, M.-V.; Chen, W.-H.; Dhamane, S.; Willson, R. C.; Landes, C. F. Unified Superresolution Experiments and Stochastic Theory Provide Mechanistic Insight into Protein Ion-Exchange Adsorptive Separations. *Proc Natl Acad Sci U S A* **2014,** *111*, 2075-2080.
45. Cordes, T.; Blum, S. Opportunities and Challenges in Single-Molecule and Single-Particle Fluorescence Microscopy for Mechanistic Studies of Chemical Reactions. *Nature Chem* **2013,** *5*, 993-999.
46. Rybina, A.; Lang, C.; Wirtz, M.; Grussmayer, K.; Kurz, A.; Maier, F.; Schmitt, A.; Trapp, O.; Jung, G.; Herten, D.-P. Distinguishing Alternative Reaction Pathways by Single-Molecule Fluorescence Spectroscopy. *Angew Chem Int Ed* **2013,** *52*, 6322-6325.
47. Canham, S. M.; Bass, J. Y.; Navarro, O.; Lim, S.-G.; Das, N.; Blum, S. A. Toward the Single-Molecule Investigation of Organometallic Reaction Mechanisms: Single-Molecule Imaging of Fluorophore-Tagged Palladium(Ii) Complexes. *Organometallics* **2008,** *27*, 2172-2175.
48. Esfandiari, N.; Wang, Y.; Bass, J.; Cornell, T.; Otte, D.; Cheng, M.; Hemminger, J.; McIntire, T.; Mandelshtam, V.; Blum, S. Single-Molecule Imaging of Platinum Ligand Exchange Reaction Reveals Reactivity Distribution. *J Am Chem Soc* **2010,** *132*, 15167-15169.
49. Esfandiari, N. M.; Blum, S. A. Homogeneous Vs Heterogeneous Polymerization Catalysis Revealed by Single-Particle Fluorescence Microscopy. *J Am Chem Soc* **2011,** *133*, 18145-18147.
50. Loudet, A.; Burgess, K. Bodipy Dyes and Their Derivatives: Syntheses and Spectroscopic Properties. *Chem Rev* **2007,** *107*, 4891-4932.

51. Ulrich, G.; Ziessel, R.; Harriman, A. The Chemistry of Fluorescent Bodipy Dyes: Versatility Unsurpassed. *Angew Chem Int Ed* **2008,** *47*, 1184-1201.

52. Basche, T.; Moerner, W. E.; Orrit, M.; Talon, H. Photon Antibunching in the Fluorescence of a Single Dye Molecule Trapped in a Solid. *Phys Rev Lett* **1992,** *69*, 1516-1519.

53. Moerner, W. E.; Kador, L. Optical Detection and Spectroscopy of Single Molecules in a Solid. *Phys Rev Lett* **1989,** *62*, 2535-2538.

54. Orrit, M.; Bernard, J. Single Pentacene Molecules Detected by Fluorescence Excitation in a Para-Terphenyl Crystal. *Phys Rev Lett* **1990,** *65*, 2716-2719.

55. Hirschfeld, T. Optical Microscope Observation of Single Small Molecules. *Appl Opt* **1976,** *15*, 2965-2966.

56. Thompson, M. A.; Casolari, J. M.; Badieirostami, M.; Brown, P. O.; Moerner, W. E. Three-Dimensional Tracking of Single Mrna Particles in Saccharomyces Cerevisiae Using a Double-Helix Point Spread Function. *Proc Natl Acad Sci U S A* **2010,** *107*, 17864-17871.

57. Cotlet, M.; Gronheid, R.; Habuchi, S.; Stefan, A.; Barbafina, A.; Müllen, K.; Hofkens, J.; De Schryver, F. C. Intramolecular Directional Förster Resonance Energy Transfer at the Single-Molecule Level in a Dendritic System. *J Am Chem Soc* **2003,** *125*, 13609-13617.

58. De Schryver, F. C.; Vosch, T.; Cotlet, M.; Van der Auweraer, M.; Mullen, K.; Hofkens, J. Energy Dissipation in Multichromophoric Single Dendrimers. *Acc Chem Res* **2005,** *38*, 514-522.

59. Flors, C.; Oesterling, I.; Schnitzler, T.; Fron, E.; Schweitzer, G.; Sliwa, M.; Herrmann, A.; van der Auweraer, M.; de Schryver, F. C.; Mullen, K.; Hofkens, J. Energy and Electron Transfer in Ethynylene Bridged Perylene Diimide Multichromophores. *J Phys Chem C* **2007,** *111*, 4861-4870.

60. Hofkens, J.; Maus, M.; Gensch, T.; Vosch, T.; Cotlet, M.; Kohn, F.; Herrmann, A.; Mullen, K.; De Schryver, F. Probing Photophysical Processes in Individual Multichromophoric Dendrimers by Single-Molecule Spectroscopy. *J Am Chem Soc* **2000,** *122*, 9278-9288.

61. Ketelaars, M.; van Oijen, A. M.; Matsushita, M.; Kohler, J.; Schmidt, J.; Aartsma, T. J. Spectroscopy on the B850 Band of Individual Light-Harvesting 2 Complexes of Rhodopseudomonas Acidophila I. Experiments and Monte Carlo Simulations. *Biophys J* **2001,** *80*, 1591-1603.

62. Scholes, G. D.; Fleming, G. R.; Olaya-Castro, A.; van Grondelle, R. Lessons from Nature About Solar Light Harvesting. *Nat Chem* **2011,** *3*, 763-774.

63. van Oijen, A. M.; Ketelaars, M.; Kohler, J.; Aartsma, T. J.; Schmidt, J. Spectroscopy of Individual Light-Harvesting 2 Complexes of Rhodopseudomonas Acidophila: Diagonal Disorder, Intercomplex Heterogeneity, Spectral Diffusion, and Energy Transfer in the B800 Band. *Biophys J* **2000,** *78*, 1570-1577.

64. van Oort, B.; van Grondelle, R.; van Stokkum, I. H. M. A Hidden State in Light-Harvesting Complex Ii Revealed by Multipulse Spectroscopy. *J Phys Chem B* **2015,** *119*, 5184-5193.

65. Krüger, T. P. J.; Ilioaia, C.; Valkunas, L.; van Grondelle, R. Fluorescence Intermittency from the Main Plant Light-Harvesting Complex: Sensitivity to the Local Environment. *The J Phys Chem B* **2011,** *115*, 5083-5095.

66. Krüger, T. P. J.; Novoderezhkin, V. I.; Ilioaia, C.; van Grondelle, R. Fluorescence Spectral Dynamics of Single LHCII Trimers. *Biophys J* **2010** *98*, 3093-3101.

67. Barin, G.; Yilmaz, M. D.; Akkaya, E. U. Boradiazaindacene (Bodipy)-Based Building Blocks for the Construction of Energy Transfer Cassettes. *Tetrahedron Lett* **2009,** *50*, 1738-1740.

68. Bullock, J. E.; Carmieli, R.; Mickley, S. M.; Vura-Weis, J.; Wasielewski, M. R. Photoinitiated Charge Transport through Pi-Stacked Electron Conduits in Supramolecular Ordered Assemblies of Donor-Acceptor Triads. *J Am Chem Soc* **2009,** *131*, 11919-11929.

69. Gunderson, V. L.; Conron, S. M. M.; Wasielewski, M. R. Self-Assembly of a Hexagonal Supramolecular Light-Harvesting Array from Chlorophyll a Trefoil Building Blocks. *Chem Comm* **2010,** *46*, 401-403.

70. Kelley, R. F.; Goldsmith, R. H.; Wasielewski, M. R. Ultrafast Energy Transfer within Cyclic Self-Assembled Chlorophyll Tetramers. *J Am Chem Soc* **2007,** *129*, 6384-+.

71. Nagai, A.; Miyake, J.; Kokado, K.; Nagata, Y.; Chujo, Y. Highly Luminescent Bodipy-Based Organoboron Polymer Exhibiting Supramolecular Self-Assemble Structure. *J Am Chem Soc* **2008,** *130*, 15276-+.

72. Rio, Y.; Seitz, W.; Gouloumis, A.; Vazquez, P.; Sessler, J. L.; Guldi, D. M.; Torres, T. A Panchromatic Supramolecular Fullerene-Based Donor-Acceptor Assembly Derived from a Peripherally Substituted Bodipy-Zinc Phthalocyanine Dyad. *Chem Eur J* **2010,** *16*, 1929-1940.

73. Yilmaz, M. D.; Bozdemir, O. A.; Akkaya, E. U. Light Harvesting and Efficient Energy Transfer in a Boron-Dipyrrin (Bodipy) Functionalized Perylenediimide Derivative. *Org Lett* **2006,** *8*, 2871-2873.

74. Haugland, R. P., Handbook of Molecular Probes and Research Products. 9th ed.; Molecular Probes, Inc.: Eugene, OR, 2002.

75. Frein, S.; Camerel, F.; Ziessel, R.; Barbera, J.; Deschenaux, R. Highly Fluorescent Liquid-Crystalline Dendrimers Based on Borondipyrromethene Dyes. *Chem Mater* **2009,** *21*, 3950-3959.

76. Lakowicz, J. R., *Principles of Fluorescence Spectroscopy*. 3rd ed.; Springer: Singapore, 2006.

77. Hu, R.; Lager, E.; Aguilar-Aguilar, A.; Liu, J.; Lam, J.; Sung, H.; Williams, I.; Zhong, Y.; Wong, K.; Pena-Cabrera, E.; Tang, B. Twisted Intramolecular Charge Transfer and Aggregation-Induced Emission of Bodipy Derivatives. *J Phys Chem C* **2009,** *113*, 15845-15853.

78. Choi, S.; Bouffard, J.; Kim, Y. Aggregation-Induced Emission Enhancement of a Meso-Trifluoromethyl Bodipy Via J-Aggregation. *Chem Sci* **2014,** *5*, 751-755.

79. Turro, N. Modern Molecular Photochemistry. 1991.

80. Herman, T. K.; Mackowiak, S. A.; Kaufman, L. J. High Power Light Emitting Diode Based Setup for Photobleaching Fluorescent Impurities. *Rev Sci Instrum* **2009,** *80*.

81. Bakshi, S.; Dalrymple, R. M.; Li, W.; Choi, H.; Weisshaar, J. C. Partitioning of Rna Polymerase Activity in Live Escherichia Coli from Analysis of Single-Molecule Diffusive Trajectories. *Biophys J* **2013,** *105*, 2676-2686.

82. Watkins, L. P.; Yang, H. Detection of Intensity Change Points in Time-Resolved Single-Molecule Measurements. *J Phys Chem B* **2005,** *109*, 617-628.

83. Lord, S. J.; Lu, Z.; Wang, H.; Willetst, K. A.; Schuck, P. J.; Lee, H.-L. D.; Nishimura, S. Y.; Twieg, R. J.; Moerner, W. E. Photophysical Properties of Acene Dcdhf Fluorophores: Long-Wavelength Single-Molecule Emitters Designed for Cellular Imaging. *J Phys Chem A* **2007,** *111*, 8934-8941.

84. Bopp, M. A.; Jia, Y. W.; Li, L. Q.; Cogdell, R. J.; Hochstrasser, R. M. Fluorescence and Photobleaching Dynamics of Single Light-Harvesting Complexes. *Proc Natl Acad Sci U S A* **1997,** *94*, 10630-10635.

85. Goldsmith, R.; Moerner, W. Watching Conformational- and Photodynamics of Single Fluorescent Proteins in Solution. *Nature Chem* **2010,** *2*, 179-186.

86. Berglund, A. J.; Doherty, A. C.; Mabuchi, H. Photon Statistics and Dynamics of Fluorescence Resonance Energy Transfer. *Phys Rev Lett* **2002,** *89*.

87. Aitken, C. E.; Marshall, R. A.; Puglisi, J. D. An Oxygen Scavenging System for Improvement of Dye Stability in Single-Molecule Fluorescence Experiments. *Biophys J* **2008,** *94*, 1826-1835.

88. Dave, R.; Terry, D. S.; Munro, J. B.; Blanchard, S. C. Mitigating Unwanted Photophysical Processes for Improved Single-Molecule Fluorescence Imaging. *Biophys J* **2009,** *96*, 2371-2381.

89. Rasnik, I.; McKinney, S. A.; Ha, T. Nonblinking and Longlasting Single-Molecule Fluorescence Imaging. *Nature Meth* **2006,** *3*, 891-893.

90. Vogelsang, J.; Kasper, R.; Steinhauer, C.; Person, B.; Heilemann, M.; Sauer, M.; Tinnefeld, P. A Reducing and Oxidizing System Minimizes Photobleaching and Blinking of Fluorescent Dyes. *Angew Chem Int Ed* **2008,** *47*, 5465-5469.

91. Sliwa, M.; Flors, C.; Oesterling, I.; Hotta, J.; Muellen, K.; De Schryver, F. C.; Hofkens, J. Single Perylene Diimide Dendrimers as Single-Photon Sources. *J Phys: Condens Matter* **2007,** *19*.

92. Valkunas, L.; Liuolia, V.; Freiberg, A. Picosecond Processes in Chromatophores at Various Excitation Intensities. *Phot Res* **1991,** *27*, 83-95.

93. Vanmourik, F.; Vanderoord, C. J. R.; Visscher, K. J.; Parkesloach, P. S.; Loach, P. A.; Visschers, R. W.; Vangrondelle, R. Exciton Interactions in the Light-Harvesting Antenna of Photosynthetic Bacteria Studied with Triplet-Singlet Spectroscopy and Singlet-Triplet Annihilation on the B820 Subunit Form of Rhodospirillum-Rubrum. *Biochim Biophys Acta* **1991,** *1059*, 111-119.

94. Gruber, M.; Chmeliov, J.; Kruger, T. P. J.; Valkunas, L.; van Grondelle, R. Singlet-Triplet Annihilation in Single Lhcii Complexes. *Phys Chem Chem Phys* **2015**.

95. Ying, L.; Xie, X. S. Fluorescence Spectroscopy, Exciton Dynamics, and Photochemistry of Single Allophycocyanin Trimers. *J Phys Chem B* **1998,** *102*, 10399-10409.

96. Zaushitsyn, Y.; Jespersen, K. G.; Valkunas, L.; Sundstrom, V.; Yartsev, A. Ultrafast Dynamics of Singlet-Singlet and Singlet-Triplet Exciton Annihilation in Poly(3-2 '-Methoxy-5 '-Octylphenyl)Thiophene Films. *Phys Rev B* **2007,** *75*.

97. Steiner, F.; Vogelsang, J.; Lupton, J. M. Singlet-Triplet Annihilation Limits Exciton Yield in Poly(3-Hexylthiophene). *Phys Rev Lett* **2014,** *112*, 137402.

98. Wang, X. F.; Koyama, Y.; Nagae, H.; Yamano, Y.; Ito, M.; Wada, Y. Photocurrents of Solar Cells Sensitized by Aggregate-Forming Polyenes: Enhancement Due to Suppression of Singlet-Triplet Annihilation by Lowering of Dye Concentration or Light Intensity. *Chem Phys Lett* **2006,** *420*, 309-315.

99. Hofkens, J.; Schroeyers, W.; Loos, D.; Cotlet, M.; Kohn, F.; Vosch, T.; Maus, M.; Herrmann, A.; Mullen, K.; Gensch, T.; De Schryver, F. C. Triplet States as Non-Radiative Traps in Multichromophoric Entities: Single Molecule Spectroscopy of an Artificial and Natural Antenna System. *Spectrochim Acta, Part A* **2001,** *57*, 2093-2107.

100. Tinnefeld, P.; Buschmann, V.; Weston, K. D.; Sauer, M. Direct Observation of Collective Blinking and Energy Transfer in a Bichromophoric System. *J Phys Chem A* **2003,** *107*, 323-327.

101. Tinnefeld, P.; Hofkens, J.; Herten, D.-P.; Masuo, S.; Vosch, T.; Cotlet, M.; Habuchi, S.; Müllen, K.; De Schryver, F. C.; Sauer, M. Higher-Excited-State Photophysical Pathways in Multichromophoric Systems Revealed by Single-Molecule Fluorescence Spectroscopy. *Chem Phys Chem* **2004,** *5*, 1786-1790.

102. Montejano, H. A.; Amat-Guerri, F.; Costela, A.; Garcia-Moreno, I.; Liras, M.; Sastre, R. Triplet-State Spectroscopy of Dipyrromethene·Bf2 Laser Dyes. *J Photochem Photobiol A* **2006,** *181*, 142-146.

103. Stewart, J. J. P. Optimization of Parameters for Semiempirical Methods V: Modification of Nddo Approximations and Application to 70 Elements. *J Mol Model* **2007,** *13*, 1173-1213.

104. Arbeloa, F. L.; Banuelos, J.; Martinez, V.; Arbeloa, T.; Arbeloa, I. P. Structural, Photophysical and Lasing Properties of Pyrromethene Dyes. *Int Rev Phys Chem* **2005,** *24*, 339-374.

105. Assor, Y.; Burshtein, Z.; Rosenwaks, S. Spectroscopy and Laser Characteristics of Copper-Vapor-Laser Pumped Pyrromethene-556 and Pyrromethene-567 Dye Solutions. *Appl Opt* **1998,** *37*, 4914-4920.

106. Costela, A.; Garcia-Moreno, I.; Gomez, C.; Sastre, R.; Amat-Guerri, F.; Liras, M.; Arbeloa, F. L.; Prieto, J. B.; Arbeloa, I. L. Photophysical and Lasing Properties of New Analogs of the Boron-Dipyrromethene Laser Dye Pm567 in Liquid Solution. *J Phys Chem A* **2002,** *106*, 7736-7742.

107. Lam, S. Y.; Damzen, M. J. Characterisation of Solid-State Dyes and Their Use as Tunable Laser Amplifiers. *Appl Phys B* **2003,** *77*, 577-584.

108. Schmitt, A.; Hinkeldey, B.; Wild, M.; Jung, G. Synthesis of the Core Compound of the Bodipy Dye Class: 4,4'-Difluoro-4-Bora-(3a,4a)-Diaza-S-Indacene. *J. Fluoresce* **2009,** *19*, 755-758.

109. Adarsh, N.; Avirah, R. R.; Ramaiah, D. Tuning Photosensitized Singlet Oxygen Generation Efficiency of Novel Aza-Bodipy Dyes. *Org Lett* **2010,** *12*, 5720-5723.

110. Choplin, A.; Quignard, F. From Supported Homogeneous Catalysts to Heterogeneous Molecular Catalysts. *Coord Chem Rev* **1998,** *178*, 1679-1702.

111. Notestein, J. M.; Katz, A. Enhancing Heterogeneous Catalysis through Cooperative Hybrid Organic-Inorganic Interfaces. *Chem Eur J* **2006,** *12*, 3954-3965.

112. Canlas, C. P.; Lu, J.; Ray, N. A.; Grosso-Giordano, N. A.; Lee, S.; Elam, J. W.; Winans, R. E.; Van Duyne, R. P.; Stair, P. C.; Notestein, J. M. Shape-Selective Sieving Layers on an Oxide Catalyst Surface. *Nature Chem* **2012,** *4*, 1030-1036.

113. Hintermair, U.; Francio, G.; Leitner, W. Continuous Flow Organometallic Catalysis: New Wind in Old Sails. *Chem Comm* **2011,** *47*, 3691-3701.

114. Zhao, D.; Ding, K. Recent Advances in Asymmetric Catalysis in Flow. *ACS Catal* **2013,** *3*, 928-944.

115. McCrory, C. C. L.; Devadoss, A.; Ottenwaelder, X.; Lowe, R. D.; Stack, T. D. P.; Chidsey, C. E. D. Electrocatalytic O-2 Reduction by Covalently Immobilized Mononuclear Copper(I) Complexes: Evidence for a Binuclear Cu_2O_2 Intermediate. *J Am Chem Soc* **2011,** *133*, 3696-3699.

116. Coggins, M. K.; Mendez, M. A.; Concepcion, J. J.; Periana, R. A.; Meyer, T. J. Selective Electrocatalytic Oxidation of a Re-Methyl Complex to Methanol by a Surface-Bound Ru-Ii Polypyridyl Catalyst. *J Am Chem Soc* **2014,** *136*, 15845-15848.

117. Bluemel, J. Linkers and Catalysts Immobilized on Oxide Supports: New Insights by Solid-State Nmr Spectroscopy. *Coord Chem Rev* **2008,** *252*, 2410-2423.

118. Cantillo, D.; Kappe, C. O. Immobilized Transition Metals as Catalysts for Cross-Couplings in Continuous Flow-a Critical Assessment of the Reaction Mechanism and Metal Leaching. *Chemcatchem* **2014,** *6*, 3286-3305.

119. Tandukar, S.; Sen, A. N-Heterocyclic Carbene-Palladium Complex Immobilized on Silica Nanoparticles - Recyclable Catalyst for High Yield Suzuki and Heck Coupling Reactions under Mild Conditions. *J Mol Cat A: Chem* **2007,** *268*, 112-119.

120. Mehendale, N. C.; Bezemer, C.; van Walree, C. A.; Gebbink, R. J. M. K.; van Koten, G. Novel Silica Immobilized Ncn-Pincer Palladium(Ii) and Platinum(Ii) Complexes: Application as Lewis Acid Catalysts. *J Mol Cat A: Chem* **2006,** *257*, 167-175.

121. Bigi, F.; Corradini, A.; Quarantelli, C.; Sartori, G. Silica-Bound Decatungstates as Heterogeneous Catalysts for H_2O_2 Activation in Selective Sulfide Oxidation. *J Catal* **2007,** *250*, 222-230.

122. Bandini, M.; Luque, R.; Budarin, V.; Macquarrie, D. J. Aryl Alkynylation Versus Alkyne Homocoupling: Unprecedented Selectivity Switch in Cu, Phosphine and Solvent-Free Heterogeneous Pd-Catalysed Couplings. *Tetrahedron* **2005,** *61*, 9860-9868.

123. Crudden, C. M.; Sateesh, M.; Lewis, R. Mercaptopropyl-Modified Mesoporous Silica: A Remarkable Support for the Preparation of a Reusable, Heterogeneous Palladium Catalyst for Coupling Reactions. *J Am Chem Soc* **2005,** *127*, 10045-10050.

124. Phan, N. T. S.; Van Der Sluys, M.; Jones, C. W. On the Nature of the Active Species in Palladium Catalyzed Mizoroki-Heck and Suzuki-Miyaura Couplings - Homogeneous or Heterogeneous Catalysis, a Critical Review. *Adv Synth Catal* **2006,** *348*, 609-679.

125. Weck, M.; Jones, C. W. Mizoroki-Heck Coupling Using Immobilized Molecular Precatalysts: Leaching Active Species from Pd Pincers, Entrapped Pd Salts, and Pdnhc Complexes. *Inorg Chem* **2007,** *46*, 1865-1875.

126. Claessens, H. A.; van Straten, M. A. Review on the Chemical and Thermal Stability of Stationary Phases for Reversed-Phase Liquid Chromatography. *J Chromatogr A* **2004,** *1060*, 23-41.

127. Pirkle, W. H.; Finn, J. M.; Schreiner, J. L.; Hamper, B. C. A Widely Useful Chiral Stationary Phase for the High-Performance Liquid-Chromatography Separation of Enantiomers. *J Am Chem Soc* **1981,** *103*, 3964-3966.

128. Song, Z. H.; Wu, D. P.; Ding, K.; Guan, Y. F. Preparation of Alumina Nanoshell Coated Porous Silica Spheres for Inorganic Anions Separation. *J Chromatogr A* **2016,** *1433*, 85-89.

129. Batth, T. S.; Francavilla, C.; Olsen, J. V. Off-Line High-Ph Reversed-Phase Fractionation for in-Depth Phosphoproteomics. *J Proteome Res* **2014,** *13*, 6176-6186.

130. Kirkland, J. J.; Vanstraten, M. A.; Claessens, H. A. High Ph Mobile-Phase Effects on Silica-Based Reversed-Phase High-Performance Liquid-Chromatographic Columns. *J Chromatogr A* **1995,** *691*, 3-19.

131. Nawrocki, J. The Silanol Group and Its Role in Liquid Chromatography. *J Chromatogr A* **1997,** *779*, 29-71.

132. Pantano, C. G.; Wittberg, T. N. Xps Analysis of Silane Coupling Agents and Silane-Treated E-Glass Fibers. *Surf Interface Anal* **1990,** *15*, 498-501.

133. Bhairamadgi, N. S.; Pujari, S. P.; Trovela, F. G.; Debrassi, A.; Khamis, A. A.; Alonso, J. M.; Al Zahrani, A. A.; Wennekes, T.; Al-Turaif, H. A.; van Rijn, C.; Alhamed, Y. A.; Zuilhof, H. Hydrolytic and Thermal Stability of Organic Mono Layers on Various Inorganic Substrates. *Langmuir* **2014,** *30*, 5829-5839.

134. Araujo, Y. C.; Toledo, P. G.; Leon, V.; Gonzalez, H. Y. Wettability of Silane-Treated Glass Slides as Determined from X-Ray Photoelectron Spectroscopy. *J Colloid Interface Sci* **1995,** *176*, 485-490.

135. Frydman, E.; Cohen, H.; Maoz, R.; Sagiv, J. Monolayer Damage in Xps Measurements as Evaluated by Independent Methods. *Langmuir* **1997,** *13*, 5089-5106.

136. Krishnan, A.; Liu, Y. H.; Cha, P.; Woodward, R.; Allara, D.; Vogler, E. A.; Hematology Biomater Inter Res, G. An Evaluation of Methods for Contact Angle Measurement. *Colloids Surf B* **2005,** *43*, 95-98.

137. Wirth, M. J.; Legg, M. A. Single-Molecule Probing of Adsorption and Diffusion on Silica Surfaces. *Ann Rev Phys Chem* **2007,** *58*, 489-510.

138. Lebold, T.; Michaelis, J.; Brauchle, C. The Complexity of Mesoporous Silica Nanomaterials Unravelled by Single Molecule Microscopy. *Phys Chem Chem Phys* **2011,** *13*, 5017-5033.

139. Walder, R.; Nelson, N.; Schwartz, D. K. Single Molecule Observations of Desorption-Mediated Diffusion at the Solid-Liquid Interface. *Phys Rev Lett* **2011,** *107*, 156102.

140. Honciuc, A.; Harant, A. W.; Schwartz, D. K. Single-Molecule Observations of Surfactant Diffusion at the Solution−Solid Interface. *Langmuir* **2008,** *24*, 6562-6566.

141. Higgins, D. A.; Collinson, M. M. Gaining Insight into the Nanoscale Properties of Sol−Gel-Derived Silicate Thin Films by Single-Molecule Spectroscopy. *Langmuir* **2005,** *21*, 9023-9031.

142. Higgins, D. A.; Park, S. C.; Tran-Ba, K.-H.; Ito, T. Single-Molecule Investigations of Morphology and Mass Transport Dynamics in Nanostructured Materials. *Ann Rev Anal Chem* **2015,** *8*, 193-216.

143. Borja, G.; Monge-Marcet, A.; Pleixats, R.; Parella, T.; Cattoen, X.; Man, M. W. C. Recyclable Hybrid Silica-Based Catalysts Derived from Pd-Nhc Complexes for Suzuki, Heck and Sonogashira Reactions. *Eur J Org Chem* **2012**, 3625-3635.

144. Polshettiwar, V.; Len, C.; Fihri, A. Silica-Supported Palladium: Sustainable Catalysts for Cross-Coupling Reactions. *Coord Chem Rev* **2009,** *253*, 2599-2626.

145. Roeffaers, M. B. J.; De Cremer, G.; Uji-i, H.; Muls, B.; Sels, B. F.; Jacobs, P. A.; De Schryver, F. C.; De Vos, D. E.; Hofkens, J. Single-Molecule Fluorescence Spectroscopy in (Bio)Catalysis. *Proc Natl Acad Sci U S A* **2007,** *104*, 12603-12609.

146. Upadhyay, S. P.; Lupo, K. M.; Marquard, A. N.; Ng, J. D.; Bates, D. M.; Goldsmith, R. H. Fluorescent Dendrimeric Molecular Catalysts Demonstrate Unusual Scaling Behavior at the Single-Molecule Level. *J Phys Chem C* **2015,** *119*, 19703-19714.

147. Wasserman, S. R.; Tao, Y. T.; Whitesides, G. M. Structure and Reactivity of Alkylsiloxane Monolayers Formed by Reaction of Alkyltrichlorosilanes on Silicon Substrates. *Langmuir* **1989,** *5*, 1074-1087.

148. O'Brien, C. J.; Kantchev, E. A. B.; Valente, C.; Hadei, N.; Chass, G. A.; Lough, A.; Hopkinson, A. C.; Organ, M. G. Easily Prepared Air- and Moisture-Stable Pd-Nhc (Nhc = N-Heterocyclic Carbene) Complexes: A Reliable, User-Friendly, Highly Active Palladium Precatalyst for the Suzuki-Miyaura Reaction. *Chem Eur J* **2006,** *12*, 4743-4748.

149. Hernan, P.; Delpino, C.; Ruizhitzky, E. Rhodium Complexes with Nitrogen-Donor Ligands Anchored on Silicic Supports .1. Synthesis and Characterization. *Chem Mater* **1992,** *4*, 49-55.

150. Tamaki, R.; Chujo, Y. Synthesis of Poly(Vinyl Alcohol) Silica Gel Polymer Hybrids by in-Situ Hydrolysis Method. *App Organomet Chem* **1998,** *12*, 755-762.

151. Brunel, D.; Cauvel, A.; Di Renzo, F.; Fajula, F.; Fubini, B.; Onida, B.; Garrone, E. Preferential Grafting of Alkoxysilane Coupling Agents on the Hydrophobic Portion of the Surface of Micelle-Templated Silica. *New J Chem* **2000,** *24*, 807-813.

152. Waddell, T. G.; Leyden, D. E.; Debello, M. T. The Nature of Organosilane to Silica-Surface Bonding. *J Am Chem Soc* **1981,** *103*, 5303-5307.

153. Schunk, T. C.; Burke, M. F. Bonded Phase Conformation and Solvation Effects on the Stationary-Phase Structure in Reversed-Phase Liquid-Chromatography. *J Chromatogr A* **1993,** *656*, 289-316.

154. Vandenberg, E. T.; Bertilsson, L.; Liedberg, B.; Uvdal, K.; Erlandsson, R.; Elwing, H.; Lundstrom, I. Structure of 3-Aminopropyl Triethoxy Silane on Silicon-Oxide. *J Colloid Interface Sci* **1991,** *147*, 103-118.

155. Witucki, G. L. A Silane Primer: Chemistry and Applications of Alkoxy Silanes. *J Coat Tech* **1993,** *65*, 57-57.

156. Abernethy, R. B.; Breneman, J.; Medlin, C.; Reinman, G. L. *Weibull Analysis Handbook.* ; DTIC Document: 1983.

157. Lindsey, C. P.; Patterson, G. D. Detailed Comparison of the Williams-Watts and Cole-Davidson Functions. *J Chem Phys* **1980,** *73*, 3348-3357.

158. Berberan-Santos, M. N.; Bodunov, E. N.; Valeur, B. Mathematical Functions for the Analysis of Luminescence Decays with Underlying Distributions 1. Kohlrausch Decay Function (Stretched Exponential). *Chem Phys* **2005,** *315*, 171-182.

159. Lu, H. P.; Xun, L.; Xie, X. S. Single-Molecule Enzymatic Dynamics. *Science* **1998,** *282*, 1877-1882.

160. Xu, W.; Kong, J. S.; Yeh, Y.-T. E.; Chen, P. Single-Molecule Nanocatalysis Reveals Heterogeneous Reaction Pathways and Catalytic Dynamics. *Nat Mater* **2008,** *7*, 992-996.

161. Chuang, I. S.; Maciel, G. E. Probing Hydrogen Bonding and the Local Environment of Silanols on Silica Surfaces Via Nuclear Spin Cross Polarization Dynamics. *J Am Chem Soc* **1996,** *118*, 401-406.

162. Bartram, M. E.; Michalske, T. A.; Rogers, J. W. A Reexamination of the Chemisorption of Trimethylaluminum on Silica. *J Phys Chem* **1991,** *95*, 4453-4463.

163. Jal, P. K.; Patel, S.; Mishra, B. Chemical Modification of Silica Surface by Immobilization of Functional Groups for Extractive Concentration of Metal Ions. *Talanta* **2004,** *62*, 1005-1028.

164. Sneh, O.; George, S. M. Thermal-Stability of Hydroxyl-Groups on a Well-Defined Silica Surface. *J Phys Chem* **1995,** *99*, 4639-4647.

165. Copéret, C.; Chabanas, M.; Petroff Saint-Arroman, R.; Basset, J.-M. Homogeneous and Heterogeneous Catalysis: Bridging the Gap through Surface Organometallic Chemistry. *Angew Chem Int Ed* **2003,** *42*, 156-181.

166. Vaccaro, L.; Cannas, M.; Radzig, V.; Boscaino, R. Luminescence of the Surface Nonbridging Oxygen Hole Center in Silica: Spectral and Decay Properties. *Phys Rev B* **2008,** *78*, 075421.

167. Hoang, P. H.; Yoon, K. B.; Kim, D. P. Synthesis of Hierarchically Porous Zeolite a Crystals with Uniform Particle Size in a Droplet Microreactor. *SSC Adv* **2012,** *2*, 5323-5328.

168. Liu, D. Y.; Liang, G. T.; Lei, X. X.; Chen, B.; Wang, W.; Zhou, X. M. Highly Efficient Capillary Polymerase Chain Reaction Using an Oscillation Droplet Microreactor. *Anal Chim Acta* **2012,** *718*, 58-63.

169. He, M. Y.; Edgar, J. S.; Jeffries, G. D. M.; Lorenz, R. M.; Shelby, J. P.; Chiu, D. T. Selective Encapsulation of Single Cells and Subcellular Organelles into Picoliter- and Femtoliter-Volume Droplets. *Anal Chem* **2005,** *77*, 1539-1544.

170. Sun, X. F.; Tang, K. Q.; Smith, R. D.; Kelly, R. T. Controlled Dispensing and Mixing of Pico- to Nanoliter Volumes Using on-Demand Droplet-Based Microfluidics. *Microfluid Nanofluidics* **2013,** *15*, 117-126.

171. Churski, K.; Korczyk, P.; Garstecki, P. High-Throughput Automated Droplet Microfluidic System for Screening of Reaction Conditions. *Lab Chip* **2010,** *10*, 816-818.
172. Lagus, T. P.; Edd, J. F. A Review of the Theory, Methods and Recent Applications of High-Throughput Single-Cell Droplet Microfluidics. *J Phys D* **2013,** *46*.
173. Musyanovych, A.; Mailander, V.; Landfester, K. Miniemulsion Droplets as Single Molecule Nanoreactors for Polymerase Chain Reaction. *Biomacromolecules* **2005,** *6*, 1824-1828.
174. Leng, X. F.; Zhang, W. H.; Wang, C. M.; Cui, L. A.; Yang, C. J. Agarose Droplet Microfluidics for Highly Parallel and Efficient Single Molecule Emulsion Pcr. *Lab Chip* **2010,** *10*, 2841-2843.
175. Rotman, B. Measurement of Activity of Single Molecules of Beta-D-Galactosidase. *Proc Nat Acad Sci U S A* **1961,** *47*, 1981-&.
176. Sakakihara, S.; Araki, S.; Iino, R.; Noji, H. A Single-Molecule Enzymatic Assay in a Directly Accessible Femtoliter Droplet Array. *Lab Chip* **2010,** *10*, 3355-3362.
177. Upadhiyay, S. P.; Lupo, K. M.; Marquard, A. N.; Ng, J. D.; Bates, D. M.; Goldsmith, R. H. Fluorescent Dendrimeric Molecular Catalysts Demonstrate Unusual Scaling Behavior at the Single-Molecule Level. *J Phys Chem C* **2015,** *119*, 19703-19714.
178. Lupo, K. M.; Hinton, D. A.; Ng, J. D.; Padilla, N. A.; Goldsmith, R. H. Probing Heterogeneity and Bonding at Silica Surfaces through Single-Molecule Investigation of Base-Mediated Linkage Failure. *Langmuir* **2016,** *32*, 9171-9179.
179. Suzuki, A. Carbon-Carbon Bonding Made Easy. *Chem Comm* **2005**, 4759-4763.
180. MorenoManas, M.; Perez, M.; Pleixats, R. Palladium-Catalyzed Suzuki-Type Self-Coupling of Arylboronic Acids. A Mechanistic Study. *J Org Chem* **1996,** *61*, 2346-2351.
181. Lord, S. J.; Conley, N. R.; Lee, H. L. D.; Nishimura, S. Y.; Pomerantz, A. K.; Willets, K. A.; Lu, Z. K.; Wang, H.; Liu, N.; Samuel, R.; Weber, R.; Semyonov, A.; He, M.; Twieg, R. J.; Moerner, W. E. DCDHF Fluorophores for Single-Molecule Imaging in Cells. *Chemphyschem* **2009,** *10*, 55-65.
182. Williams, J. M. High Internal Phase Water-in-Oil Emulsions - Influence of Surfactants and Cosurfactants on Emulsion Stability and Foam Quality. *Langmuir* **1991,** *7*, 1370-1377.
183. Leong, T. S. H.; Wooster, T. J.; Kentish, S. E.; Ashokkumar, M. Minimising Oil Droplet Size Using Ultrasonic Emulsification. *Ultrason Sonochem* **2009,** *16*, 721-727.
184. Lethuaut, L.; Metro, F.; Genot, C. Effect of Droplet Size on Lipid Oxidation Rates of Oil-in-Water Emulsions Stabilized by Protein. *J Am Oil Chem Soc* **2002,** *79*, 425-430.
185. McClements, D. J.; Dungan, S. R. Light-Scattering Study of Solubilization of Emulsion Droplets by Nonionic Surfactant Solutions. *Colloids Surf A* **1995,** *104*, 127-135.
186. Abate, A. R.; Lee, D.; Do, T.; Holtze, C.; Weitz, D. A. Glass Coating for Pdms Microfluidic Channels by Sol-Gel Methods. *Lab Chip* **2008,** *8*, 516-518.
187. Yim, T. J.; Zentgraf, T.; Min, B.; Zhang, X. All-Liquid Photonic Microcavity Stabilized by Quantum Dots. *J Am Chem Soc* **2010,** *132*, 2154-+.
188. Lee, J. N.; Park, C.; Whitesides, G. M. Solvent Compatibility of Poly(Dimethylsiloxane)-Based Microfluidic Devices. *Anal Chem* **2003,** *75*, 6544-6554.
189. Bauer, W. A. C.; Fischlechner, M.; Abell, C.; Huck, W. T. S. Hydrophilic Pdms Microchannels for High-Throughput Formation of Oil-in-Water Microdroplets and Water-in-Oil-in-Water Double Emulsions. *Lab Chip* **2010,** *10*, 1814-1819.
190. Utada, A. S.; Fernandez-Nieves, A.; Stone, H. A.; Weitz, D. A. Dripping to Jetting Transitions in Coflowing Liquid Streams. *Phys Rev Lett* **2007,** *99*.

191. Cabana, A.; AitKadi, A.; Juhasz, J. Study of the Gelation Process of Polyethylene Oxide(a) Polypropylene Oxide(B) Polyethylene Oxide(a) Copolymer (Poloxamer 407) Aqueous Solutions. *J Colloid Interface Sci* **1997,** *190*, 307-312.

192. Lenaerts, V.; Triqueneaux, C.; Quarton, M.; Riegfalson, F.; Couvreur, P. Temperature-Dependent Rheological Behavior of Pluronic F-127 Aqueous-Solutions. *Int J Pharm* **1987,** *39*, 121-127.

193. Jada, A.; Lang, J.; Zana, R.; Makhloufi, R.; Hirsch, E.; Candau, S. J. Ternary Water in Oil Microemulsions Made of Cationic Surfactants, Water, and Aromatic Solvents .2. Droplet Sizes and Interactions and Exchange of Material between Droplets. *J Phys Chem* **1990,** *94*, 387-395.

194. Nagarajan, R. Molecular Packing Parameter and Surfactant Self-Assembly: The Neglected Role of the Surfactant Tail. *Langmuir* **2002,** *18*, 31-38.

195. Israelachvili, J. N.; Mitchell, D. J.; Ninham, B. W. Theory of Self-Assembly of Hydrocarbon Amphiphiles into Micelles and Bilayers. *J Chem Soc Faraday Trans* **1976,** *72*, 1525-1568.

196. Wu, L.; Tsutahara, M.; Kim, L.; Ha, M. Numerical Simulations of Droplet Formation in a Cross-Junction Microchannel by the Lattice Boltzmann Method. *Int J Numer Methods Fluids* **2008,** *57*, 793-810.

197. Liu, H. H.; Zhang, Y. H. Droplet Formation in Microfluidic Cross-Junctions. *Phys Fluids* **2011,** *23*.

198. Tan, J.; Xu, J. H.; Li, S. W.; Luo, G. S. Drop Dispenser in a Cross-Junction Microfluidic Device: Scaling and Mechanism of Break-Up. *Chem Eng Jl* **2008,** *136*, 306-311.

199. Xu, J. H.; Li, S. W.; Tan, J.; Luo, G. S. Correlations of Droplet Formation in T-Junction Microfluidic Devices: From Squeezing to Dripping. *Microfluid Nanofluidics* **2008,** *5*, 711-717.

200. Xu, J. H.; Li, S. W.; Tan, J.; Wang, Y. J.; Luo, G. S. Preparation of Highly Monodisperse Droplet in a T-Junction Microfluidic Device. *AIChE J* **2006,** *52*, 3005-3010.

201. Garstecki, P.; Fuerstman, M. J.; Stone, H. A.; Whitesides, G. M. Formation of Droplets and Bubbles in a Microfluidic T-Junction - Scaling and Mechanism of Break-Up. *Lab Chip* **2006,** *6*, 437-446.

202. De Menech, M.; Garstecki, P.; Jousse, F.; Stone, H. A. Transition from Squeezing to Dripping in a Microfluidic T-Shaped Junction. *J Fluid Mech* **2008,** *595*, 141-161.

203. Martin, R.; Buchwald, S. L. Palladium-Catalyzed Suzuki-Miyaura Cross-Coupling Reactions Employing Dialkylbiaryl Phosphine Ligands. *Acc Chem Res* **2008,** *41*, 1461-1473.

204. Arpad, M. Efficient, Selective, and Recyclable Palladium Catalysts in Carbon-Carbon Coupling Reactions. *Chem Rev* **2011,** *111*, 2251-2320.

205. Wolfe, J. P.; Singer, R. A.; Yang, B. H.; Buchwald, S. L. Highly Active Palladium Catalysts for Suzuki Coupling Reactions. *J Am Chem Soc* **1999,** *121*, 9550-9561.

206. Wallow, T. I.; Novak, B. M. Highly Efficient and Accelerated Suzuki Aryl Couplings Mediated by Phosphine-Free Palladium Sources. *J Org Chem* **1994,** *59*, 5034-5037.

207. Organ, M. G.; Calimsiz, S.; Sayah, M.; Hoi, K. H.; Lough, A. J. Pd-Peppsi-Ipent: An Active, Sterically Demanding Cross-Coupling Catalyst and Its Application in the Synthesis of Tetra-Ortho-Substituted Biaryls. *Angew Chem Int Ed* **2009,** *48*, 2383-2387.